MACROSEGREGATION IN ELECTROSLAG REMELTED INGOTS

BY

SINDO KOU

B.S., National Taiwan University
1971

M.S., University of Wisconsin
1974

Submitted in partial fulfillment of the requirements

for the degree of

DOCTOR OF PHILOSOPHY

at the

Massachusetts Institute of Technology

February 1978

Signature of Author ....
Department of Materials Science and Engineering
January 13, 1978

Certified by ....
Thesis Supervisor

Accepted by ....
Chairman, Departmental Committee on Graduate Students

ABSTRACT

MACROSEGREGATION IN ELECTROSLAG REMELTED INGOTS

by

SINDO KOU

Submitted to the Department of Materials Science and Engineering on January 13, 1978 in partial fulfillment of the requirements for the degree of Doctor of Philosophy.

Laboratory-scale ESR and simulated ESR apparatus were designed and used to study the formation of macrosegregation in ESR ingots. The laboratory-scale ESR apparatus was used to make a series of Al-4% Cu ingots with a solidification rate of about 4×10^{-2} cm/sec. Macrosegregation in these ingots varied from no macrosegregation in an ingot with a flat mushy zone to 4.25% Cu at the center and 4.6% Cu at the edge for an ingot with a deep mushy zone (Co = 4.4% Cu).

In order to induce more severe macrosegregation, the apparatus for simulating the ESR process was used to make a series of Sn-15% Pb ingots with a solidification rate of about 5×10^{-3} cm/sec. Compositions as rich as 38% Pb (freckling) at the center and as poor as 7% Pb at the edge were found, depending on solidification conditions. In order to study the effect of centrifugal force on macrosegregation across the ESR ingots, the same apparatus was modified to allow rotation of the ingot. A series of rotated Sn-Pb ingots (12∿14% Pb) was made in this way. Solidification rates were varied from 5.3×10^{-3} cm/sec to 1.36×10^{-2} cm/sec and rotation speeds were varied from 54 rpm to 119 rpm. The centerline composition varied from 9% Pb higher than the edge composition to 20% Pb lower than it (freckling at the edge).

Equations for predicting flow of interdendritic liquid and macrosegregation in ESR ingots are derived and a computer model based on these equations is used to numerically calculate the macrosegregation. Agreement between calculations and experimental results is good.

The influence of the important solidification parameters such as the shape and depth of the mushy zone and the local solidification time on the macrosegregation across the ingot is demonstrated quantitatively. The solidification shrinkage effect and the gravity effect on convection in the mushy zone lead to different types of macrosegregation. The conditions under which either effect dominates and the resultant macrosegregation are discussed. In addition, the effect of the important dimensionless group, $\vec{v} \cdot \nabla T / \varepsilon$, on the different macrosegregation results is discussed.

The most important innovation of this work is to introduce and demonstrate the idea of effectively reducing macrosegregation and eliminating "freckles" by rotating the ingot at a suitable speed during solidification. The experimental and calculated results of the rotated ingots show significant reduction in macrosegregation across the ingot and "freckles", which would otherwise be present, are eliminated.

Thesis Supervisor: Merton C. Flemings

Title: Ford Professor of Engineering

TABLE OF CONTENTS

TABLE OF CONTENTS (Cont'd.)

LIST OF FIGURES

LIST OF FIGURES (Cont'd.)

LIST OF FIGURES (Cont'd.)

LIST OF FIGURES (Cont'd.)

LIST OF FIGURES (Cont'd.)

LIST OF FIGURES (Cont'd.)

LIST OF TABLES

ACKNOWLEDGEMENTS

The author would like to thank Professor Merton C. Flemings for his guidance and valuable suggestions. He would also like to thank Professor David R. Poirier of the University of Bridgeport for his encouratement and assistance in this research work.

The author wishes to give thanks to Mr. Robert Furlong for his help in the computer calculations and to Mr. Tetsuya Fujii for his help in the experiment. The suggestions of Professor Robert Mehrabian of the University of Illinois at the beginning of this study is gratefully acknowledged.

The author also wishes to thank the sponsor of this research work, the Army Materials and Mechanics Research Center, Watertown, Massachusetts.

Lastly, the author sincerely thanks Ms. Linda Sayegh for typing this thesis.

I. INTRODUCTION

The ESR process is one of the most important new processes developed for special purpose alloys. The main advantages are that refining can be obtained by melting through a slag of controlled composition, and special control over solidification. Such a control can lead to reduction of dendrite arm spacing, microsegregation, and macrosegregation, giving a sound ingot (1).

However, the recent production of ESR ingots for large, heavy forgings for nuclear-reactor pressure vessels and generator rotors has faced very serious macrosegregation problems including centerline segregation and channel-type segregation (freckles) (2). The non-uniformity of properties and structure can affect deleteriously the mechanical properties of ingots during forging or rolling. Also, in the production of electroslag remelted U-7.5Nb-2.5Zr ingots, it has been found that niobium tends to concentrate at the center of the ingots and results in center-line segregation (3).

Furthermore, due to the strong effect of ingot size on the economics of ESR processing, the production of ingots for forged round billets of stainless steel and tool steels has been found to be profitable only when the ingot size exceeds about 20 inches in diameter (4), and the greater the ingot diameter, the more profitable the ESR process. However, like other casting processes, the macrosegregation problem is expected to become increasingly severe when the ingot size becomes very large.

So far, much experimental and theoretical work has been conducted on the heat transfer in ESR ingots leading to many theoretical heat transfer models which relate the operating parameters in the ESR process to the solidification parameters such as the shape and depth of the mushy zone and the solidification rate (5-7). However, quantitative studies have not been done on how these solidification parameters in turn affect macrosegregation. This work is focused on the experimental and theoretical study of the effects of solidification parameters on macrosegregation in ESR ingots. Also, more importantly, an effective means of reducing macrosegregation and eliminating "freckles" in ESR ingots is demonstrated. Therefore, as a result of this study, one is able to predict solidification conditions required to produce ESR ingots of optimum homogeneity.

It should be emphasized that although macrosegregation in the ESR processes is analyzed in this study, the basic equations can be equally applied to other casting processes such as continuous casting and the VAR process.

II. LITERATURE SURVEY

1. General Background on Macrosegregation

There has been much research on macrosegregation in ingots and castings in the past decade. The direct observation of fluid flow in the mushy zone of solidifying NH_4Cl-H_2O system (8, 9, 10, 11) and analytical and experimental results on macrosegregation in ingots and castings (12, 13, 14, 15, 16) have lead to the conclusion that interdendritic fluid flow in the mushy zone is the most important mechanism of macrosegregation. Since the interdendritic liquid is rich in solute, its physical displacement can lead to considerable solute redistribution and result in macrosegregation. This flow of solute-rich interdendritic fluid is caused primarily by two driving forces (17). The first is the solidification shrinkage, which causes the interdendritic liquid to flow toward the solidus isotherm in order to satisfy continuity. The second driving force is gravity which causes convection since the density varies within the interdendritic liquid. Another but less important force driving the interdendritic flow is the bulk liquid convection which can sometimes penetrate into the mushy zone and sweep away the solute from behind the dendrite tips.

The calculation of the interdendritic fluid flow caused by solidification shrinkage and gravity and the resulting macrosegregation was first performed by Mehrabian et al. (15). They applied D'Arcy's law to calculate the interdendritic fluid flow in horizontally solidified Al-Cu ingots. No bulk motion in the liquid pool was assumed and the metallostatic pressure was used as the boundary condition at the liquidus isotherm. For simplicity, fluid flow and solute redistribution equations were uncoupled in their numerical calculation. The agreement between the experiment and calculation was reasonably good (16). Szekely and Chen (18) calculated heat transfer and fluid flow in the mushy zone of an Al-Cu ingot solidifying in the horizontal direction. However, variations in the volume fraction and density of the interdendritic liquid within the mushy zone were neglected in their equation of continuity. The volume fraction of liquid was calculated from the heat balance only since no mass balance was considered. Later, Jassal and Szekely (11, 19, 20) carried out an experimental and analytical study of the fluid flow in the mushy zone of a solidifying NH_4Cl-H_2O ingot. The calculation was basically the same as that of Szekely and Chen (18). However, this time they calculated the fluid flow in the bulk liquid pool assuming zero velocity of liquid at the liquidus isotherm. Then, by choosing the velocities at some point away from the liquidus isotherm as the velocity boundary condition at the liquidus isotherm, they calculated the fluid flow in the mushy zone. Although agreement between experiment and calculation was claimed, the choice of velocity boundary condition at the liquidus is arbitrary. More recently, Asai and Muchi (10) calculated simultaneously heat, mass and momentum transfer in the mushy zone of a solidifying NH_4Cl-H_2O ingot. Although a mass balance was considered, variations in the density and fraction of interdendritic liquid were neglected in their equation of continuity. While fraction of liquid was calculated; macrosegregation was not measured nor calculated. Also, no quantitative comparison between experiment and calculation was made.

2. Effects of Solidification Parameters on Macrosegregation in ESR Ingots

Like other solidification processes, the shape and depth of the mushy zone plays an important role in macrosegregation formation in ESR ingots. It has been found that operating conditions that favor a deep shape of mushy zone will cause more macrosegregation (21, 22). For example, Fredriksson and Jarleborg (21) observed positive segregation of Ni at the centerline of a 18/8 ingot when the electrode melt rate was high and the liquid pool was deep. However, no segregation was observed at a slower melt rate. Ward and Hambleton (22) pointed out that when the slag skin is reduced (in order to get better surface quality) by increasing the power input subsequent deepening of the liquid pool occurs and causes segregation problems. Moreover, since pool depth increases with the size of ESR ingots (23, 24), macrosegregation problems become particularly serious in very large ESR ingots (2).

The reason why a deep mushy zone causes more macrosegregation in ESR ingots, according to the macrosegregation theory (8, 15), is that the solute-rich interdendritic fluid flow can be strongly affected by solidification shrinkage and gravity in a deep mushy zone. In short, if the solidification conditions favor the solute-rich interdendritic liquid to flow from the center of the ingot to the edge, the solute is depleted at the center and hence negative segregation at the center occurs. Conversely, if flow is from the edge to the center, solute is accumulated at the center, and positive segregation at the center occurs.

Experimental (25) and computer (5) studies have shown that the melting rate of the electrode is the most important parameter in determining the liquid metal pool depth. A higher melting rate results in a deeper metal pool and hence a deeper mushy zone. Other operating parameters such as composition and amount of slag, thermal conductivity of metal, current and voltage, electrode polarity also affect the depth of liquid pool and mushy zone.

3. Prediction and Control of Magrosegregation in ESR Ingots

Although a number of heat flow models (5, 6, 7) have been developed to relate the solidification parameters, such as the shape of the mushy zone and solidification rate to the ESR operating parameters, very little work has been done on the quantitative prediction of macrosegregation in ESR ingots. Mitchell (26) calculated macrosegregation in the axial direction of ESR ingots due to the composition change in the bulk liquid (caused by electrode change or inadequate slag control during solidification). However, this type of segregation, if it exists, is far less severe than that caused by interdendritic liquid flow in the mushy zone. Serious macrosegregation, such as "freckles", cannot be predicted using this approach.

Although no quantitative prediction of macrosegregation in ESR ingots exists at this time, some techniques of improving ingot homogeneity have been reported recently. For example, Cooper (2) developed a so-called "central zone remelting"(C Z R) technique by punching out and remelting the badly segregated central region of big ingots. Success was achieved in improving homogeneity at the ingot centers. However, punching out and remelting the central part consumes extra time and energy. Moreover, any discontinuities (e.g., change in ingot structure or entrapped slag) between the old part and the newly remelted part could cause problems during the subsequent mechanical processing. Thomas et al. (27) also reported success in improving the ingot homogeneity by shielding the solidifying ESR ingot and slag from the disturbance of any stray magnetic field outside the mold. However, it is obvious that this technique cannot reduce the macrosegregation caused by interdendritic fluid flow induced by gravity and/or solidification shrinkage.

Contrary to the work of Thomas et al. (27), Zabaluer et al. (28) claimed success in improving ingot homogeneity by applying a magnetic field to enhance the movement of liquid slag, which, according to the authors, changed the character of dropwise transfer of metal from the electrode and therefore decreased the depth of the conical part of the metal pool.

4. Effect of Centrifugal Force on Macrosegregation

Stewart et al. (29) studied macrosegregation in rotated and oscillated Al-3% Ag conventional-type ingots. In the stationary ingot, the composition ranged from about 2.9% Ag at the center to about 3.1% Ag at the wall. The rotated ingot (126 rpm) showed no significant difference from the stationary one. This might be attributed to the fact that the test castings employed solidified too rapidly to observe any effect of centrifugal force; the ingots were cast in water-cooled stainless steel molds which were only 8 cm in diameter. The oscillated ingot (126 rpm with the direction of rotation being reversed every 5 sec.), however, showed significant macrosegregation. Early in the freezing of the oscillating casting (i.e., near the wall), the high shear force near the solid-liquid interface caused extensive interdendritic flow and swept the solute-rich liquid out of the mushy zone. Therefore, final solute concentration increased from the casting surface toward the interior. Near the mid-radius, however, the temperature gradient decreased and the dendrite fragments, broken off by the shear force, were able to survive and grow. Because of the lower concentration of these fragments, the overall concentration in the center was reduced and, therefore, final solute concentration decreased toward the center.

Recently, Keane (30) studied the effect of centrifugal force on the macrosegregation in Al-4.5% Cu ingots. His work was unidirectional solidification in the radial direction and simulated a slice out of a non-unidirectionally solidified ingot. However, only theoretical calculation was done; no experimental work was performed.

III. THE OUTLINE AND PLAN OF WORK

The plan of work may be summarized as follows:

1. Design and build a laboratory-scale ESR unit suitable for macrosegregation study.

2. Reproduce severe macrosegregation (including freckles) often found in industrial ESR ingots.

3. Study the effects of important solidification parameters such as solidification time and shape and depth of mushy zone on the macrosegregation in ESR ingots.

4. Develop a computer model to predict macrosegregation in ESR ingots. Verify the validity of this model by comparing the calculated results with the experimental macrosegregation results.

5. Study the effect of centrifugal force on the macrosegregation in ESR ingots. Demonstrate experimentally and theoretically the idea of effectively reducing macrosegregation and eliminating freckles by rotating the ingot at a suitable speed during solidification.

IV. THEORETICAL ANALYSIS OF MACROSEGREGATION IN ESR INGOTS

In order to predict quantitatively macrosegregation in ESR ingots, theoretical equations are derived based on fluid flow and mass transfer in solid-liquid system. The basic concept employed is that macrosegregation in ESR ingots is caused by interdendritic fluid flow, as described earlier for other types of ingots by Flemings and Nereo (12), and by Mehrabian, Keane and Flemings (15). In the latter work, equations were derived for the pressure distribution, and hence interdendritic flow, inside the planar mushy zone of a unidirectionally solidifying ingot, using D'Arcy's Law for the interdendritic fluid flow, and taking both gravity and solidification shrinkage as driving forces for the flow. However, in order to simplify the numerical calculation, the governing equations for fluid flow and solute redistribution were uncoupled. In this work, (1) the relevant equations are solved simultaneously and (2) the pressure distribution, flow behavior, and macrosegregation in cylindrical coordinates for the conditions of solidifying ESR ingots are described.

A schematic summary of the analytic work to be described herein is given in Figure 1. Figure 1a shows an ESR ingot during solidification. Liquidus and solidus isotherms are presumed to be known by calculation or by thermal measurement. Properties of the semisolid alloy are known (dendity, solidification shrinkage, etc.) so interdendritic flow behavior can be calculated, as shown in Figure 1b. Solidification theory is then employed to calculate macrosegregation, as shown in Figure 1c. More precisely, as noted in the previous paragraph, the equations for flow behavior and segregation must be solved simultaneously.

A. Analysis of Macrosegregation

The derivation of our pressure distribution equation is briefly given below. First, the "equation of continuity" in the mushy zone is given below (12):

$$\frac{\partial}{\partial t}(\rho_S g_S + \rho_L g_L) = - \nabla \cdot \rho_L g_L \vec{v} \qquad (1)$$

where $\vec{v}$ is the interdendritic fluid velocity, ρ_S and ρ_L are the densities and g_S and g_L are the volume fractions of the solid and liquid, respectively. According to D'Arcy's Law

$$\vec{v} = \frac{K}{\mu g_L}(- \nabla P + \vec{F}_{gravity} + \vec{F}_{centrifugal}) \qquad (2)$$

where K is specific permeability, P is pressure, μ is viscosity of the interdendritic liquid, $\vec{F}_{gravity}$ is the gravity force and $\vec{F}_{centrifugal}$ is the centrifugal force applied. Substituting Equations (2) into Equation (1), we get

$$\nabla \cdot (\frac{K\rho_L}{\mu} \nabla P - \frac{K\rho_L}{\mu} \vec{F}_{gravity} - \frac{K\rho_L}{\mu} \vec{F}_{centrifugal})$$

$$= (\rho_L - \rho_S)(\frac{\partial g_L}{\partial t}) + g_L(\frac{\partial \rho_L}{\partial t}) \qquad (3)$$

Then, the "local solute redistribution equation" is used to account for the partitioning of solute which takes place in dendritic freezing. That equation is (12)

$$\frac{\partial g_L}{\partial t} = - (\frac{1 - \beta}{1 - k})(1 + \frac{\vec{v} \cdot \nabla T}{\varepsilon}) \frac{g_L}{C_L}(\frac{\partial C_L}{\partial t}) \qquad (4)$$

where β is the solidification shrinkage, k is the equilibrium partition ratio, ε is the cooling rate, C_L is the liquid composition and T is the temperature. Equation (4) was first derived by Flemings and Nereo (12). It should be pointed out that in the derivation of the "local solute redistribution equation," ρ_S has been assumed constant. Therefore, in our derivation of Equation (3), ρ_S has also been assumed constant. From Figures 2(b) and 3(b), we see that this assumption is quite reasonable for alloys considered herein.

Now with the chain rule Equation (4) can be written as (see Appendix A):

$$\frac{\partial g_L}{\partial t} = - \left(\frac{1 - \beta}{1 - k}\right) \left(1 + \frac{\vec{v} \cdot \nabla T}{\varepsilon}\right) \frac{g_L}{C_L} \frac{\varepsilon}{m} \tag{5}$$

Similarly,

$$\frac{\partial \rho_L}{\partial t} = \left(\frac{d\rho_L}{dC_L}\right) \frac{\varepsilon}{m} \tag{6}$$

where m is the slope of the liquidus line of the phase diagram, and $d\rho_L/dC_L$ is the slope of ρ_L versus C_L curve for the interdendritic liquid during solidification. Finally, assuming the dendritic structure is similar to a bundle of capillary tubes, Mehrabian et al. (15) proposed the following equation for K, the specific permeability:

$$K = \gamma g_L^2 \tag{7}$$

where γ is a proportional constant. Substituting Equations (5) - (7), and (2) into (3), and then expanding it into cylindrical coordinate form (note that $\vec{F}_{gravity} = -\rho_L \, g \, \vec{z}$ and $\vec{F}_{centrifugal} = \rho_L \omega^2 r\vec{r}$ where g is acceleration due to gravity, ω is rotation speed, $\vec{z}$ and $\vec{r}$ are the axial and the radial unit vectors and r is the radial position), we get the following equation for pressure distribution:

$$\frac{\partial^2 P}{\partial r^2} + \frac{\partial^2 P}{\partial z^2} + A \frac{\partial P}{\partial r} + B \frac{\partial P}{\partial z} + C = 0 \qquad (8)$$

where A, B, and C are defined as follows:

$$A = \frac{1}{r} + \frac{2}{g_L} \frac{\partial g_L}{\partial r} + \frac{1}{\rho_L} \frac{\partial \rho_L}{\partial r} + \alpha \left(\frac{\partial C_L}{\partial r}\right)$$

$$B = \frac{2}{g_L} \frac{\partial g_L}{\partial z} + \frac{1}{\rho_L} \frac{\partial \rho_L}{\partial z} + \alpha \left(\frac{\partial C_L}{\partial z}\right)$$

$$C = g\, \rho_L \left[\frac{2}{g_L} \frac{\partial g_L}{\partial z} + \frac{2}{\rho_L} \frac{\partial \rho_L}{\partial z} + \alpha \left(\frac{\partial C_L}{\partial z}\right) - \alpha \left(\frac{\partial C_L}{\partial r}\right) \frac{\omega^2 r}{g}\right]$$

$$- \frac{\varepsilon \mu}{m \gamma g_L} \left[\frac{1}{\rho_L} \frac{d\rho_L}{dC_L} + \alpha\right] - 2\omega^2 \left[\rho_L + r \frac{\partial \rho_L}{\partial r} + \frac{\rho_L r}{g_L} \frac{\partial g_L}{\partial r}\right]$$

$$\alpha = \frac{\beta}{(1 - k) C_L}$$

The boundary conditions are shown in Figure 4. Since the mold wall is impermeable, $v_r = 0$ at the wall. At the center-line, $v_r = 0$ because of symmetry. At the solidus isotherm, continuity requires that

$$\vec{v}_E = - \left(\frac{\rho_{SE} - \rho_{LE}}{\rho_{LE}}\right) \vec{U}_E \qquad (9)$$

where $\vec{v}_E$ is the interdendritic fluid velocity at the solidus isotherm, $\vec{U}_E$ is the velocity of the solidus isotherm (eutectic temperature), and ρ_{SE} and ρ_{LE} are the densities of eutectic solid and liquid respectively.

Within the bulk liquid pool, we assume no convection so that at the liquidus isotherm the pressure is given approximately by

$$P(\text{liquidus}) = P_0 + \rho_{L0} g\ h + \rho_{L0}\ \omega^2 r^2/2 \qquad (10)$$

where P_0 is the pressure at the top of the liquid pool, ρ_{L0} is the density of the bulk liquid, and h is the height of the liquid pool.

B. Calculation of Macrosegregation

From the measured shape of mushy zone, temperature distribution in the mushy zone, solidification rate and cooling rate, all the unknown variables (except g_L) involved in coefficients A, B, and C are determined with the help of the phase diagram and the density-liquid composition diagram (i.e., Figures 2 and 3). To initiate calculations g_L is approximated using the Sheil Equation (i.e., Equation (4) with β and $\vec{v}$ equal to zero). Now, with the boundary conditions given in Figure 4, Equation (8) is solved for the pressure distribution in the mushy zone. Once the pressure distribution is known, the velocity of interdendritic liquid in the mushy zone is calculated using D'Arcy's Law, Equation (2). With the obtained velocity distribution, the "Local Solute Redistribution Equation", Eqn. (4), is integrated to obtain new values of g_L which are substituted into A, B and C so that a new pressure and velocity distribution can be recalculated. This procedure is repeated until g_L stops changing. This final g_L distribution is the correct one. Finally, with this correct g_L distribution in the mushy zone, the local average composition, $\bar{C}_S$, is (12)

$$\bar{C}_S = \frac{\rho_S \int_0^{1-g_E} C_S dg_S + \rho_{SE} g_E C_E}{\rho_S(1 - g_E) + \rho_{SE} g_E} \quad (11)$$

where C_E and g_E are the composition and fraction of eutectic, respectively, $g_S = 1 - g_L$, and $C_S = kC_L$.

A simplified version of the flow chart of the computer program is given in Appendix B. The numerical technique used to solve for pressure is based upon finite difference approximations for all derivatives. The finite difference forms of equations needed for the calculations are shown in Appendix C. The computer program is given in Appendix D. A list of computer notations used is given in Table 4 of the appendix.

V. APPARATUS AND EXPERIMENTAL PROCEDURE

Two different types of experimental apparatus were employed and these are each described below. The first (employed for Al-4% Cu alloy) was a small scale ESR unit comprised of a DC power source, a water cooled mold, a consumable electrode, and slag layer as in conventional ESR, Figure 5.

The second type of apparatus employed was one which simulates the solidification behavior of the ESR process, but did not utilize slag. This unit, used for Sn-15% Pb alloy, consisted of a source of molten alloy drops, a cooled mold, and a heat source to simulate the heat input of the ESR process, Figure 6.

Small Scale ESR Unit

A sketch of the apparatus is shown in Figure 5 and, with the exception of the mold, is the same previously used by Basaran et al. (31). The power supply is a D.C. arc-welder capable of providing up to 1600 amp and 40 volts for a total power of 55 KW. The electrode mount is connected to a feed screw about 6 ft long which is driven by one of two gear reduction boxes in series with an electric motor. The driving speed of the electrode can be controlled and operated with a speed in the range of 0.2 - 14 cm/min. The electrodes used were 2024 rods (Al-4% Cu) 1 inch in diameter by 6 feet long.

The dimensions of the copper mold where 3 in. diameter by 9 in. high. A thin wash of graphite powder or alumina powder was applied to the mold wall in order to avoid the attack of the mold by the slag (45% LiCl-55%

KCl). Two mold designs were used; the first is shown in Figure 7. The second, shown in Figure 8, was designed for the convenience of replacing the mold wall whenever the mold failed due to the slag attack. This design also made it easy to insert up to 5 thermocouples into the ingot during a run. With both molds, an aluminum bottom hearth was used to insure good bottom welding at the start-up and to prevent the start-up arc from damaging the copper bottom chill.

About 250 cc. of liquid slag of eutectic composition (45wt% LiCl and 55wt% KCl) was poured into the mold at start-up. Immediately after pouring the slag, melting was initiated with a power of 10 KW. The cooling water was turned on and then the power lowered to the working value between 2 and 4 KW. The amperage was kept constant by adjusting the driving speed of the electrode. The electrode position was recorded on a chart recorder during each run. When thermal data were obtained, five chromel-alumel thermocouples were inserted into the mold and pushed to predetermined positions (shown as "X's" in Figure 5) immediately after the electrode passed these positions, and their output recorded. Cooling curves were used to determine the shape of mushy zone, temperature distribution, cooling rates and solidification rates. Thermal data for two ingots (Nos. 1 and 2) were obtained with the second mold design (Figure 8).

Ingot No. 3, made in the first mold design (Figure 7) was doped with about five grams of Al-50% Cu to reveal the liquid pool shape. The ingots were cut into sections in order to obtain analysis by X-ray fluorescence, which was used to detect macrosegregation across the ingots, and in order to obtain samples for microstructures.

Simulated ESR Apparatus

A sketch of the apparatus is shown in Figure 6. The stainless steel mold is 3-1/4 in. in diameter and 13 in. long. The metal pool inside the mold is heated with six 3 in. long resistance heaters connected in parallel. These heaters are positioned inside holes drilled into a 3 in. long by 1-1/4 in. diameter stainless steel bar. Power input is controlled with a Variac transformer.

Cooling water or air runs through a movable cooling jacket surrounding the mold. Both the resistance heaters and the cooler are fixed to the same system used for driving the electrodes in making the Al-4% Cu ingots. Thermal measurements are made with three chromel-alumel thermocouples located inside three vertical stainless steel tubes. The tubes are fixed but the position of the thermocouples is varied during a run by sliding them up and down inside the tubes.

Flow of liquid Sn-15% Pb alloy from the top stainless steel container is controlled by an adjustable valve. Heating of the melt in the top container is done with two 1.5 in. wide band heaters which are controlled by a thermocouple hooked up with a temperature controller. A stirrer was used to insure uniform temperature and composition in the liquid supply.

Tin (99.9%) and lead (99.9%) were melted and stirred well in a crucible furnace. About one-fourth of the charge was poured into the stainless steel mold until the liquid level rose to almost the top of the resistance heaters (about 3.5 in. from the bottom of the mold). The remaining alloy was then poured into the top container. The band heaters, the resistance heaters and cooling water were then turned on.

With the resistance heaters and the cooling jacket fixed, the initial position and the shape of the mushy zone were determined by moving the three thermocouples up and down and locating the position of the liquidus and solidus temperatures of the alloy. Power input to the heaters and cooling jacket position were adjusted until the desired position and shape of mushy zone were obtained.

The resistance heaters and the cooler were then moved upwards at a predetermined speed, and the valve for supply of liquid metal adjusted so that the liquid level inside the mold rose at the same speed. As solidification progressed the three thermocouples were moved up and down in order to determine the temperature distribution in the mushy zone. In the case of rotating ingots, the mold was seated on a turn-table (Fig. 9). One thermocouple was located inside the central stainless steel tube. As in the case of no mold rotation, this thermocouple was allowed to slide up and down in order to trace the positions of solidus and liquidus isotherms. Due to the rotation of the mold, thermocouples inside the other two stainless steel tubes could not be slid up and down. Therefore, inside each of these tubes three thermocouples were located and fixed at different heights. All six of these thermocouples were connected to a slip ring for the purpose of thermal measurement.

The heaters for the liquid pool inside the mold also rotated with the mold in this case.

After casting, the ingots were cut into sections for microstructural study and analysis by X-ray fluorescence to determine macrosegregation.

Chemical Analysis

Chemical analysis of macrosegregation in the ingots was by X-ray fluorescence. A General Electric X-ray diffraction unit (model XRD3, Type 1) was used with a Mo tube. The primary white radiation from the tube fluoresced the samples on an area of 0.32 cm. diameter. This area covered many dendrite arms (secondary dendrite arm spacing is about $40 \sim 65\mu$) and therefore the compositions measured were local average compositions.

The secondary radiation from the sample was received by a Si (Li) X-ray detector and the intensity of the characteristic line (K_α for Cu and L_α for Pb) was compared with a standard intensity versus composition curve to determine the composition.

The standards were prepared from rapidly cooled thin sections of known compositions. The Al-Cu standards used were those prepared by Nereo (14). The Pb-Sn standards were prepared by melting lead and tin together in a graphite crucible to form the liquid alloy of desired composition. About 5 grams of the liquid alloy was quickly removed from the crucible and dropped 1.5 feet onto a copper chill (1.5 inches x 6 inches x 10 inches). The descending drop hit the copper and solidified very rapidly as a splat. A significant portion of the splat formed an area which was similar to a thin disk (about 0.8 mm thick and 2 inches in diameter) with a very smooth and flat bottom surface. A rectangular plate (0.8 inch x 1.2 inches) was cut from the disk and polished with 600 grit metallographic paper for X-ray fluorescence. The remainder of the disk was analyzed by wet chemical analysis to serve as a standard.

VI. RESULTS

A. Experimental Results

Aluminum-4% Copper ESR Ingots

Results of three ingots are summarized in Table 1. The isotherms for Ingots 1 and 2 were obtained from thermal measurements; for Ingot 3, the shape of the isotherm was determined by doping.

Ingot 1 (Al-4.4% Cu)

The cooling curves obtained from the thermocouples as positioned in Figure 8 are given in Figure 10. Figure 11 shows plots of the position of the liquidus isotherm (Z_L) and eutectic isotherm (Z_E) at the center of the ingot. After steady state is achieved, the isotherms move with a vertical speed of 0.053 cm/s. Figure 12 shows the isotherm positions across the ingot.

Figures 11 and 12 can be used to construct the shape of the mushy zone as given in Figure 13a after 7 minutes of ingot solidification has elapsed. As a consequence of cooling rate not varying with radius, the isotherms are parallel. Figure 14 shows the measured temperature distribution along the centerline.

Figure 13c shows the macrosegregation in Ingot 1. The overall analysis of the ingot is 4.4% Cu; as a result of solidification, there is positive segregation at the surface (4.6% Cu) and negative segregation at the center (4.25% Cu). Macroetching showed no evidence of localized segregates, such as "freckles" or "V"-segregates. Dendrite cell size, $\bar{d}$, in this ingot was also measured (Fig. 15). No variation in $\bar{d}$ across the ingot was observed which, of course, is predictable by the fact that cooling rate during solidification is also constant across the ingot.

Ingot 2 (Al-4.4% Cu)

This ingot was cast in the same manner as Ingot 1 with the exception that an unusually thick (about 3 mm.) coating of mold wash (graphite and powdered zirconia) was applied to the inside mold wall. As a result, solidification was unidirectional.

Figures 16 and 17 show cooling curves and isotherm positions, respectively. From Figure 16, we see that temperature is independent of radius, so isotherms must be flat. Cooling rate during solidification is about equal to that observed in Ingot 1, and consequently dendrite cell size is also equal (61μ) (Fig. 15). Figure 18 shows the mushy zone after 7 minutes have elapsed. Since solidification is unidirectional, no macrosegregation is detected in this ingot; nor is there any evidence of localized segregates found in an etched macrosection.

Ingot 3 (Al-4.2% Cu)

Thermal data for Ingot 3 were not measured, but with isotherm shape obtained by doping, the thermal history can be constructed with a knowledge of the electrode melting rate and cooling rate (32) (calculated from dendrite cell sizes). Figure 19 shows the etched macrostructure of Ingot 3. The isotherm is not exactly symmetrical because the electrode was not centered exactly. Dendrite cell size is also uniform across this ingot (61μ, Fig. 15); therefore the isotherms are considered to be parallel to each other.

The degree of macrosegregation for Ingot 3 is shown in Figure 20b. The extent of segregation is considerably less than that of Ingot 1.

Tin-Lead Simulated ESR Ingots

Results of macrosegregation in the series of the Al-4% Cu experimental ingots show that severely localized segregates, as sometimes found in large commercial ESR ingots, cannot be produced using this alloy cast by ESR in small laboratory scale (3 inches in diameter) molds. Although surface-to-center compositional variations were produced, these variations are rather modest and no severe-localized segregates were detected. It was decided, therefore, to design laboratory experiments which could be used to study a wider range of segregation problems encountered in ESR ingots. Accordingly, experimental efforts were directed towards solidifying Sn-Pb alloy in the simulated ESR apparatus (Figure 6). Results from three ingots are summarized in Table 2.

Ingot 4 (Sn-15% Pb)

The positions of the solidus and the liquidus at three radii are given in Figure 21. After 9 minutes steady state was achieved and the isotherms moved with a vertical speed of 4.0×10^{-3} cm/sec, about one order of magnitude less than that obtained in the Al-4% Cu ingots. From Figure 21 the shape of mushy zone after 25 min. is plotted in Figure 22a and the secondary dendrite arm spacing shown in Figure 23. The measured temperature distribution along the centerline is shown in Fig. 24.

In this ingot the resulting macrosegregation across the ingot is pronounced (Figure 22c). The composition ranges from 11.7% Pb at the edge of the ingot to 28.2% Pb at the center. Microstructures show no evidence of "freckles" in this ingot.

Ingot 5 (Sn-15% Pb)

The positions of the solidus and the liquidus during solidification were recorded for this ingot in the same manner as for Ingot 4 isotherms. At steady state, the isotherms moved with a vertical speed of 7.0×10^{-3} cm/sec, Figure 25. Figure 26a shows the shape of mushy zone at 14 min., and the measured secondary dendrite arm spacing is shown in Figure 23.

The macrosegregation is shown in Figure 26c which shows that the composition ranges from 7% Pb at the mid-radius of the ingot to 28% Pb at the center. This segregation pattern is more severe than in Ingot 4 (Figure 22c), and the microstructures show clear evidence of "freckling" in this ingot (Figure 27).

Ingot 6 (Sn-15% Pb)

In this ingot, steady state solidification was not achieved until after 20 min. when the isotherms moved with a vertical speed of 5.1×10^{-3} cm/sec (Figure 28). The shape of mushy zone after 23 min. is plotted in Figure 29a and the greater secondary dendrite arm spacings shown in Figure 23 reflect a lower cooling rate than in Ingots 4 and 5.

As seen in Figure 29c, macrosegregation across this ingot is even more severe than in Ingot 5; composition varies from 11.5% Pb at the edge of the ingot to 38% Pb (eutectic composition) at the center of the ingot. The microstructures (Fig. 30) show that along the centerline there is a large channel or "freckle"; other areas show no evidence of "freckling."

Tin-Lead Simulated ESR Ingots with Mold Rotation

Results of macrosegregation in the series of Sn-Pb ingots (Ingots 5 and 6) show not only very severe surface-to-center compositional variations, but also "freckles". It was decided to rotate the mold during casting in order to study the effect of centrifugal force on macrosegregation.

Ingot 7 (Sn-12% Pb)

This ingot was cast with three different rotation speeds: 0 rpm, 45 rpm and 76 rpm. The measured shapes and positions of the mushy zone 25 minutes, 50 minutes and 75 minutes after the start are shown in Fig. 31. The solidification rate was 3.0×10^{-3} cm/sec. The macrosegregation results are shown in Fig. 32. It can be seen in Fig. 32 that the degree of macrosegregation was slightly reduced in the case of 45 rpm rotation, but was reduced significantly in the case of 76 rpm rotation. Microstructures showed "freckling" at the center of the ingot for zero and 45 rpm. rotations (Fig. 33), but no "freckling" was observed in the case of 76 rpm rotation.

Ingots 8∿12 were cast with detailed thermal measurement. Each ingot was cast under one single rotation speed and in each ingot solidification reached state at about 10$\sim$25 minutes after the start. Results from these five ingots are summarized in Table 3.

Ingot 8 (Sn-12.4% Pb)

Results of thermal measurements are shown in Figs. 34, 35 and 36. At steady state, the isotherms moved with a vertical speed of 5.6×10^{-3} cm/sec. The shape of the mushy zone 30 minutes after the start is shown in Fig. 37a. The rotation speed was 83 rpm (8.7 rad./sec). The measured dendrite arm spacings are given in Fig. 38.

The macrosegregation is shown in Fig. 37c. The composition ranges from 11% Pb at the edge of the ingot to 19% Pb at the center. Microstructures show no evidence of freckles.

Ingot 9 (Sn-14.0% Pb)

Results of thermal measurement are given in Figs. 39, 40 and 41. At steady state, the isotherms moved with a vertical speed of 6.6×10^{-3} cm/sec. The shape of the mushy zone 28 minutes aftet the start is given in Fig. 42a. The rotation speed was 97 rpm (10.1 rad/sec). Dendrite arm spacings are shown in Fig. 38. The resulting macrosegregation is shown in Fig. 42c. The W-shape composition profile is the result of rotation. Microstructures show no evidence of freckles.

Ingot 10 (Sn-12.8% Pb)

Results of thermal measurement are given in Fig. 43, 44 and 45. At steady state, the isotherms moved with a vertical speed of 5.3×10^{-3} cm/sec. The shape of the mushy zone 30 minutes after the start is given in Fig. 46a. The rotation speed was 119 rpm (12.5 rad/sec). Dendrite arm spacings are shown in Fig. 38. The resulting macrosegregation is shown in Fig. 46c. The composition is relatively uniform across the ingot except near the edge where it jumps to nearly the eutectic composition. This can be seen from the microstructures at the wall, Fig. 47 and 48. The evidence of "freckling" at the wall is very clear.

Ingot 11 (Sn-12.4% Pb)

Results of thermal measurement are given in Figs. 49, 50 and 51. At steady state, the isotherms moved with a vertical speed of 8.3×10^{-3} cm/sec. The shape of mushy zone 35 minutes after the start is given in Fig. 52a. The rotation speed was 66 rpm. The dendrite arms spacings are shown in Fig. 38.

The macrosegregation is given in Fig. 52c. The composition jumps to approximately 25% Pb at about 0.8 cm from the wall, where the slopes of the isotherms go up drastically. The microstructures show clear evidence of "freckling" at this position, Fig. 53.

Ingot 12 (Sn-12% Pb)

Results of thermal measurement are given in Figs. 54, 55 and 56. At steady state, the isotherms moved with a vertical speed of 1.36×10^{-2} cm/sec. The shape of mushy zone at 12 minutes after the start is given in Fig. 57a. The rotation speed was 54 rpm. The dendrite arm spacings are shown in Fig. 38.

The macrosegregation is shown in Fig. 57c. As expected, the macrosegregation is slight because the solidification rate was high. Microstructual show no evidence of "freckles".

B. Comparison Between Experimental and Calculated Results

Aluminum-Copper ESR Ingots

Calculation of flow lines and macrosegregation were done using the phase diagram and density data for Al-Cu system as shown in Figures 2b and c, respectively. The value of viscosity used was 1.3 centipoises (33, 34). The value of γ used is on the order of 10^{-7} cm^2 which agrees with the value used by Mehrabian et al. (16) to obtain the best fit between their theoretical and experimental results of macrosegregation in Al-4.5% Cu ingots.

Ingot 1 (Al-4.4% Cu)

With γ equal to 5×10^{-7} cm^2 the agreement between theory and the experiment is quite good for most part of the ingot (Figure 13c). Flow lines based on the calculated velocity distribution of the interdendritic liquid are shown in Figure 13b. The spacing of the flow lines is approximately proportional to the inverse of velocity magnitude.

Flow is predominantly downward and outward, Figure 13b, and so segregation, calculated and observed, is negative at the center, Figure 13c.

Ingot 2 (Al-4.4% Cu)

The value of γ was again 5×10^{-7} cm^2. Calculations show no macrosegregation, which is in agreement with the experiment. Flow lines are downward and vertical as expected and consistent with the absence of macrosegregation.

Ingot 3 (Al-4.2% Cu)

The mushy zone was not symmetrical because as previously mentioned the electrode was not centered exactly; however for calculations we assume a symmetrical mushy zone (Figure 20a). The width of the mushy zone (vertical distance between the solidus and liquidus) is constant since cooling rate was also independent of radius as indicated by a constant dendrite cell size (61 microns) across the ingot.

The degree of macrosegregation for ingot 3 is shown in Figure 20b. The extent of segregation is less than that of Ingot 1. Calculations with $\gamma = 3 \times 10^{-7}$ cm^2 agree remarkably well with experiment except that the minimum point in the experimental curve is off-center.

Tin-Lead Simulated ESR Ingots

Calculation of flow lines and macrosegregation were done using the phase diagram and density data for the Sn-Pb system as shown in Fig. 3a and b, respectively. The value of viscosity used was 2.2 centipoises (35).

In Ingots 4, 5, and 6, the width of the mushy zone and the cooling rate vary from center to surface. This is seen in Figure 23 which shows a decrease in the secondary dendrite arm spacing in going from the center to the surface. The calculations take into account this variation by making permeability (and, hence, γ) a function of the secondary dendrite arm spacing. Data of Streat and Weinberg (36) show that permeability varies with square of secondary dendrite arm spacing, d, for $25<d<60$ microns. Accordingly, we select a value of γ at the centerline (γ_o) and vary γ

according to

$$\gamma/\gamma_o = (d/d_o)^2 \tag{7}$$

Ingot 4 (Sn-15% Pb)

Calculations of flow lines and macrosegregation are shown in Figures 22b and 22c respectively. With $\gamma_o = 3.7 \times 10^{-6}$ cm^2, the calculated result of macrosegregation agrees reasonably well with experiment. Since permeability in lead-rich Pb-Sn alloys (36) is reported to be 10^1 - 10^2 greater than the value of permeability for aluminum alloys (37, 38), it is reasonable that γ is on the order of 10^{-6} cm^2 assuming similar behavior of tin-rich and lead-rich Sn-Pb alloys.

The calculated flow pattern, shown in Figure 22b shows that gravity has a very strong effect on the flow, causing the interdendritic liquid to flow from the surface towards the ingot center and up near the center resulting in positive segregation in the center of the ingot. It will be seen that such flow (from "cold" to "hot" regions in the mushy zone), when sufficiently strong, leads to localized channels of increased flow and the formation of freckles.

Ingot 5 (Sn-15% Pb)

A value of γ_o was selected by using the best value determined for Ingot 4 ($\gamma_o = 3.7 \times 10^{-6}$ cm^2) and adjusting for the decrease in secondary arm spacing at the centerline (Figure 23). This gives $\gamma_o = 2.4 \times 10^{-6}$ cm^2. Flow calculations show that $(\vec{v} \cdot \nabla T/\varepsilon) < -1$ in Equation (4), and hence $\partial g_L/\partial t > 0$ in these regions of the ingot. This phenomenon is discussed in more detail below. Essential points are that, when $\vec{v}\cdot\nabla T/\varepsilon<-1$, (a) "freckles" can form, and (b) the method of quantitatively calculating macrosegregation is no longer valid.

Figure 26b shows calculated flow lines with permeability decreased to the point that their directions are observed just at the onset of developing a flow instability. With $\gamma_o = 2.0 \times 10^{-7}$ cm^2, $(\vec{v}\cdot\nabla T/\varepsilon)>-1$ throughout the entire mushy zone. With permeability decreased by almost one order of magnitude, the flow is still towards the centerline and upwards at the center. Flow is strongly enhanced in Ingot 5 over that in Ingot 4, because the isotherms in the mushy zone are significantly deeper; this difference is apparent in Figures 22a and 26a. With $\gamma_o>2.0 \times 10^{-7}$ cm^2, the flow is stronger than indicated in Figure 26b, and the formation of freckles is predicted as observed in Figure 27.

Ingot 6 (Sn-15% Pb)

As with Ingot 5, when permeability is selected to correspond to the dendrite arm spacing in Figure 23 ($\gamma_o = 4.4 \times 10^{-6}$ cm^2), calculations indicate $(\vec{v}\cdot\nabla T/\varepsilon)<-1$ in the central regions of the ingot predicting the formation of a freckle. The flow lines shown in Figure 29b are calculated using $\gamma_o = 8 \times 10^{-7}$ cm^2; with greater values, the instability develops. Figure 29b however does indicate that the overall interdendritic flow is similar to that observed in Ingots 4 and 5. Macrosegregation in Ingot 6 is more severe than in Ingot 5 because the local solidification time is significantly greater (Figure 23).

Tin-Lead Simulated ESR Ingots with Mold Rotation

Ingot 8 (Sn-12.2% Pb)

The calculated flow pattern and macrosegregation are shown in Fig. 37b and c, respectively. The value of γ_o used was 1.2 x 10^{-6} cm^2, which was obtained from the best fit between the theoretical and experimental results. This value is close to the value estimated from Equation (7) and the dendrite arm spacings (Figs. 23 and 38), γ_o = 2.0 x 10^{-6} cm^2 (see Fig. 58). Therefore, as with no mold rotation, the agreement between theory and experiment is reasonably good.

Ingot 9 (Sn-14.0% Pb)

The calculated flow pattern and macrosegregation are shown in Fig. 42b and c,respectively. A value of γ_o = 0.98 x 10^{-6} cm^2 was obtained from the best fit between measured and calculated results. The corresponding value estimated from the dendrite arm spacing measurements is 1.0 x 10^{-6} cm^2 (see Fig. 58). The agreement is, therefore, excellent.

Ingot 10 (Sn-12.8% Pb)

The calculated flow pattern and macrosegregation are shown in Fig. 46b and c respectively. A value of γ_o = 1.3 x 10^{-6} cm^2 was obtained from the best fit between theoretical and experimental results. The corresponding value estimated from the dendrite arm spacing measurement is 1.1 x 10^{-6} cm^2 (see Fig. 58). Again, the agreement is very good.

The calculated flow pattern shown upward interdendritic fluid flow near the wall. Calculations also indicate $(\vec{v}\cdot\nabla T/\varepsilon)<-1$ here predicting the formation of freckles.

Ingot 11 (Sn-12.4% Pb)

The calculated flow pattern and macrosegregation are shown in Fig. 52b and c, respectively. The value of γ_o estimated from the dendrite arm spacing measurements, 3.3×10^{-6} cm^2, was used in the calculation. The agreement between calculated and experimental macrosegregation results are not as good as Ingots 8-10. However, the calculations do show the peaks in the concentration profile, though the positions of these peaks are not exactly the same as the observed ones.

The calculated flow pattern shows upward interdendritic fluid flow in the region between the mid-radius and the wall. The calculations also indicate $\vec{v} \cdot \nabla T/\varepsilon < -1.0$ in this region predicting the formation of "freckles."

Ingot 12 (Sn-12.0% Pb)

The calculated flow pattern and macrosegregation are shown in Fig. 57b and c, respectively. A γ_o value of 1.0×10^{-6} cm^2 was obtained from the best fit between the calculated and experimental macrosegregation results. The corresponding value estimated from the dendrite arm spacing measurement is 1.43×10^{-6} cm^2 (see Fig. 58). Therefore, the agreement is reasonably good.

VII. DISCUSSION

1. Effect of Solidification Time and Permeability

Both the Al-4% Cu ingots (1 and 3) and Sn-15% Pb ingots (4, 5 and 6) have concave shapes of mushy zone, and in both alloys, (1) the equilibrium partition ratio k is less than one and (2) the density of the interdendritic liquid increases progressively during solidification. However, the Al-4% Cu ingots have negative center-line macrosegregation while the Sn-15% Pb ingots have positive center-line macrosegregation. The reason for this can be explained as follows.

In a concave mushy zone, solidification shrinkage tends to suck the solute-rich interdendritic liquid toward the solidus isotherm and, therefore, the solute-rich interdendritic liquid in the mushy zone tends to flow downwards and outwards (see, for example, Fig. 13b). But, at the same time, the gravity effect also tends to cause flow of the dense, solute-rich interdendritic liquid from the upper, outer region of the mushy zone to the lower, central region of the mushy zone (see, for example, Fig. 26b). Therefore, the convection effects of solidification shrinkage and gravity compete during solidification. If the shrinkage effect dominates, solute is diverted away from the center-line of the ingot and, therefore, negative center-line macrosegregation will occur. On the other hand, if the gravity effect dominates, solute will be accumulated along the center-line of the ingot and, therefore, positive centerline macrosegregation will occur. Both solidification time and permeability are very important in determining whether solidification shrinkage or gravity will dominate. According to the continuity requirement, the interdendritic liquid always feeds solidification shrinkage (1) no matter whether the solidification time is long or short and (2) no matter whether the permeability is high or low. But, if the solidification time is too short and the permeability is too low, the interdendritic liquid is already sucked toward the solidus isotherm by the solidification shrinkage before gravity has sufficient time to affect significantly the flow pattern of the interdendritic liquid. Therefore, solidification shrinkage is more likely to dominate when the solidification time is short and the permeability is low. Conversely, the gravity effect is more likely to dominate if the solidification time is long and the permeability is high.

In short, since the Al-4% Cu ingots were produced with a much greater (10 times faster) vertical solidification rate and a narrower mushy zone than were the Sn-15% Pb ingots, the solidification time of Al-4% Cu ingots was much shorter than that of Sn-15% Pb ingots. Also, as mentioned before, the permeability of Al-4% Cu alloy is 10^1-10^2 less than that of Sn-15% Pb alloy. Therefore, solidification shrinkage dominated in the Al-4% Cu ingots during solidification and resulted in negative center-line macrosegregation. The gravity effect dominated in the Sn-15% Pb ingots during solidification and resulted in freckling as well as positive center-line macrosegregation.

2. Effect of Mushy Zone Shape

The three Al-4% Cu ingots were cast with the same local solidification time since secondary dendrite arm spacings are equal. However, the results show that the deeper the shape of mushy zone, the greater the degree of negative center-line macrosegregation. This is because, in a deep mushy zone, the solute-rich interdendritic liquid is sucked toward the steep solidus isotherm and the solute is diverted away from the center-line of the ingot. Therefore, a greater degree of negative center-line macrosegregation results. Of course, if there is vertical unidirectional solidification, no macrosegregation results.

As another example of this effect, let us now consider Ingot 4 and Ingot 5 of Sn-15% Pb alloy. The upward solidification rate of Ingot 5 is about twice the value of Ingot 4 while the width (i.e., vertical distance from solidus to liquidus) of the mushy zone of Ingot 5 is slightly smaller than that of Ingot 4. Therefore, the solidification time of Ingot 5 is less than that of Ingot 4. This can also be seen from secondary dendrite arm spacings shown in Figure 23 (smaller secondary dendrite arm spacing means shorter solidification time.) However, the shape of the mush zone of Ingot 5 is much deeper than that of Ingot 4. Therefore, the resultant macrosegregation of Ingot 5 is still more severe than that of Ingot 4.

The effects of solidification time and shape of mushy zone on macrosegregation are further illustrated in Figure 59. Here, macrosegregation has been calculated in Al-4.4% Cu ESR ingots of geometry studied in this work, for different solidification conditions. Calculated flow lines and macrosegregation are shown for two different solidification times (solidification time = $(Z_L - Z_S)/R$, where $Z_L - Z_S$ is the width of mushy zone and R is the upward solidification rate) and for mushy zones of three different degrees of concavity (i.e., three different "depths" where depth refers to distance from the highest to the lowest point in the mushy zone). Note that for both short and long solidification time, the degree of macrosegregation increases with increasing depth of mushy zone. In the case of short solidification time (a, b and c), we have negative centerline macrosegregation, while in the case of long solidification time (d, e and f), we have positive centerline macrosegregation.

3. The Dimensionless Group, $\vec{v}\cdot\nabla T/\varepsilon$

According to macrosegregation theory (4, 5), the important dimensionless parameter affecting macrosegregation is $\vec{v}\cdot\nabla T/\varepsilon$. When this is equal to $\beta/1-\beta$ no macrosegregation results; when it is greater, segregation is negative and when it is less, segregation is positive. Figure 60a shows a plot, for Ingot 1, of $\vec{v}\cdot\nabla T/\varepsilon$ at the centerline during solidification (i.e., as C_L increases from C_0 to C_E). $\vec{v}\cdot\nabla T/\varepsilon$ is greater than $\beta/1-\beta$ throughout solidification, resulting in a lower composition of solid forming at any time during solidification and a lower fraction eutectic than would form in the absence of segregation (Figure 60b). Hence segregation is negative here.

Figure 61 is a plot similar to that of Figure 60 in all respects except that here $\vec{v}\cdot\nabla T/\varepsilon$ is less than $\beta/1-\beta$ and so segregation is positive. This plot applies to the centerline of Ingot 4.

Note in Ingot 4 that $\vec{v} \cdot \nabla T/\varepsilon$ is never less than -1. At the critical point where this occurs, flow velocity in the direction of isotherm movement is greater than velocity of isotherms and "remelting" occurs. This is the criterion for formation of freckles (15). $\vec{v} \cdot \nabla T/\varepsilon$ was calculated to be less than -1 in Ingots 5, 6, 10 and 11, and here, as expected, "freckles" (channel type segregates) were observed.

4. Effect of Centrifugal Force

The experimental results from Ingot 7 demonstrate clearly the effect of centrifugal force on reducing the macrosegregation across the ESR ingots and eliminating "freckles". The quantitative effect of the centrifugal force can be better demonstrated with the help of the computer model. Figure 62 shows the calculated macrosegregation for different rotation speeds. The mushy zone of Ingot 8 was used in all of these calculations. The γ value of Ingot 8 was used, as well.

As can be seen in Fig. 62, without mold rotation, there is very severe positive centerline macrosegregation and pronounced "freckling" at the center of the ingot. With increasing rotation speed the high solute concentration at the centerline decreases and the low solute concentration at the wall increases. Freckling at the centerline also disappears. At higher rotation speeds (e.g. ω = 13.0 rad./sec), the concentration profile resembles the shape of a "W". At even higher rotation speeds (e.g., ω = 15 rad./sec), the solute-rich interdendritic liquid is pushed to the wall and is forced to flow upwards. Therefore, "freckling" as well as positive macrosegregation develops near the wall.

As can be seen from Figs. 62 and 63 (similar to Fig. 62 except the solidification rate is higher), the optimum concentration profile can be obtained if a suitable rotation speed is applied in this ingot (e.g., ω = 12 rad/sec).

The effect of centrifugal force on macrosegregation across ESR ingots is affected by the solidification rate. Examination of Figs. 62 and 63 shows that the effect of centrifugal force is more pronounced at lower solidification rates. This can be seen more clearly in Fig. 64, where $\Delta C/C_o$ is plotted vs. ω^2. ΔC is the concentration at the ingot center minus the concentration at the edge, and C_o is the original concentration. As can be seen in this figure, at high solidification rates (e.g., 0.056 cm/sec), the macrosegregation is very slight and the centrifugal force has hardly any effect on the macrosegregation. However, when the macrosegregation is severe due to a very slow solidification rate (e.g., 0.0035 cm/sec), sufficient mold rotation not only reverses the concentration profile from positive centerline segregation to negative centerline segregation, but also changes the location of freckling from the center of the ingot to the edge.

Finally, it is to be noted that although Fig. 64 shows the strong influence of the solidification rate on the effectiveness of the centrifugal force, it also shows that the optimum rotation speed for minimizing the macrosegregation is independent of solidification rates (e.g., ω = 12 rad/sec for this ingot).

VIII. CONCLUSION

1. Laboratory-scale ESR apparatus was used to make a series of Al-4% Cu ingots with a solidification rate of about 4×10^{-2} cm/sec. Macrosegregation in these ingots varied from no macrosegregation in an ingot with a flat mushy zone to 4.25% Cu at the center and 4.6% Cu at the edge for an ingot with a deep mushy zone (C_o = 4.4% Cu).

2. Apparatus for simulating the ESR process was used to make a series of Sn-15% Pb ingots with a solidification rate of about 5×10^{-3} cm/sec. Compositions as rich as 38% Pb (freckling) at the center and as poor as 7% Pb at the edge were found, depending on solidification conditions.

3. The apparatus for simulating the ESR process was modified to allow rotation of the ingot. A series of rotated Sn-Pb ingots (12$\sim$ 14% Pb) was made in this way. Solidification rates were varied from 5.3×10^{-3} cm/sec to 1.36×10^{-2} cm/sec and rotation speeds were varied from 54 rpm to 119 rpm. The centerline composition varied from 9% Pb higher than the edge composition to 20% Pb lower than it (freckling at the edge).

4. Calculations which predict macrosegregation in ESR ingots compare very well with experimental results. The calculated interdendritic fluid flow patterns clearly demonstrate the influence of solidification shrinkage and gravity on the observed macrosegregation across experimental ESR ingots.

5. The effects of the important solidification parameters such as the upward solidification rate and the depth of the mushy zone on macro-segregation in ESR ingots can be evaluated quantitatively.

6. The computer model developed predicts correctly the conditions which cause the formation of "freckles".

7. Severe positive centerline macrosegregation can be reduced significantly and freckling at the center of the ESR ingots can be eliminated if a suitable speed of mold rotation is applied during solidification. The computer model can be applied to predit the optimum rotation speed for minimizing macrosegregation and eliminating freckles.

8. The effect of centrifugal force on macrosegregation across ESR ingots is influenced by the solidification rate. At high solidification rates (e.g., 10^{-2} cm/sec) the macrosegregation is slight and the centrifugal force has little effect on the macrosegregation. However, when macrosegregation is severe due to a very slow solidification rate (e.g., 10^{-3} cm/sec), a very fast rotation speed (e.g., 150 rpm) not only reverses the concentration profile from positive centerline segregation to negative centerline segregation, but also changes the location of freckling from the center of the ingot to the edge.

9. The optimum rotation speed for minimizing the macrosegregation is independent of solidification rates.

REFERENCES

1. E. Plokinger, "Electroslag Remelting - A Modern Tool in Metallurgy", J.I.S.I., Aug. 1973, pp. 533-541.
2. L. Cooper, "Central Zone Remelting of Ingots using an Electroslag Process". Fifth International Symposium on ESR Process, Oct. 1974, pp. 202-238.
3. Cadden, J.L., Jessen, N.C., and Lewis, P.S. "Melting of Uranium Alloys." Paper presented at Physical Metallurgy of Uranium Alloys Conference, Vail, Colorado, February 1974. (Preprint Y-DA-5323, Oak Ridge Y-12 Plant, 1973).
4. Arwidson, S.G. "Technico-Economic Appraisal of a Large Tonnage ESR Installation." In Electroslag Refining, pp. 157-62. London: Iron and Steel Institute, 1973.
5. M.A. Maulvault, "Temperature and Heat Flow in the Electroslag Remelting Process", Ph.D. Thesis, 1971, MIT, Dept. of Metallurgy and Materials Science.
6. R.C. Sun, J.W. Pridgeon, "Predicting Pool Shapes in a Laboratory Electroslag Remelting Process", Union Carbide Corporation, Materials System Division, Technology Dept., Kokomo, Indiana, Sept. 1969, Report No. 7649.
7. A. Mitchell, S. Joshi, "The Thermal Characteristics of the Electroslag Process", Met. Trans., V. 4, 1973, pp. 631-642.
8. R.J. McDonald, J.D. Hunt, "Fluid Motion through the Partial Solid Region of a Casting and Its Importance in Understanding 'A' Type Segregation", Trans. Met. Soc. AIME, V. 245, 1969, pp. 1993.
9. S.M. Copley, A.F. Giamei, S. M. Johnson, M.F. Hornbecker, "The Origin of Freckles in Unidirectionally Solidified Castings", 69-028, Pratt & Whitney, Aircraft, Middletown, Connecticut.
10. S. Asai and I. Muchi, "Simultaneous Heat Mass and Momentum Transfer in the Mushy Zone of Ingot", Japan-US Joint Seminar on Solidification of Metals and Alloys, Jan. 1977, Tokyo, Japan, pp. 57-68.

11. A.S. Jassal, "An Experimental and Analytical Study of the Fluid Velocities and Flow Patterns in the Interdendritic Region During Solidification of a Binary System", Ph.D. Thesis, 1975, State University of New York at Buffalo.

12. M.C. Flemings, F.E. Nereo, "Macrosegregation, Part I", Trans. Met. Soc. AIME, V. 212, 1967, pp. 1449.

13. M.C. Flemings, G.E. Nereo, R. Mehrabian, "Macrosegregation, Part II", Trans. Met. Soc. AIME, V. 242, 1968, pp. 41.

14. M.C. Flemings, G.E. Nereo, "Macrosegregation, Part III", Trans. Met. Soc. AIME, V. 242, 1968, pp. 50.

15. R. Mehrabian, M. Keane, M.C. Flemings, "Interdendritic Fluid Flow and Macrosegregation: Influence of Gravity", Met. Trans. V. 1, 1970, pp. 1029.

16. R. Mehrabian, M.A. Keane and M.C. Flemings, "Experiments on Macrosegregation and Freckle Formation", Met. Trans. v. 1, 1970, pp. 3238-3241.

17. M.C. Flemings, "Principles of Control of Soundness and Homogeneity of Large Ingots", Scand. J. Metallurgy, v. 5, 1976, pp. 1-15.

18. J. Szekely and J.H. Chen, "Thermal Natural Convection in the Two-Phase Region of a Solidifying Alloy", In Chemical Metallurgy of Iron and Steel, publ. by the Iron and Steel Inst., London, July, 1971, pp. 218-220.

19. J. Szekely and A.S. Jassal, "Experimental and Analytical Study of the Solidification of a Binary System - Part I Experimental", to be published in Met. Trans. 1977.

20. J. Szekely and A.S. Jassal, "Experimental and Analytical Study of the Solidification of a Binary System - Part II Mathematical Analysis", to be published in Met. Trans. 1977.

21. H. Fredriksson, O. Jarleborg, "Solidification of ESR Ingots", J. of Metals, Sept. 1971, pp. 32.

22. J.O. Ward and R.C. Hambleton, "Production Experience of Electroflux Remelting of Nickel-Base Superalloys", Electroslag Refining, published by Iron and Steel Inst., 1973, pp. 80-88.

23. R. Schumann and C. Ellebrecht, "Metallurgical and Process Problems Related to ESR of Forging Ingot Larger than 40 Inch Diameter and 150 Inch Length in Single Electrode Technique," Fifth International Symposium on ESR Process, pp. 180-201.

24. A.S. Ballantyne and A. Mitchell, "Computer Simulation of Cold Crucible Ingots," Fifth International Symposium on ESR Process, pp. 345-409.

25. Yu M. Mironov, M.M. Klyuev, "Some Features of the Solidification of Electroslag Ingots", Russian Metallurgy, No.2, 1968, pp. 72-76.

26. A. Mitchell, "Macrosegregation, Liquid Movement and Heat Flow in the ESR Process", Fourth International Symposium on Electroslag Remelting Process, June 7-8, 1973, Tokyo, Japan, p. 1.

27. F.W. Thomas, F. Knell, E. Weingartner, "Magnetic Field Effects in Vacuum ARC and Electroslag Remelting", Fifth International Symposium on ESR Process, Oct. 1974, pp. 722.

28. Y.I. Zabaluev, E.I. Moshkevich, G.A. Buryakovskii, G.M. Brodskii, and A.A. Nikulin, "Improvement in the Quality of Electroslag Remelted Steel by the Action of a Magnetic Field," Steel in USSR, Aug. 1973, pp. 644-645.

29. M.J. Stewart, L.C. LacAulay and F. Weinberg," Macrosegregation in Castings Rotated and Oscillated During Solidification", Met. Trans., v.2, 1971, pp. 169-173.

30. M. A. Keane, Sc.D. Thesis, Department of Materials Science and Engineering, Massachusetts Institute of Technology, 1973.

31. M. Basaran, T.Z. Kattamis, R. Mehrabian, M.C. Flemings, "A Study of the Heat and Fluid Flow in Electroslag Remelting", U.S. Army Materials and Mechanics Research Center, Contract No. DAAG 46-73-C-0088, April, 1974.

32. P.O. Mellberg and H. Sandberg, Scand. J. Metallurgy, v. 2, 1973, pp. 83-86.

33. E. Rothwell, J. Inst. Metals, v. 90 (1961/1962), pp. 389-394.

34. E. Gebhardt, M. Becker, J. Dorner, Metallkunde, v. 44 (1953), pp. 510-518.

35. H. R. Thresh, A.F. Crawley, Met. Trans., v. 1 (1970), pp. 1531-1535.

36. M. J. Streat and F. Weinberg, Met. Trans. B., v. 7b (1976), pp. 417-423.

37. T.S. Piwonka, M.C. Flemings, Trans. TMS-AIME, v. 236 (1966), pp. 1157-1165.

38. D. Apelian, M.C. Flemings, R. Mehrabian, Met. Trans., v. 5 (1974), pp. 2533-2537.

39. Metals Handbook, v. 8, A.S.M., 1973, p. 259.

40. Metals Handbook, v. 8, A.S.M., Metals Park, Ohio, 1973, p. 330.

41. H.R. Thresh, A.F. Crawley and D.W.G. White, Trans. TMS-AIME, v. 242 (1968), pp. 819-822.

42. H.J. Fisher, A. Philips, Trans. TMS-AIME, v. 200 (1954), pp. 1060-1070.

43. A. Lee and G.V. Raynor, Proc. Phys. Soc., v. B67 (1954), pp. 737-747.

44. C. Tyzack and G.V. Raynor, Acta Cryst., v. 7 (1954), pp. 505-510.

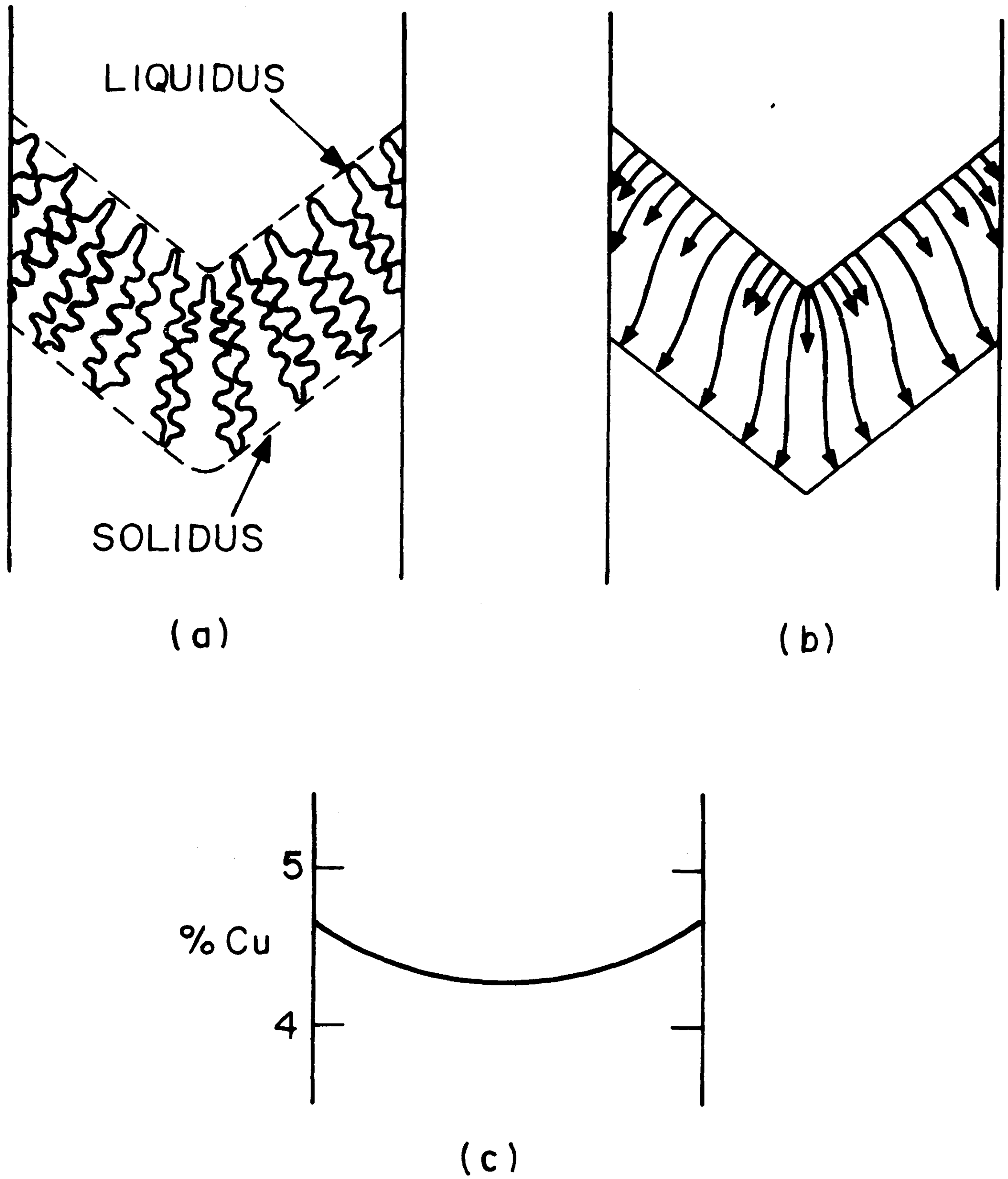

Figure 1: Macrosegregation in an Al-4.4% Cu ESR ingot. (a) Mushy zone; (b) flow lines for interdendritic liquid; (c) macrosegregation.

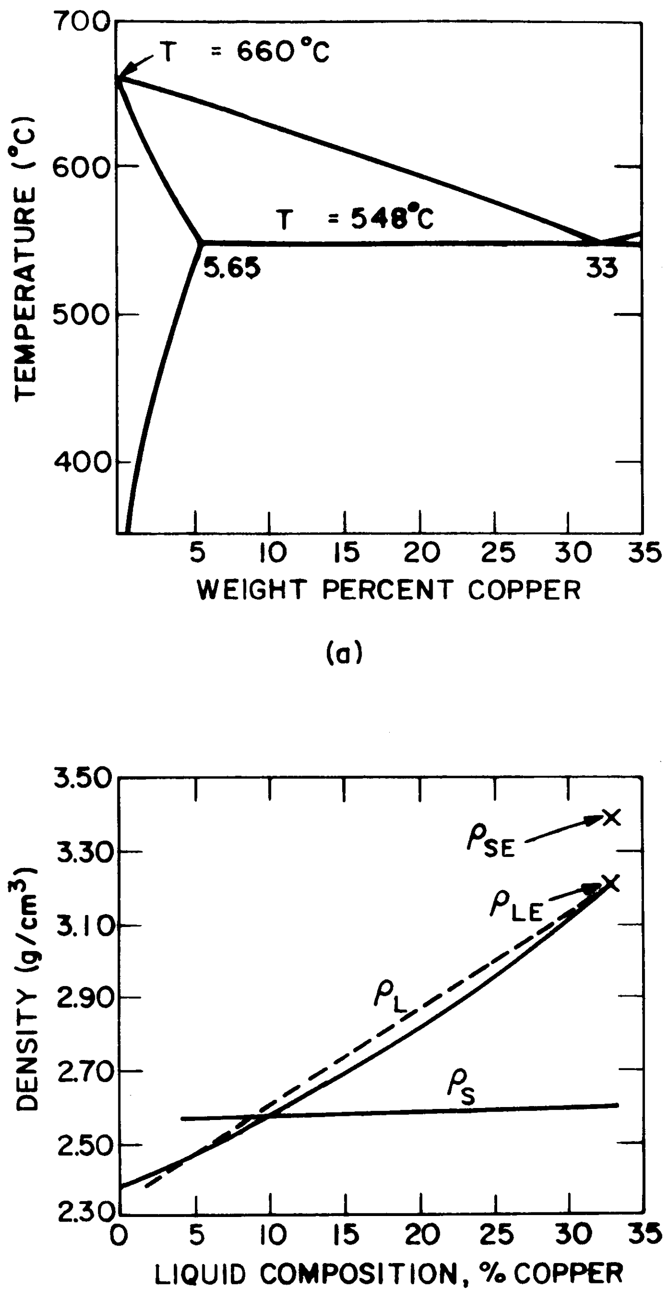

Figure 2: Phase diagram and density used for calculations of macrosegregation in Al-4% Cu ESR ingots. (a) Phase diagram, Ref. 39; (b) density of solid and liquid during solidification, Ref. 15.

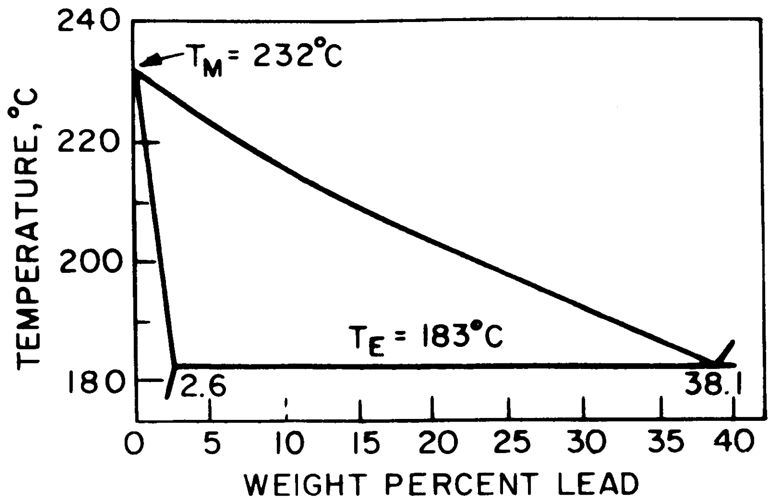

(a)

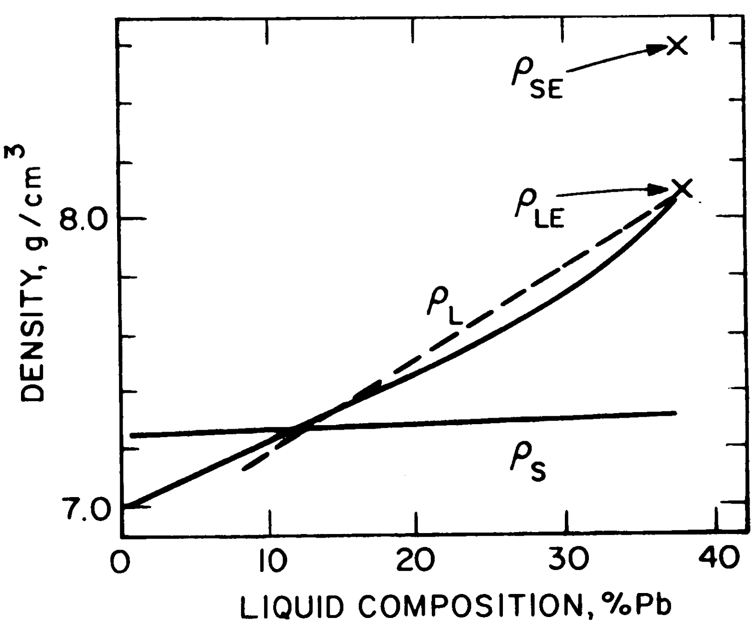

(b)

Figure 3: Tin-lead system. (a) Phase diagram (from ref. 40); (b) densities of solid and liquid phases during solidification computed with data from refs. 41-44.

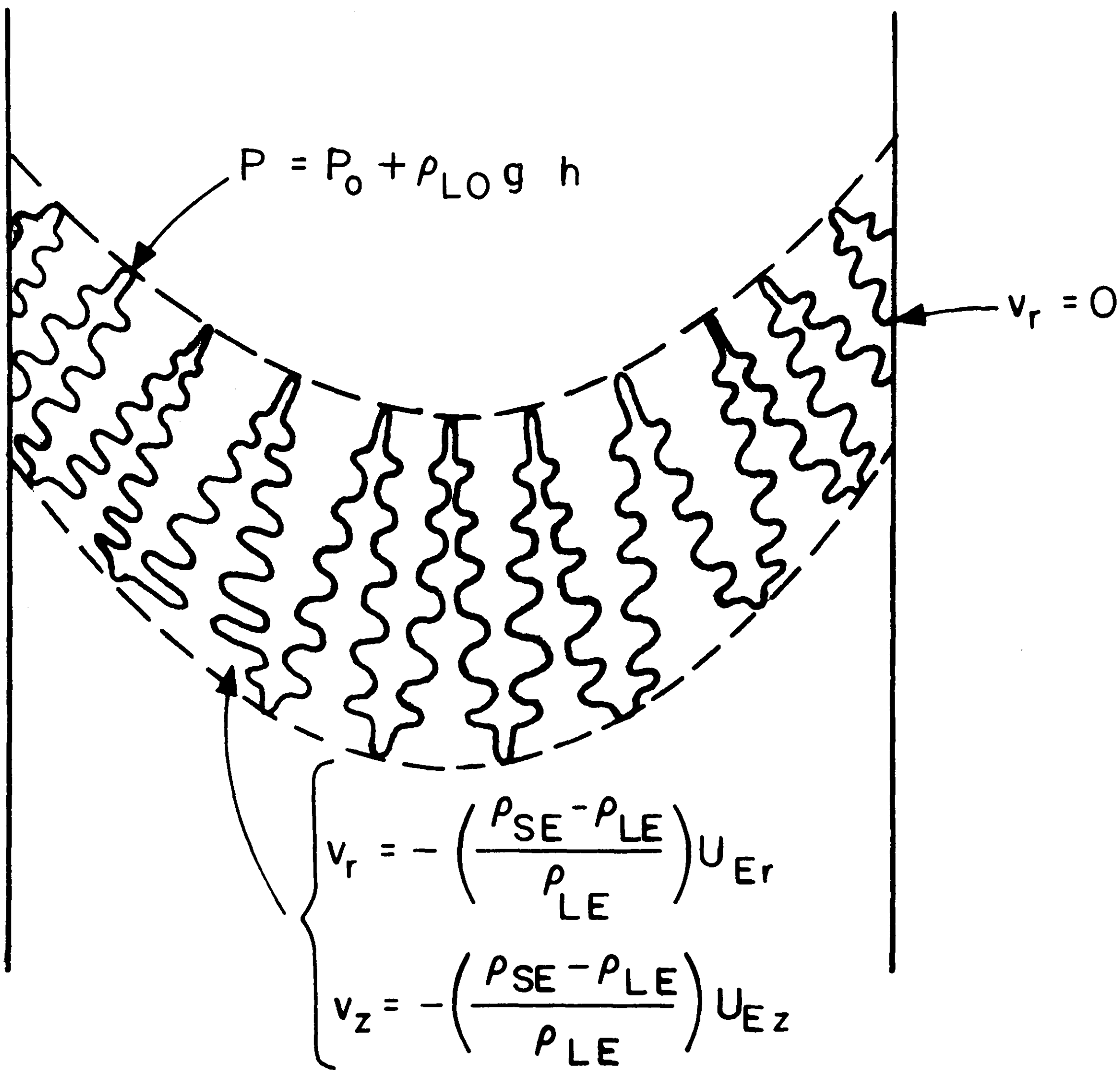

Figure 4: Boundary conditions used in solving for flow of interdendritic liquid

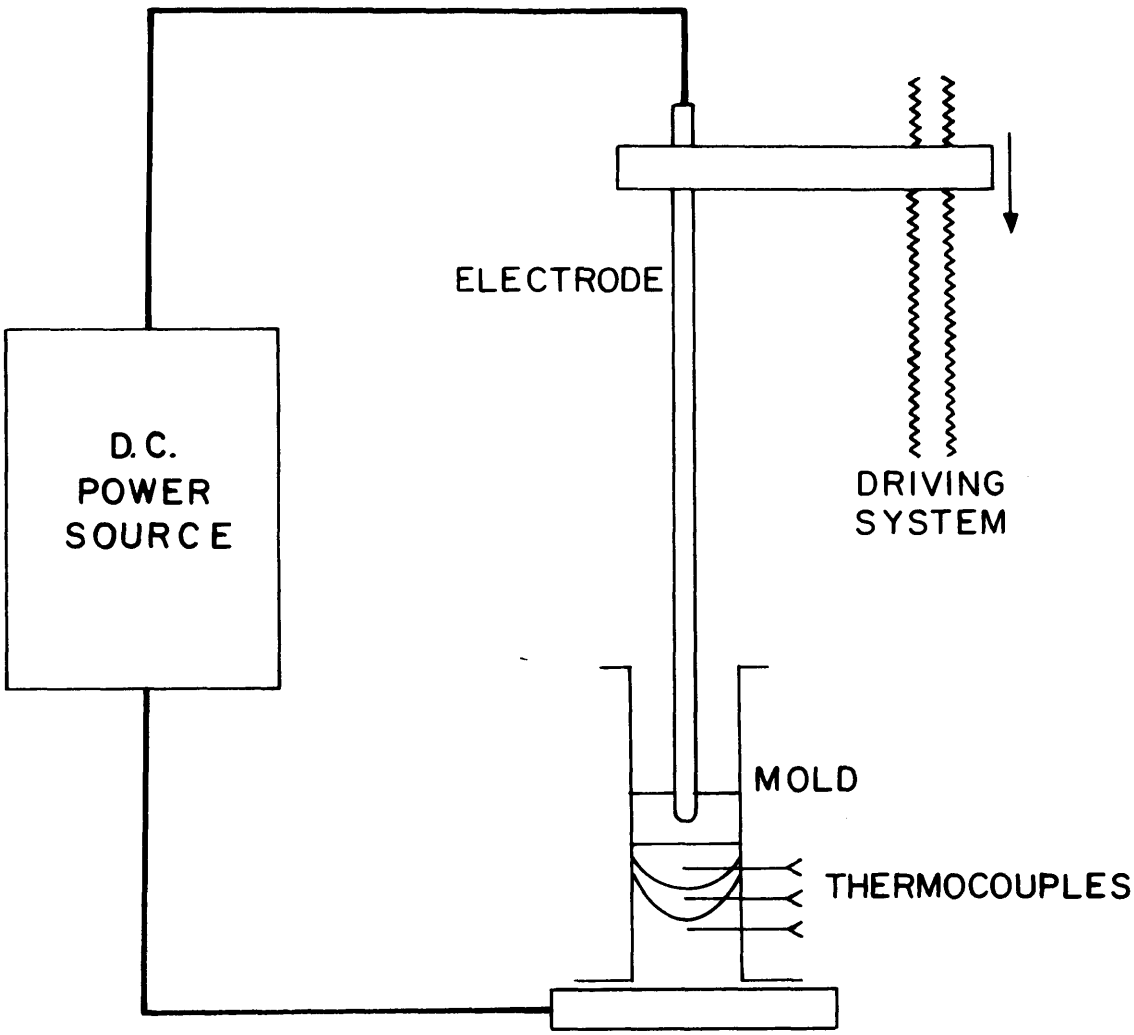

Figure 5: The experimental set-up used to study macro-segregation in Al-4% Cu ESR ingots

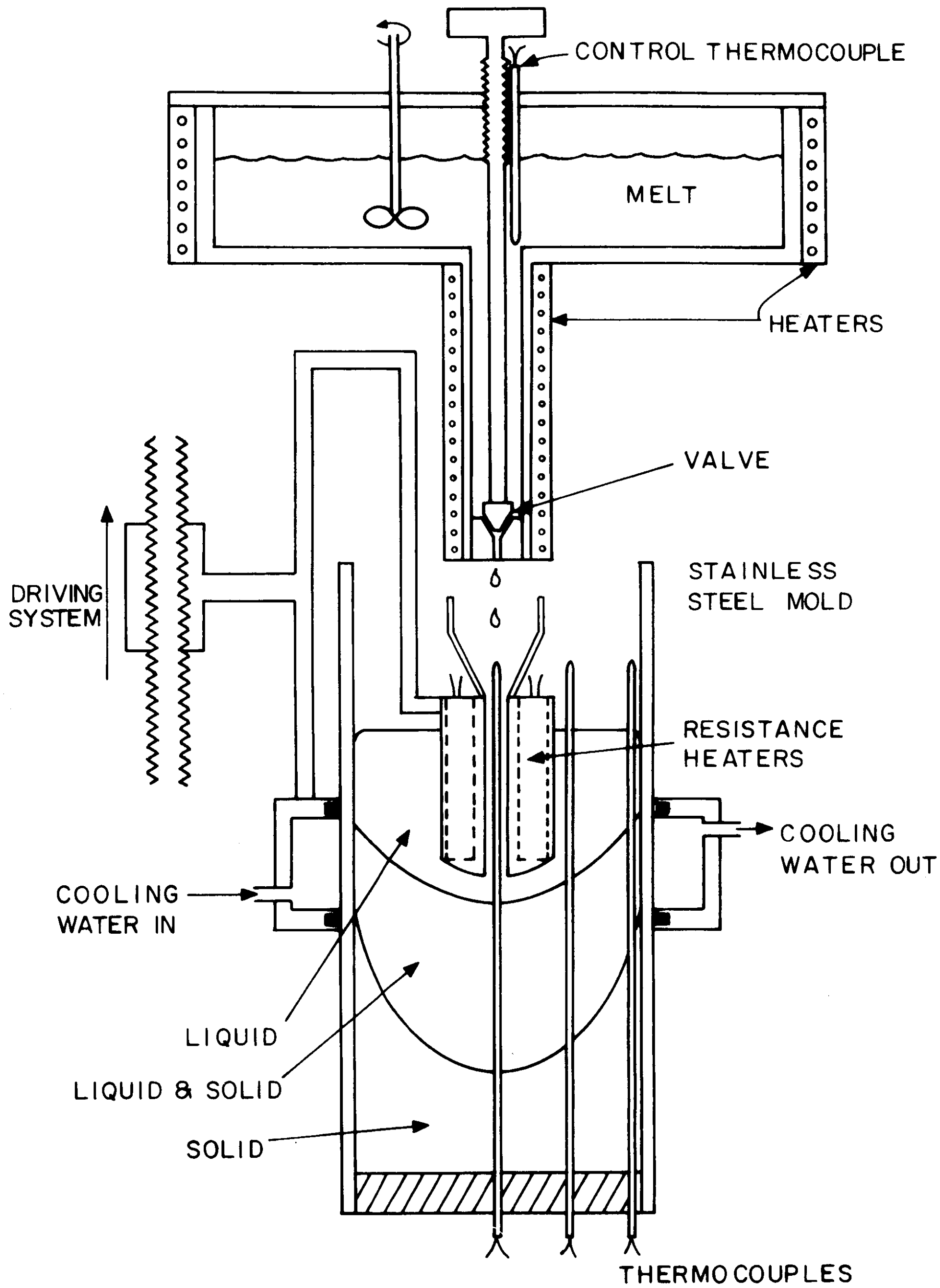

Figure 6: Apparatus used as an analog ESR process to produce Sn-15% Pb ingots.

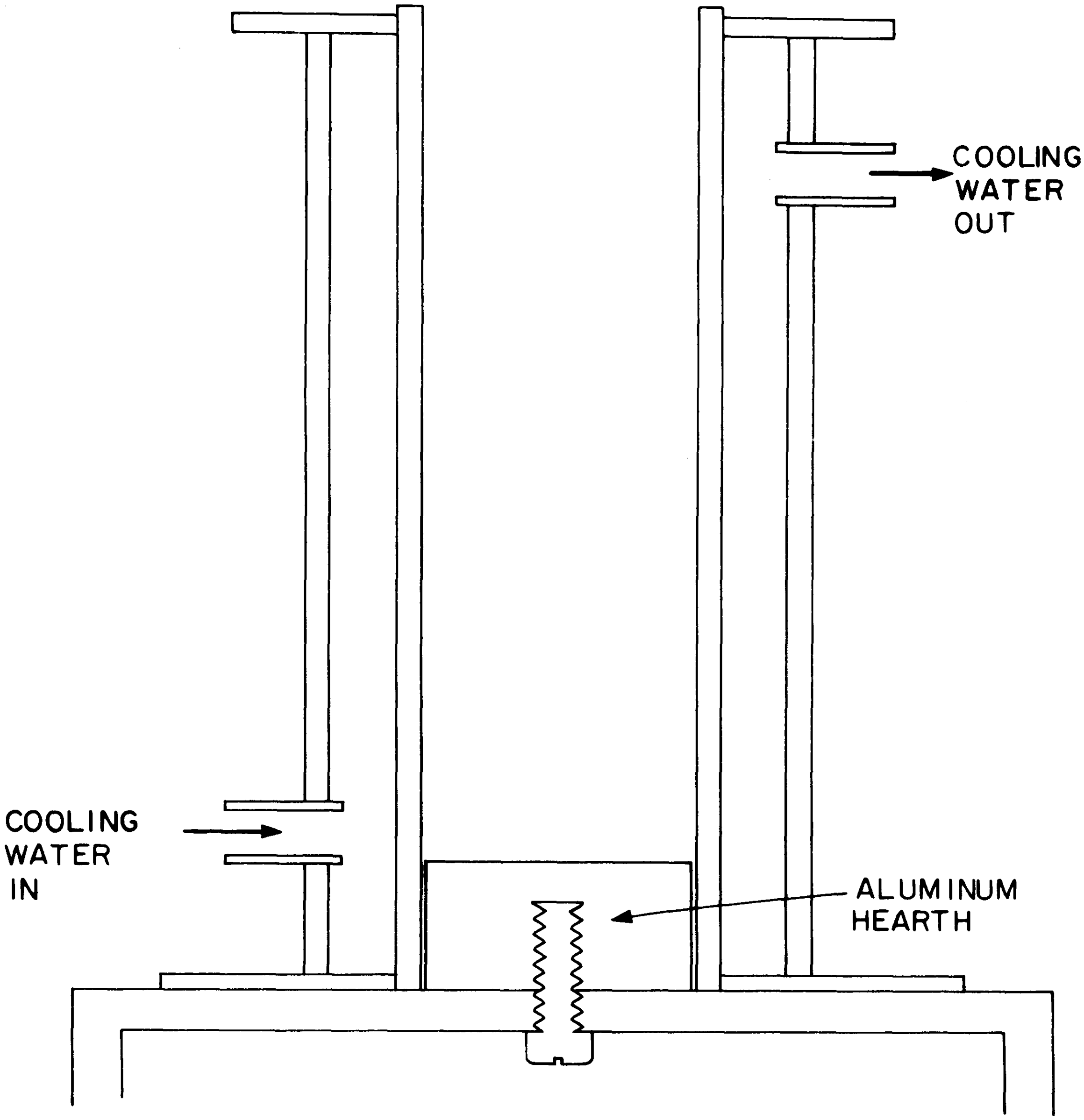

Figure 7: ESR mold design with brazed cooling-water jacket.

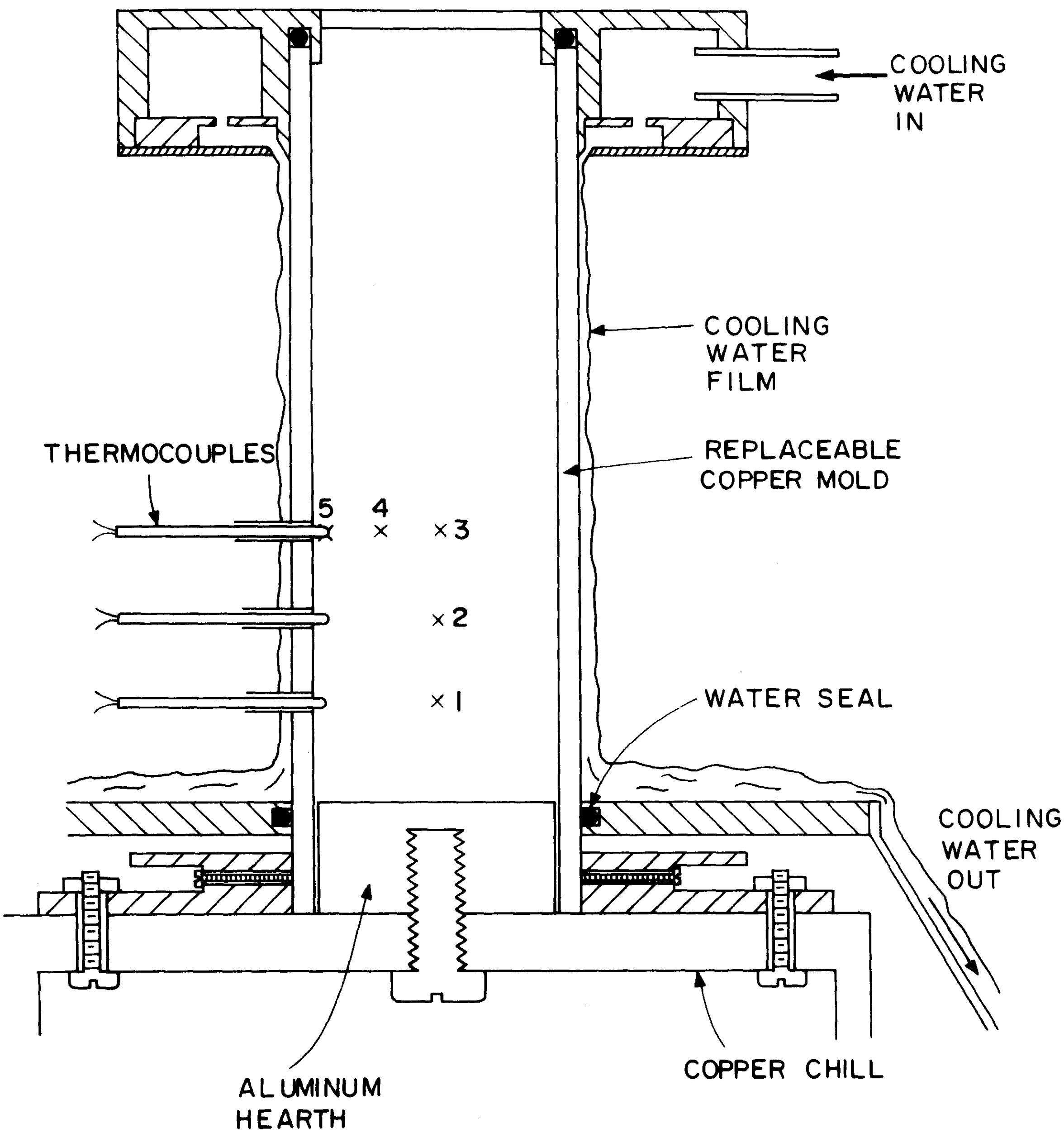

Figure 8: Design with replaceable mold wall. Numbers indicate thermocouples.

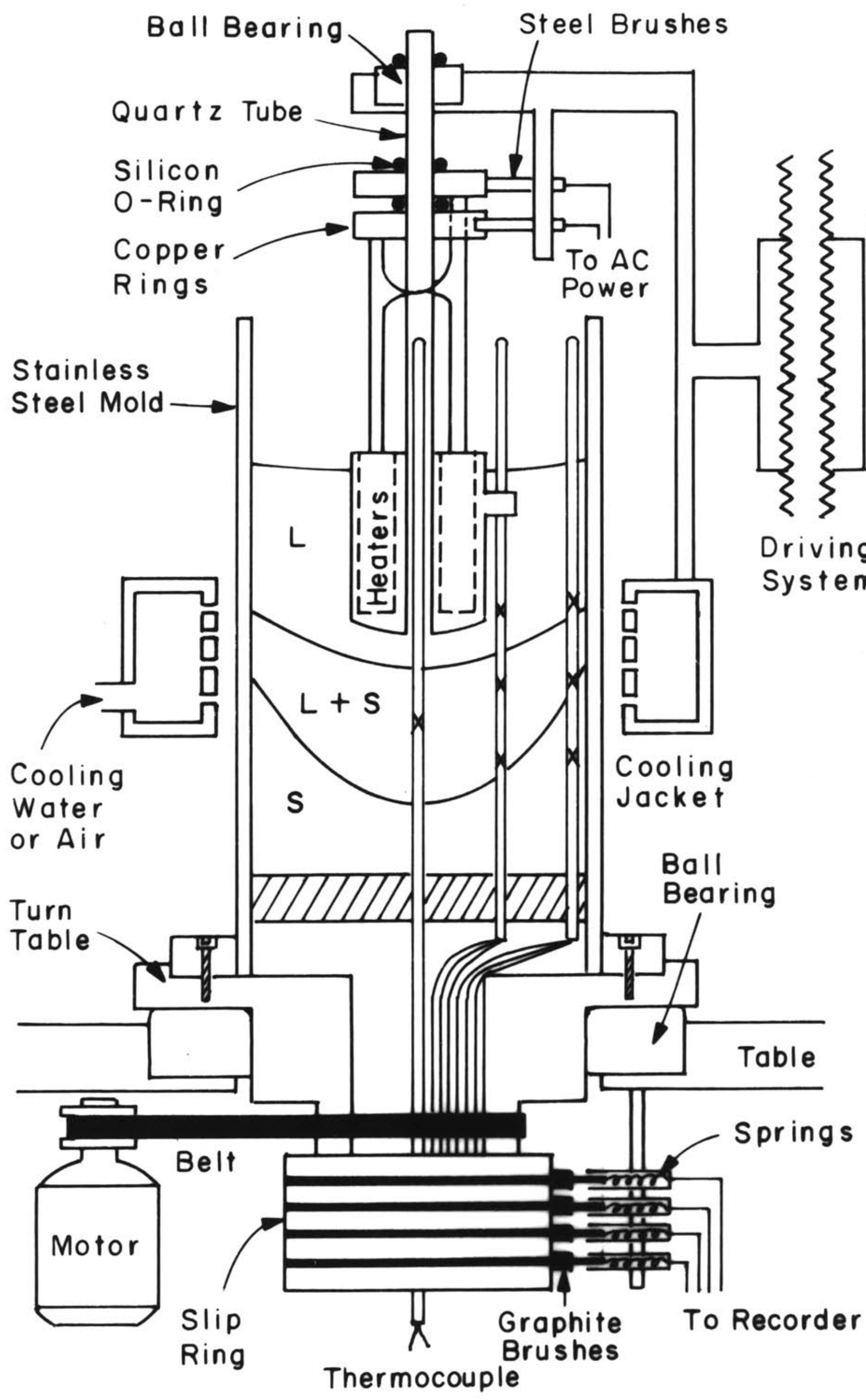

Figure 9: Apparatus used as an analog ESR process to produce Sn-Pb ingots with mold rotation.

Table I. Results of Al - Cu Ingots

Ingot #	1	3	2
Solid'n Rate	5.3×10^{-2} cm/sec	4.0×10^{-2} cm/sec	3.2×10^{-2} cm/sec
Shape of Mushy Zone	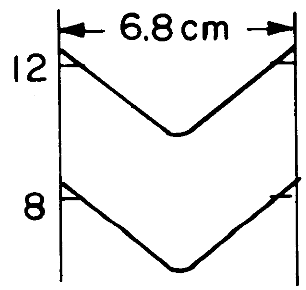	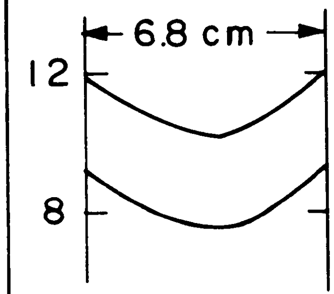	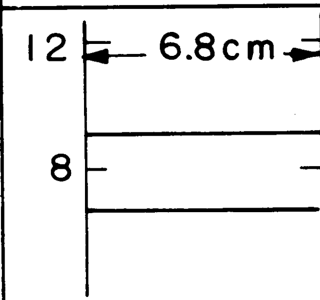
Macrosegre-gation	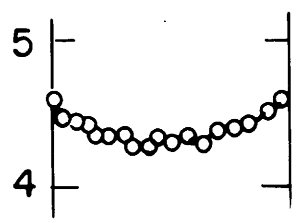	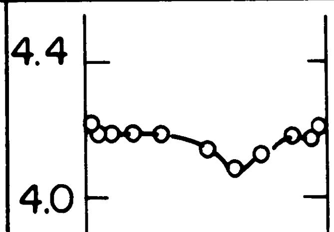	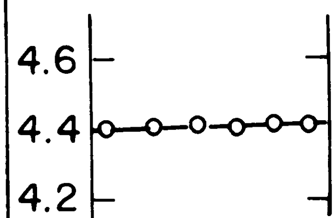
Freckle	No	No	No
Solid'n Time	68 sec	68 sec	70 sec
Comment	← Increasing Depth of Mushy Zone Increasing "—" ℄ Macrosegregation		

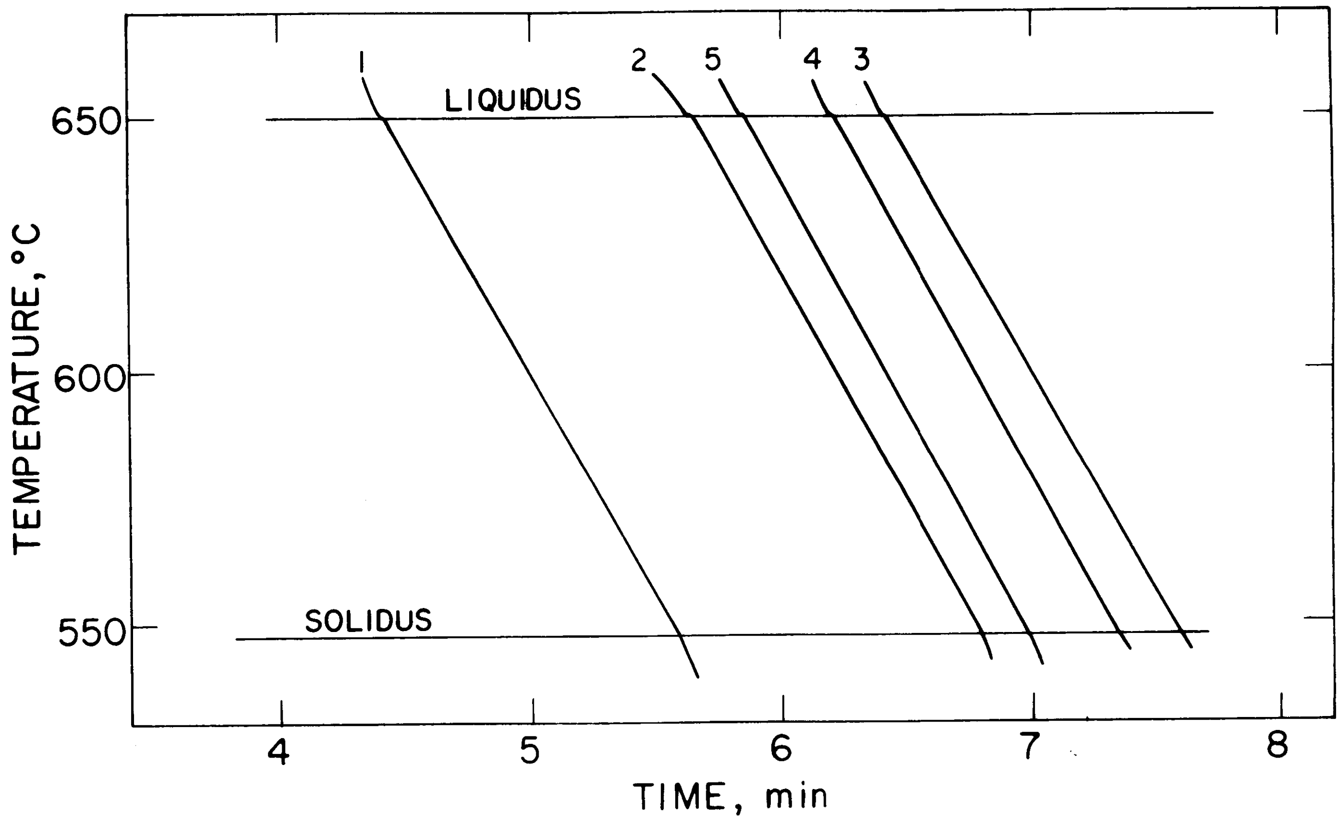

Figure 10: Cooling curves for Ingot 1 (Al-4.4% Cu). Numbers refer to thermocouples shown in Figure 8.

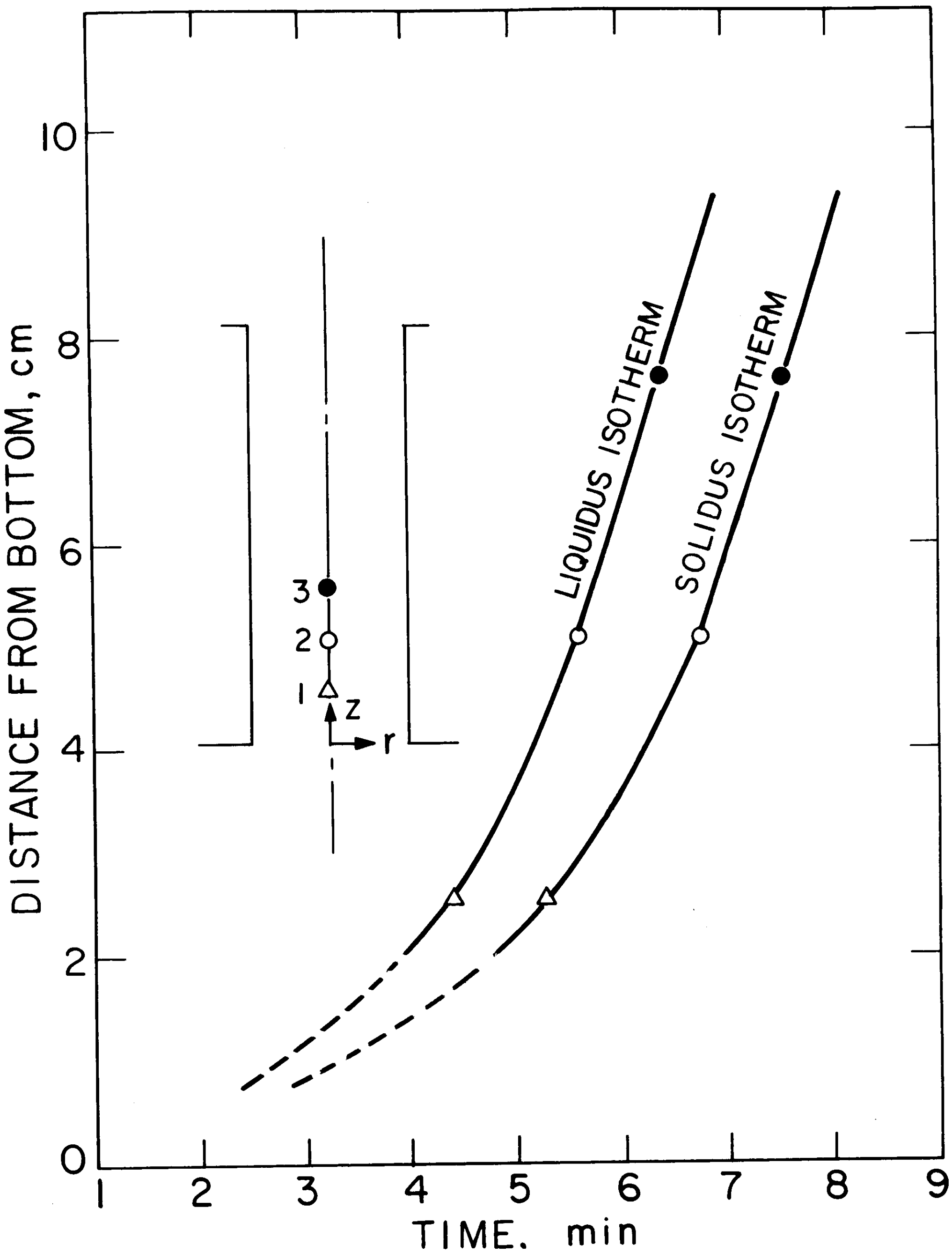

Figure 11: Liquidus and solidus isotherms along axis in Ingot 1 (Al-4.4% Cu).

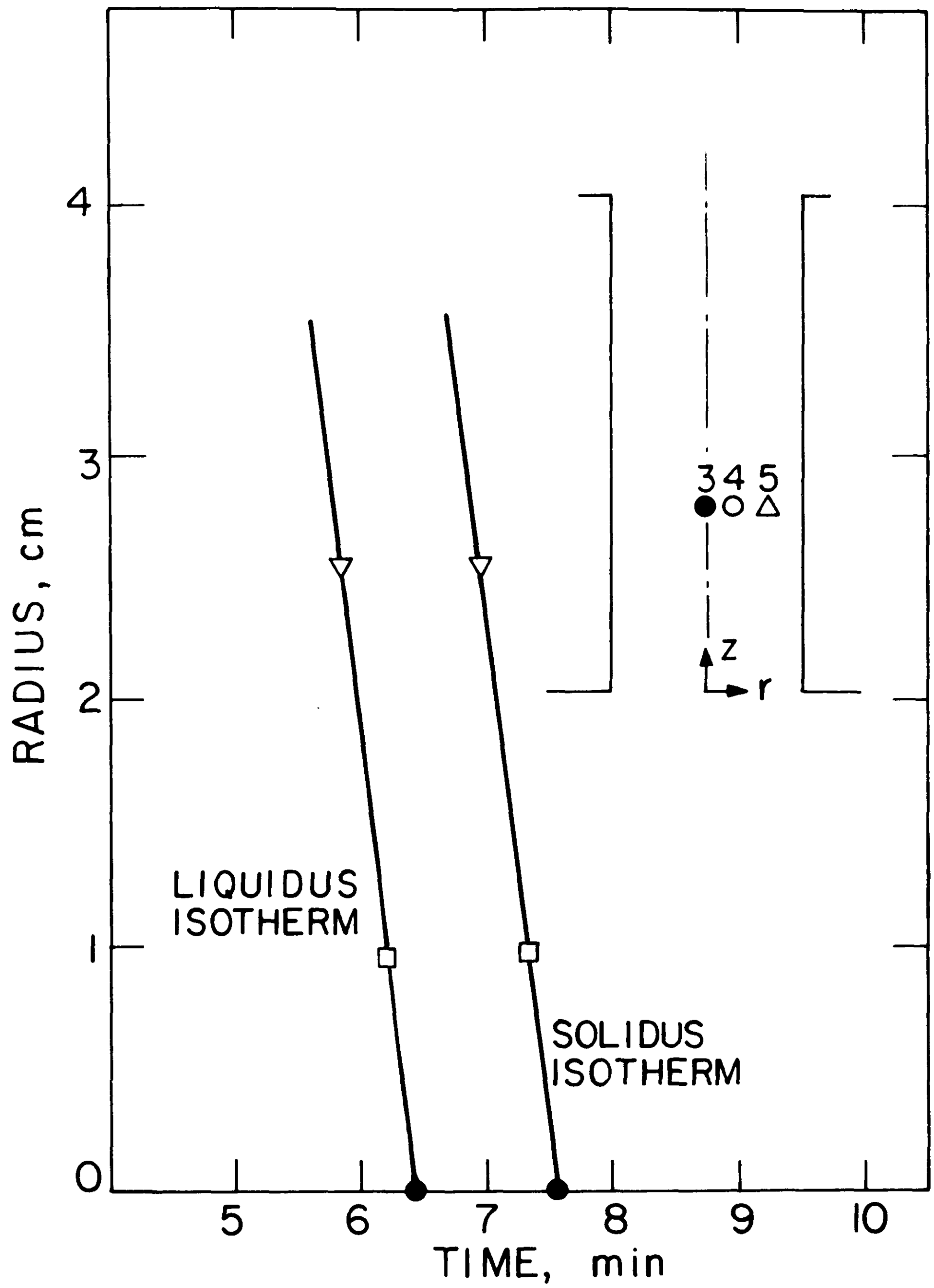

Figure 12: Liquidus and solidus isotherms with respect to radius at 7.6 cm from the bottom in Ingot 1 (Al-4.4% Cu).

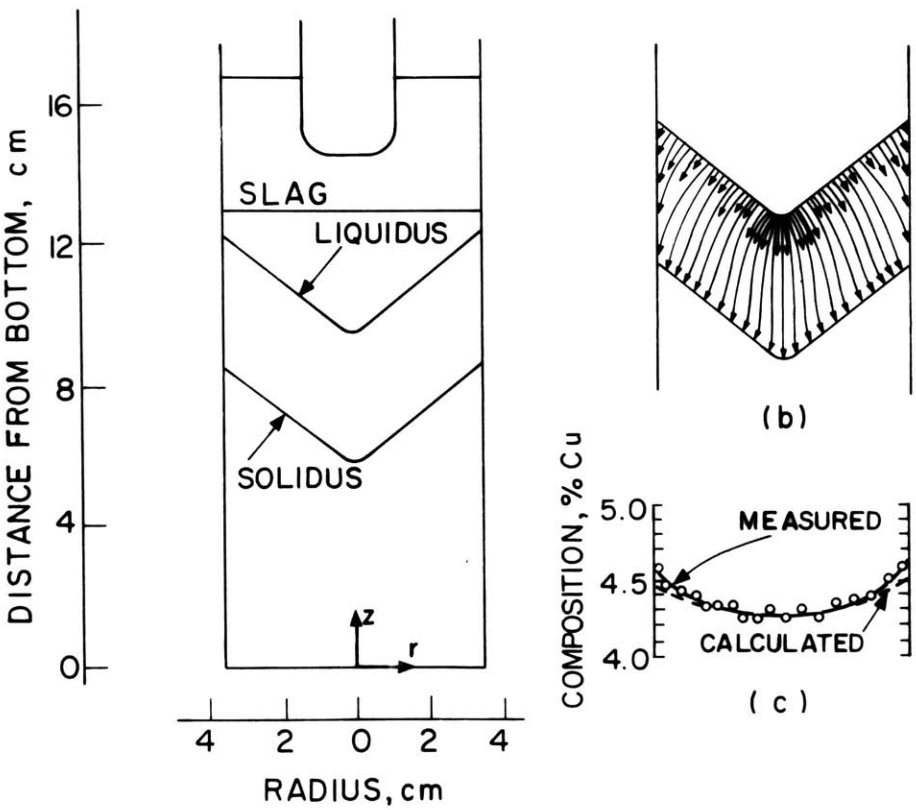

Figure 13: Results obtained for Ingot 1 (Al-4.4%CU).
(a) Liquidus and solidus isotherms after 7 min.;
(b) flow lines of interdendritic liquid;
(c) macrosegregation as measured (solid curve)
and calculated with $\gamma = 5 \times 10^{-7}$ cm^2 (broken curve).

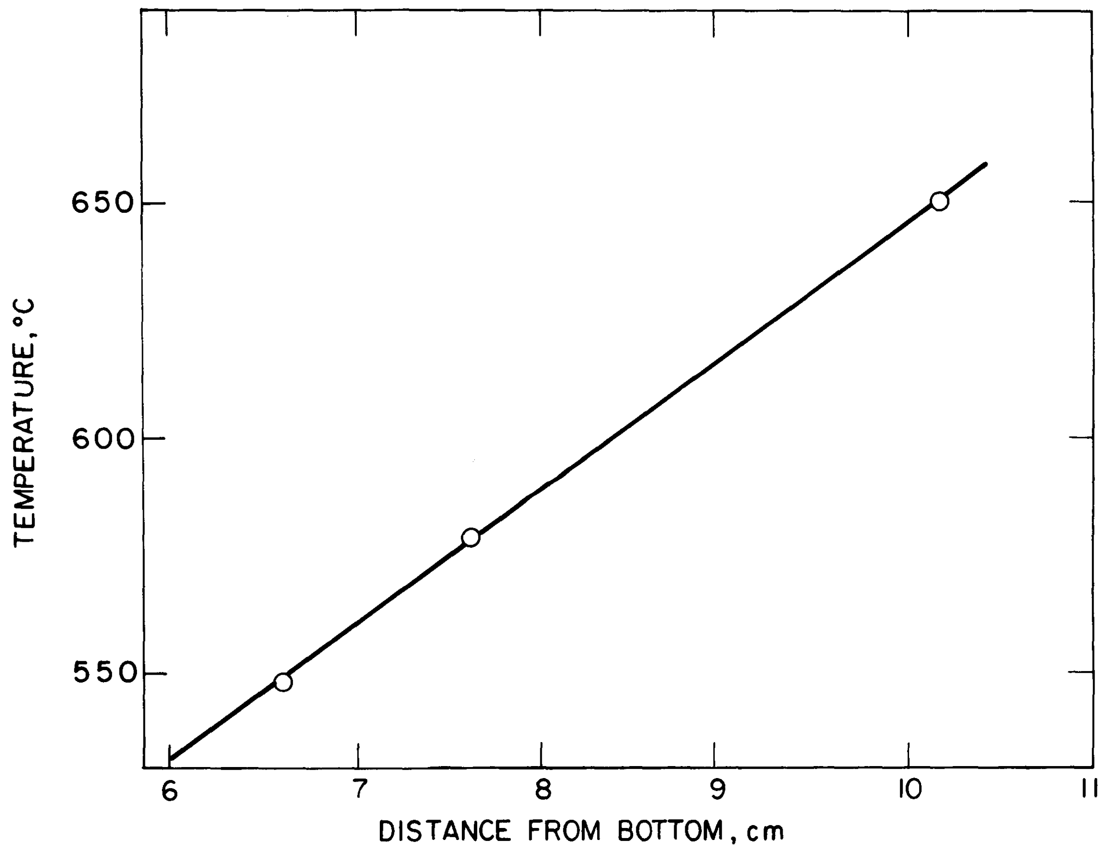

Figure 14: The temperature gradient in Ingot 1 (Al-4.4%Cu).

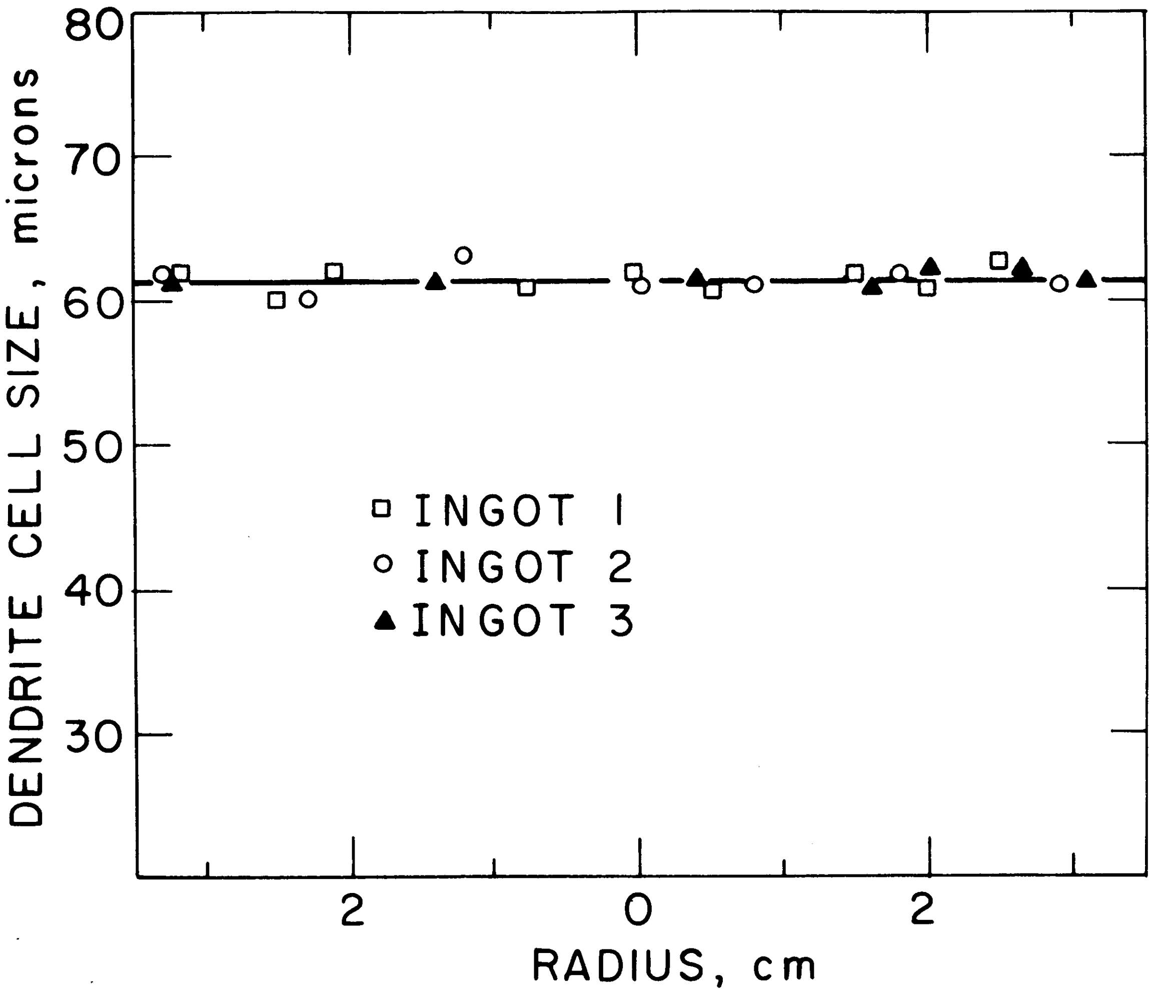

Figure 15: Dendrite cell sizes in the Al-4% Cu ingots.

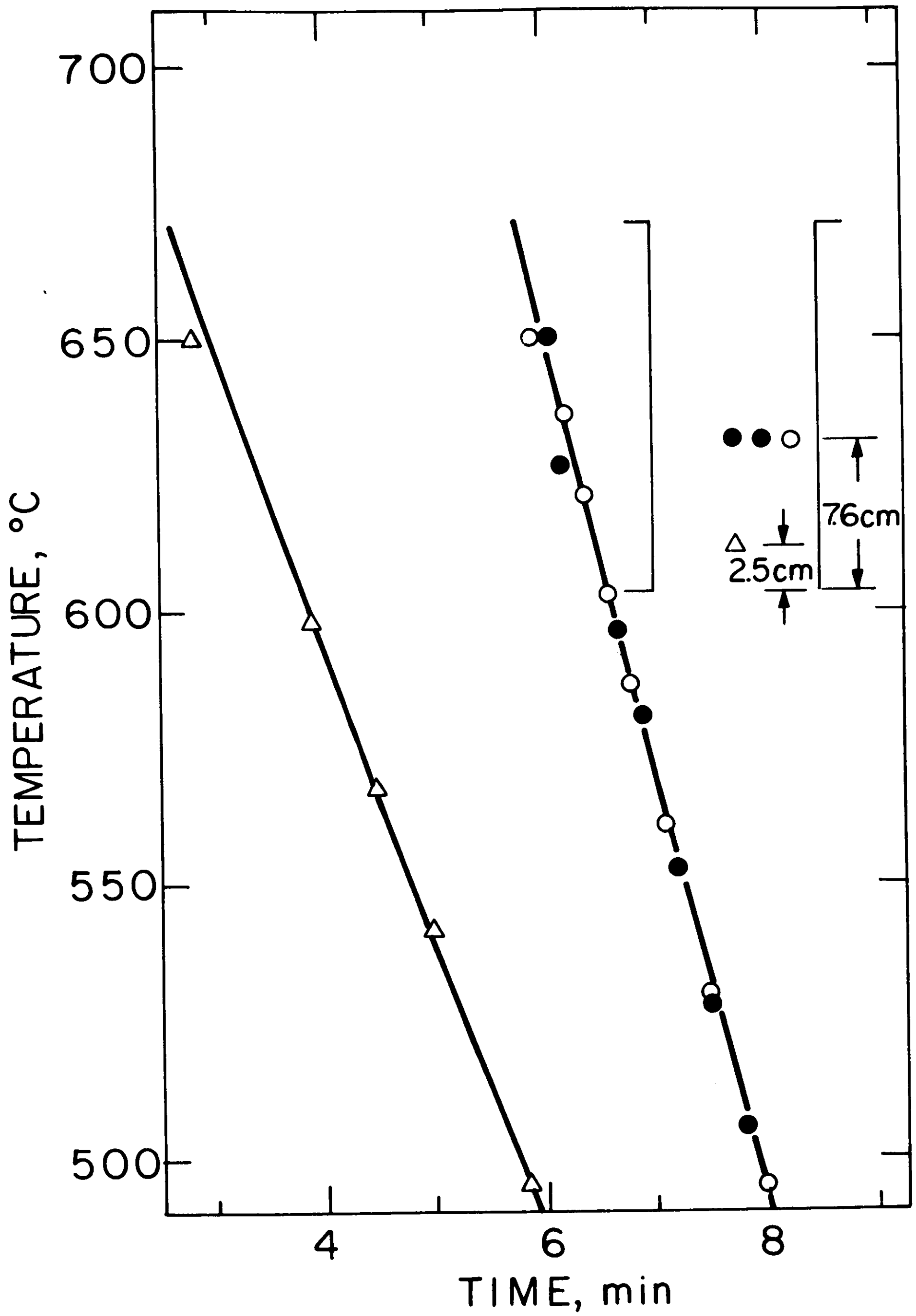

Figure 16: Cooling curves for Ingot 2 (Al-4.4% Cu).

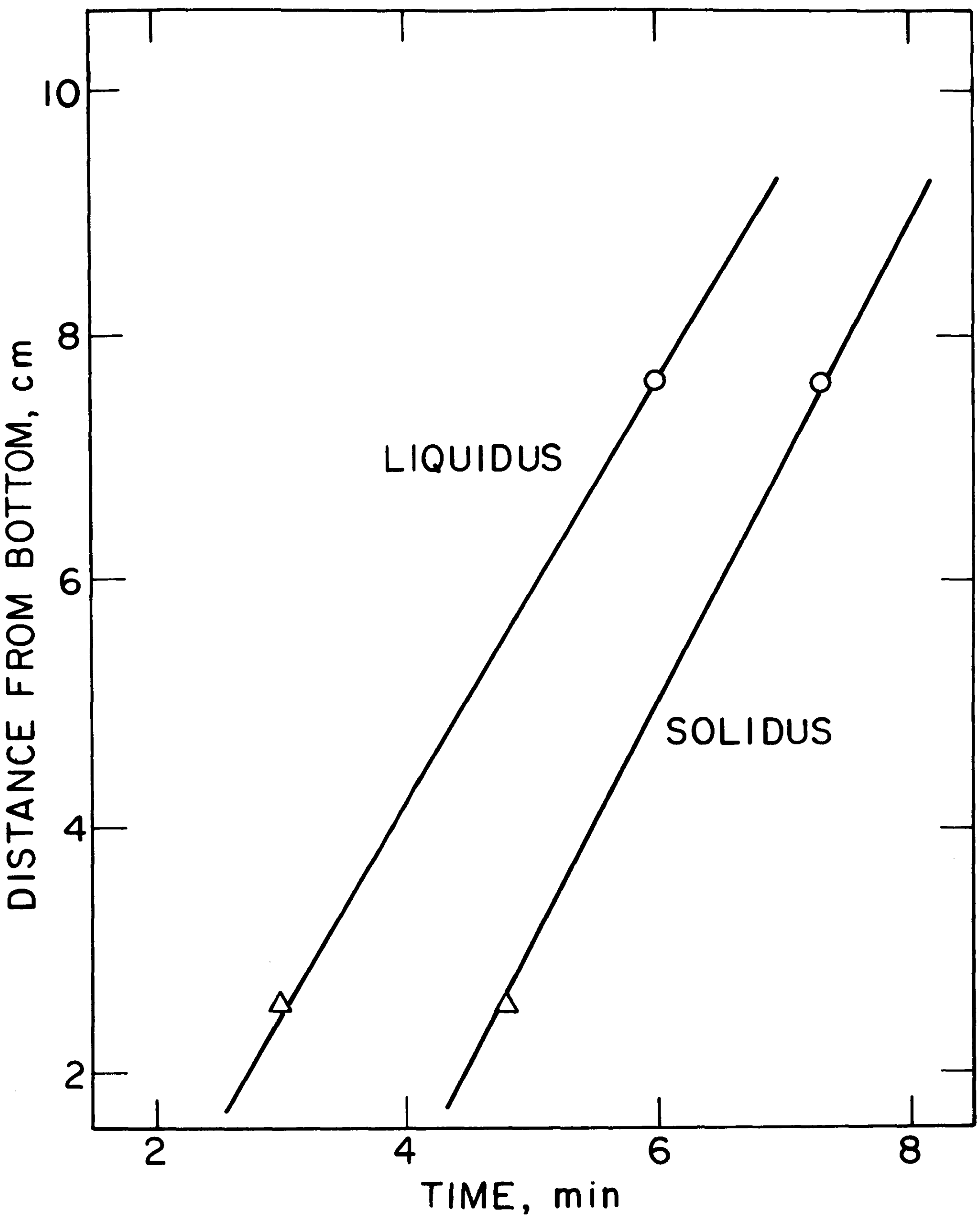

Figure 17: The liquidus and solidus isotherms in Ingot 2 (Al-4.4% Cu).

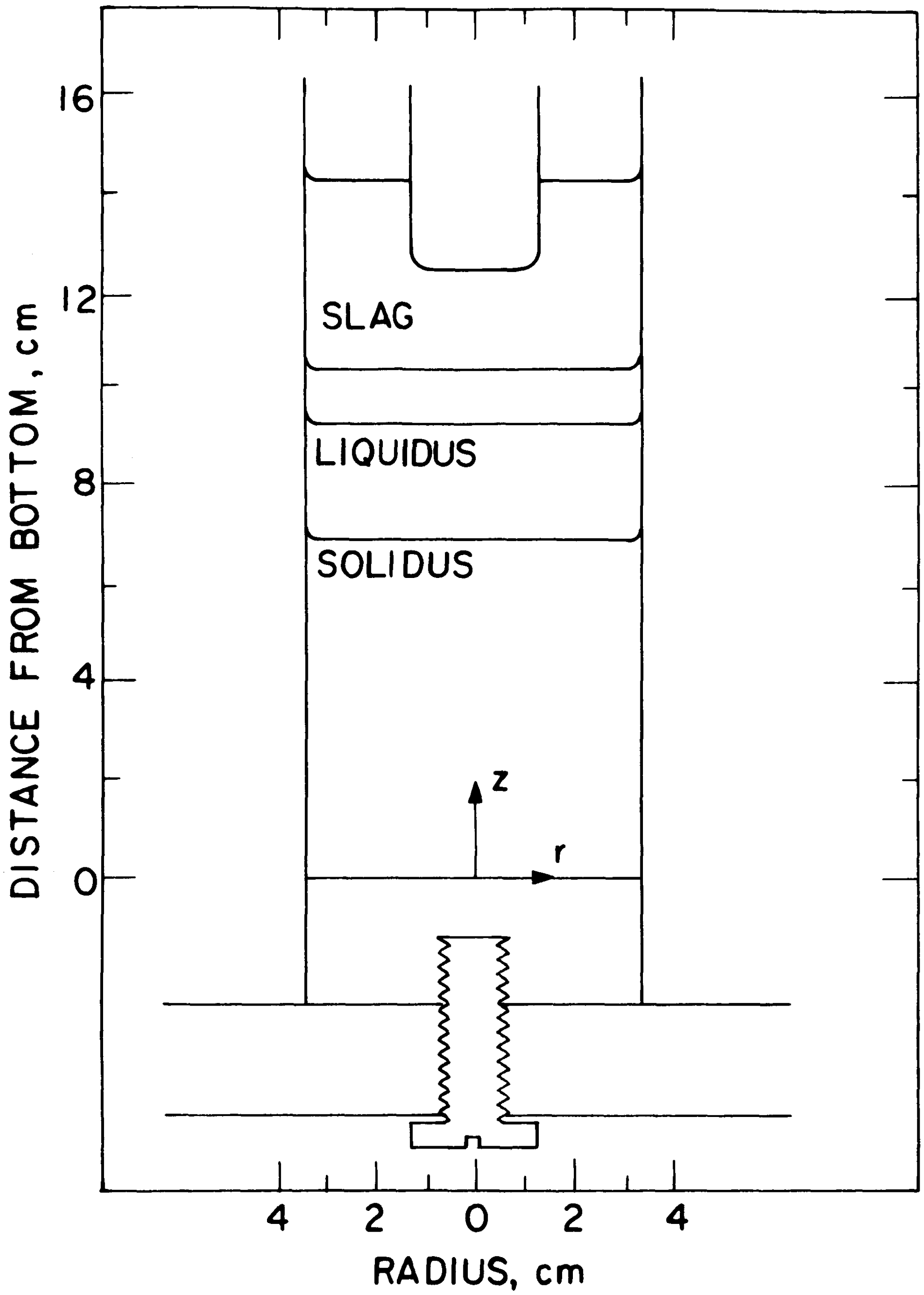

Figure 18: The shape of the mushy zone at 7 minutes in Ingot 2 (Al-4.4% Cu).

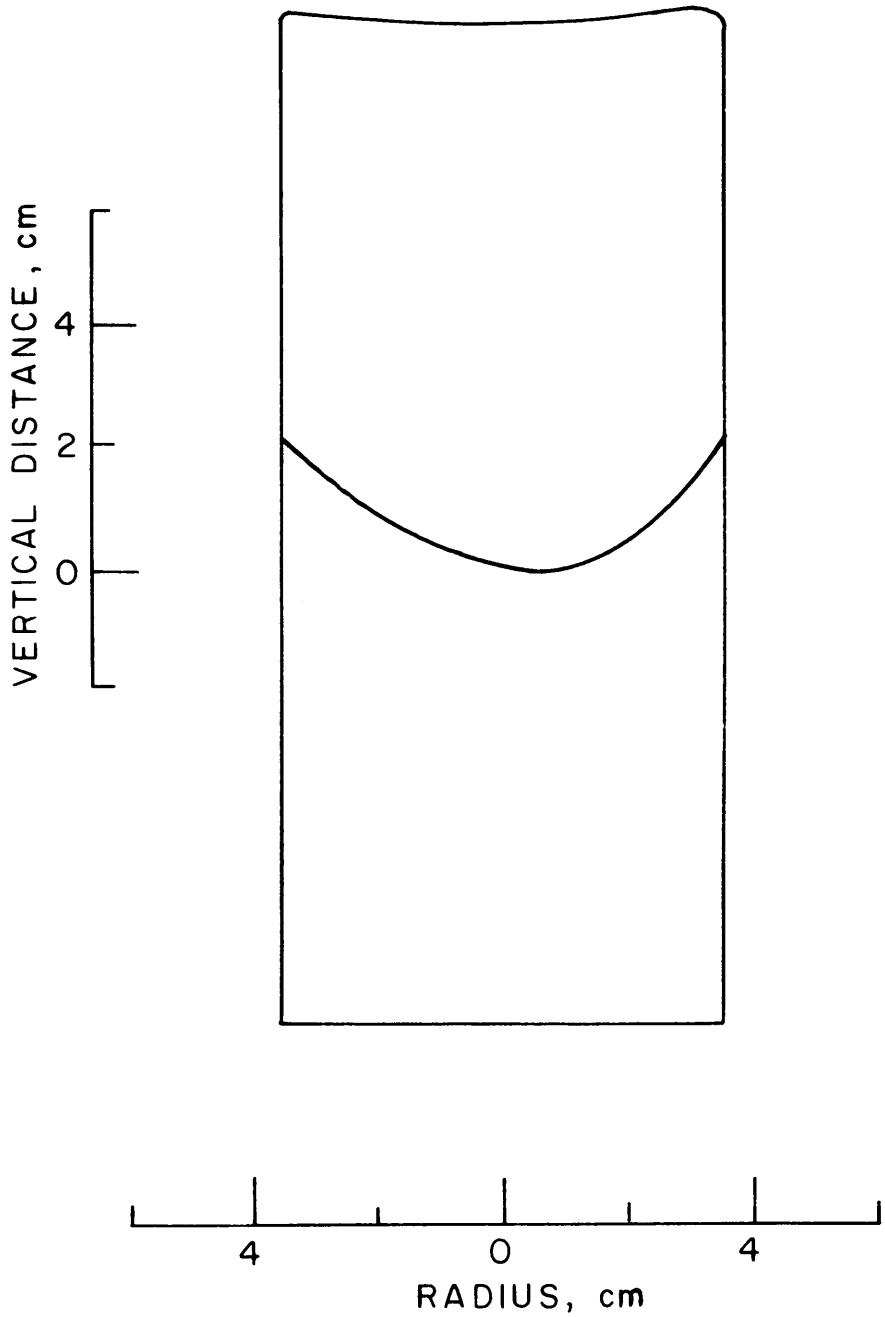

Figure 19: Isotherm detected by doping Ingot 3 (Al-4.2% Cu).

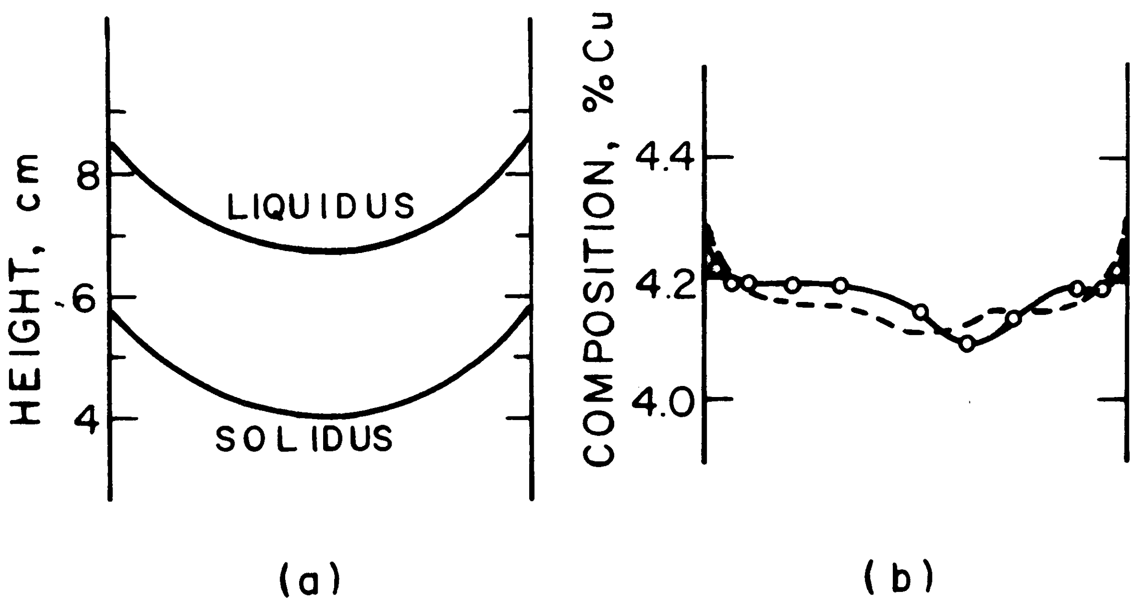

Figure 20: Ingot 3 (Al-4.2% Cu). (a) Position of isotherms used for calculations; (b) macrosegregation by experiment (solid curve) and by calculation with $\gamma = 3 \times 10^{-7}$ cm^2 (broken curve).

Table 2. Results of Sn-Pb Ingots without Rotation

Ingot #	4	5	6
Solid'n Rate	4.0×10^{-3} cm/sec	7.0×10^{-3} cm/sec	5.1×10^{-3} cm/sec
Shape of Mushy Zone	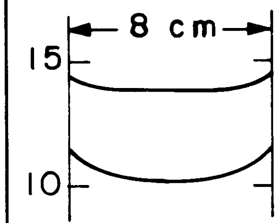	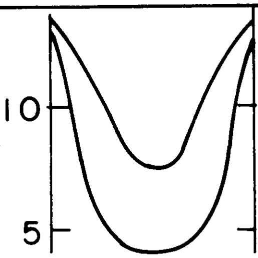	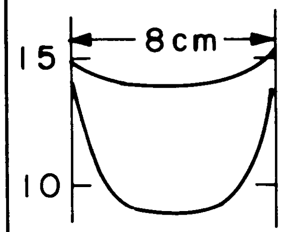
Macrosegregation	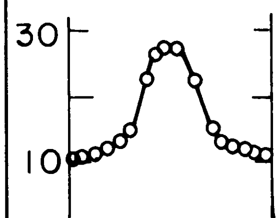	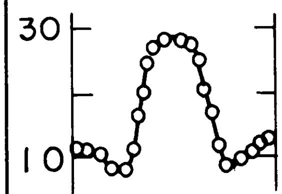	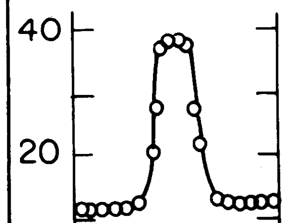
Freckle (Transverse Cross Section)	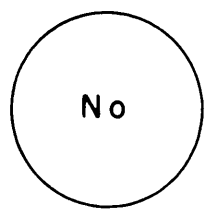	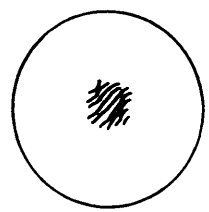	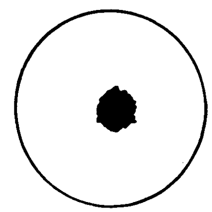
Solid'n Time	900 sec at ℄	457 sec at ℄	980 sec at ℄
Comment	Flat Mushy Zone	Steep Mushy Zone Shorter Solid'n Time	Steep Mushy Zone Longer Solid'n Time
	Increasing "+" ℄ Macrosegregation →		

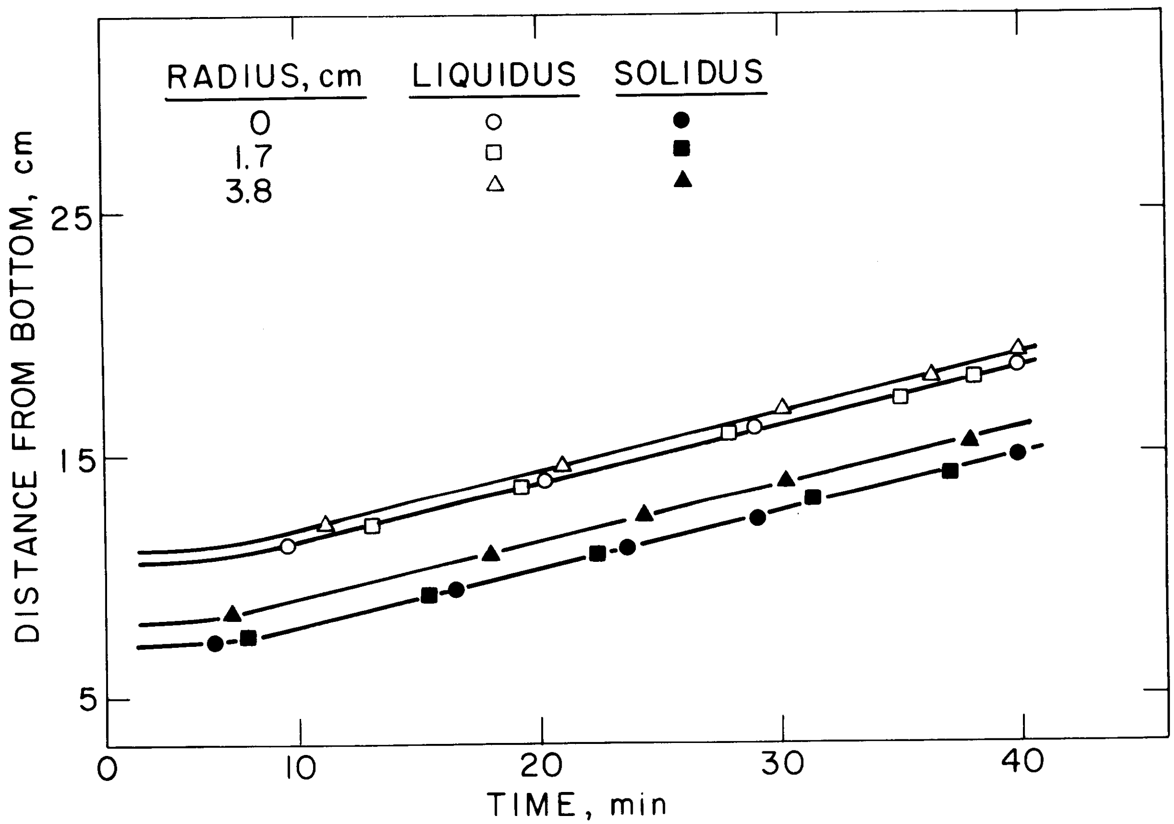

Figure 21: Positions of the liquidus and solidus isotherms in Ingot 4.

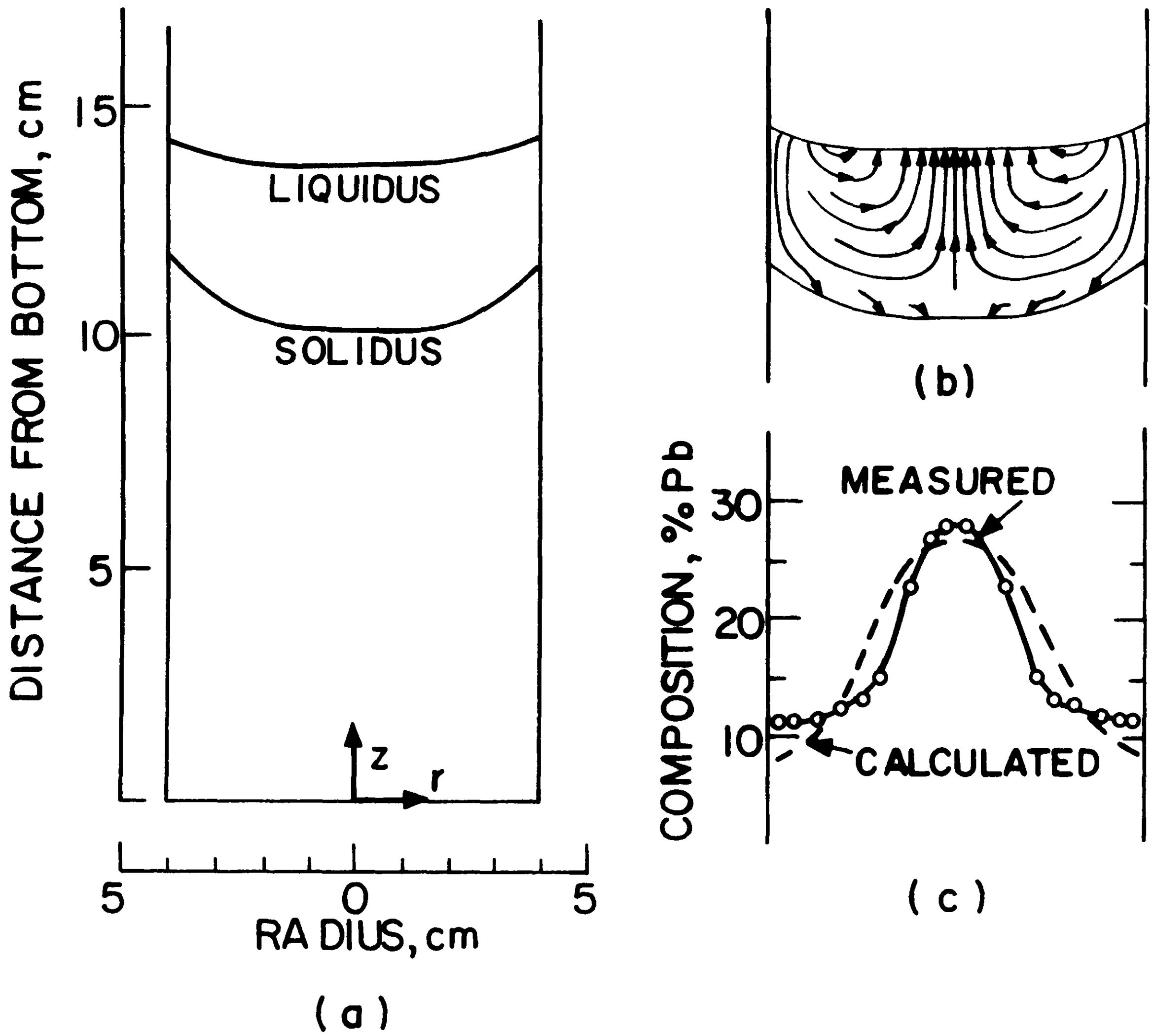

Figure 22: Results obtained for Ingot 4 (Sn-15% Pb).
(a) Liquidus and solidus isotherms after 25 minutes;
(b) flow lines of interdendritic liquid;
(c) macrosegregation as measured (solid curve) and calculated with $\gamma_o = 3.7 \times 10^{-6}$ cm^2 (broken curve)

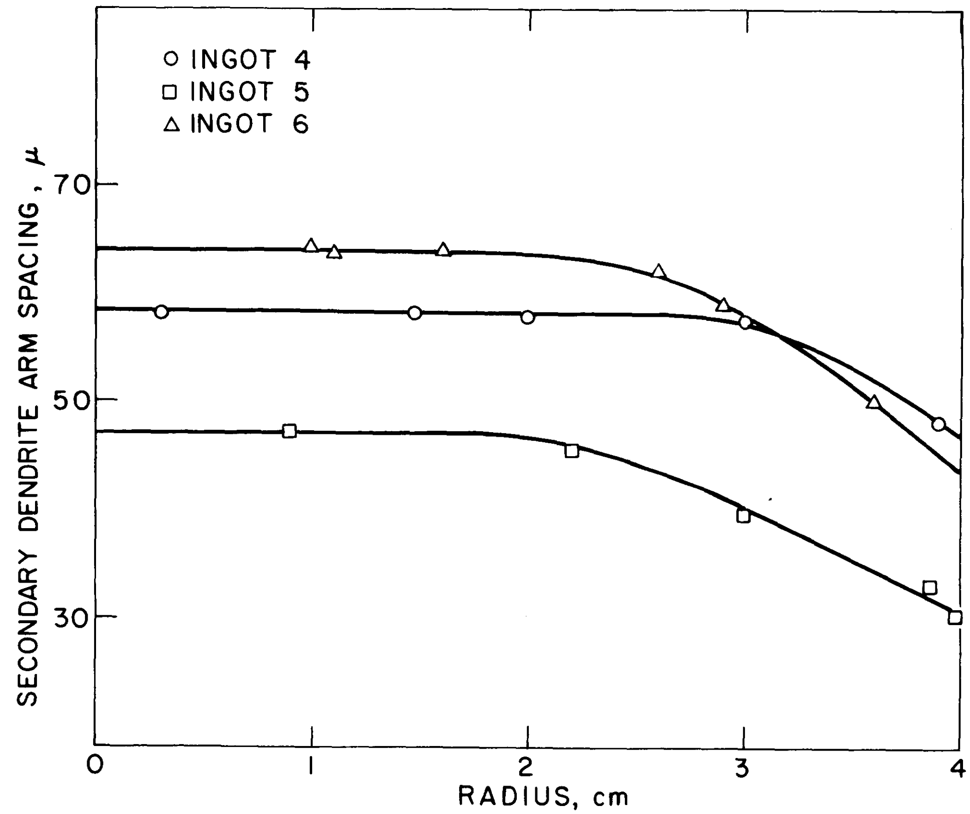

Figure 23: Secondary dendrite arm spacings in Ingots 4, 5 and 6.

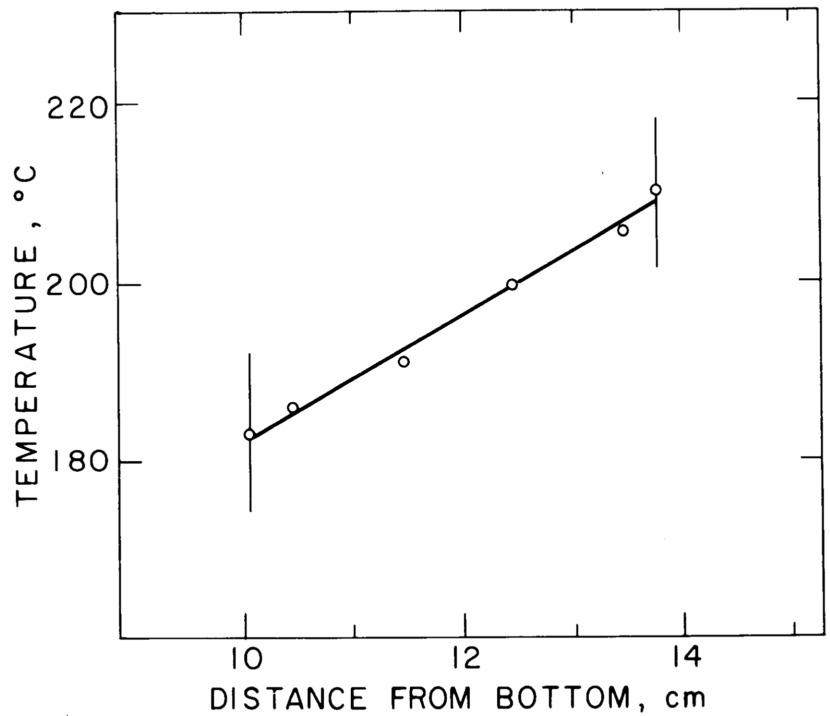

Figure 24: The temperature gradient in Ingot 4.

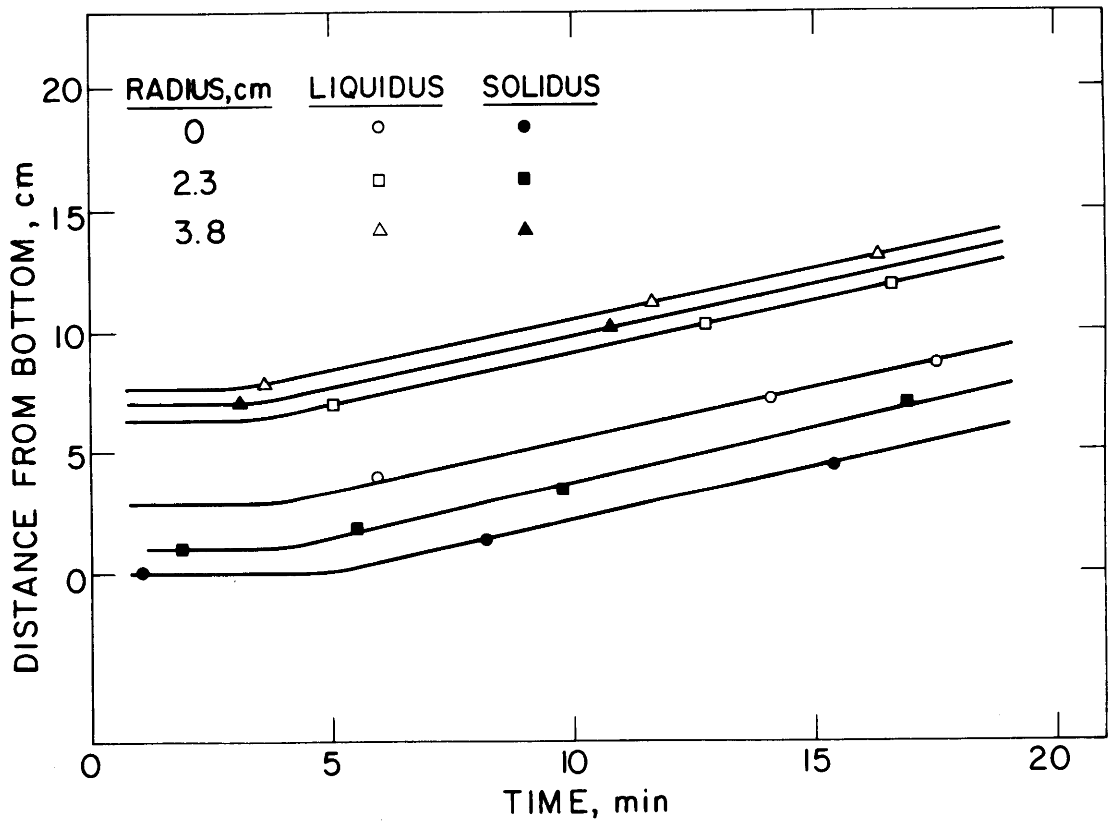

Figure 25: Position of the liquidus and solidus isotherms in Ingot 5.

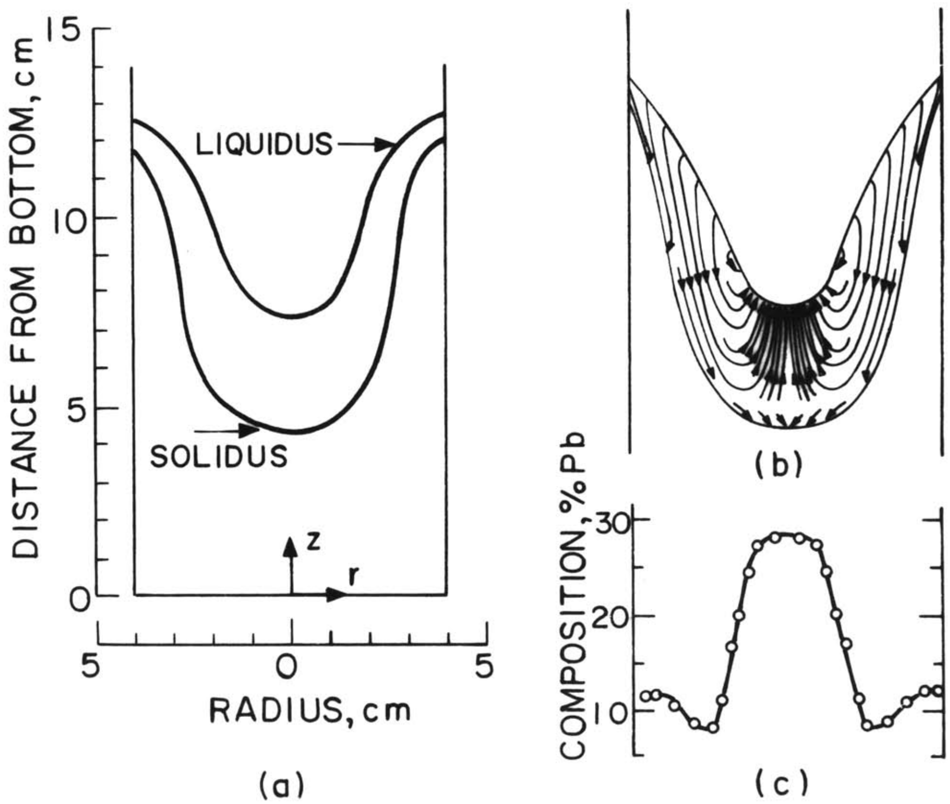

Figure 26: Results obtained for Ingot 5 (Sn-15%Pb).

(a) Liquidus and solidus isotherms after 14 minutes;
(b) calculated flow lines of interdendritic liquid with $\gamma_o = 2 \times 10^{-7}$ cm^2; (c) macrosegregation as measured.

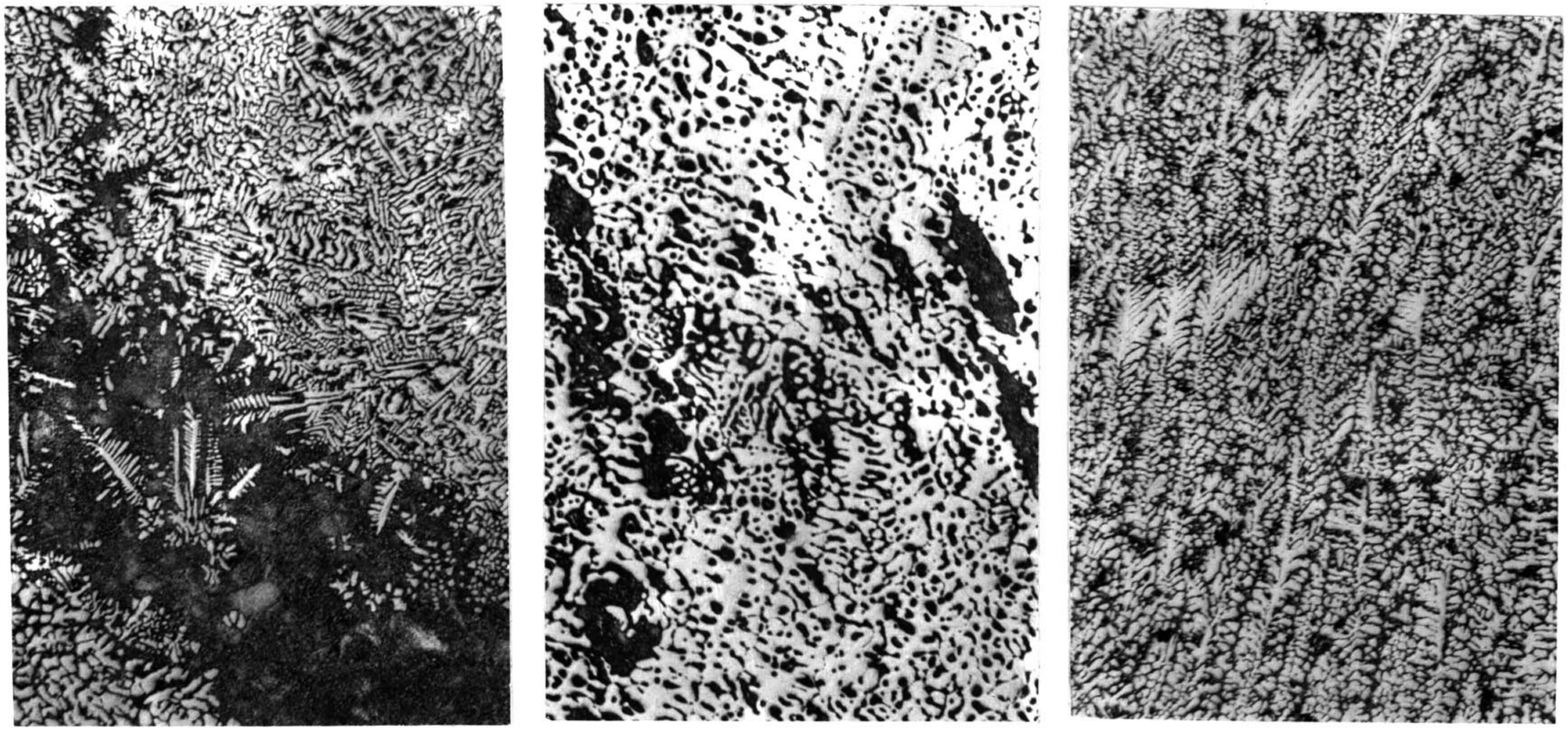

a b c

Figure 27: Longitudinal microsections of Ingot 5 (Sn-15% Pb). (a) center; (b) 1.5 cm radius; (c) near surface. Mag. 25.6X.

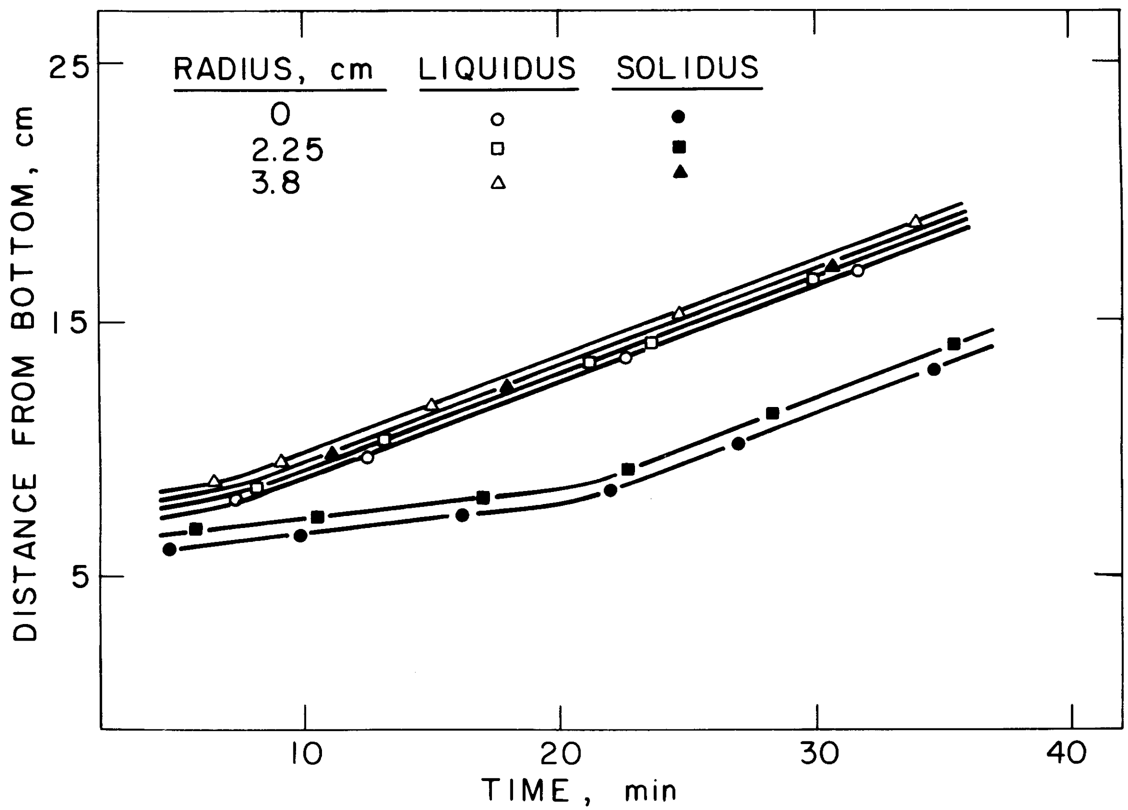

Figure 28: Position of the liquidus and solidus isotherms in Ingot 6.

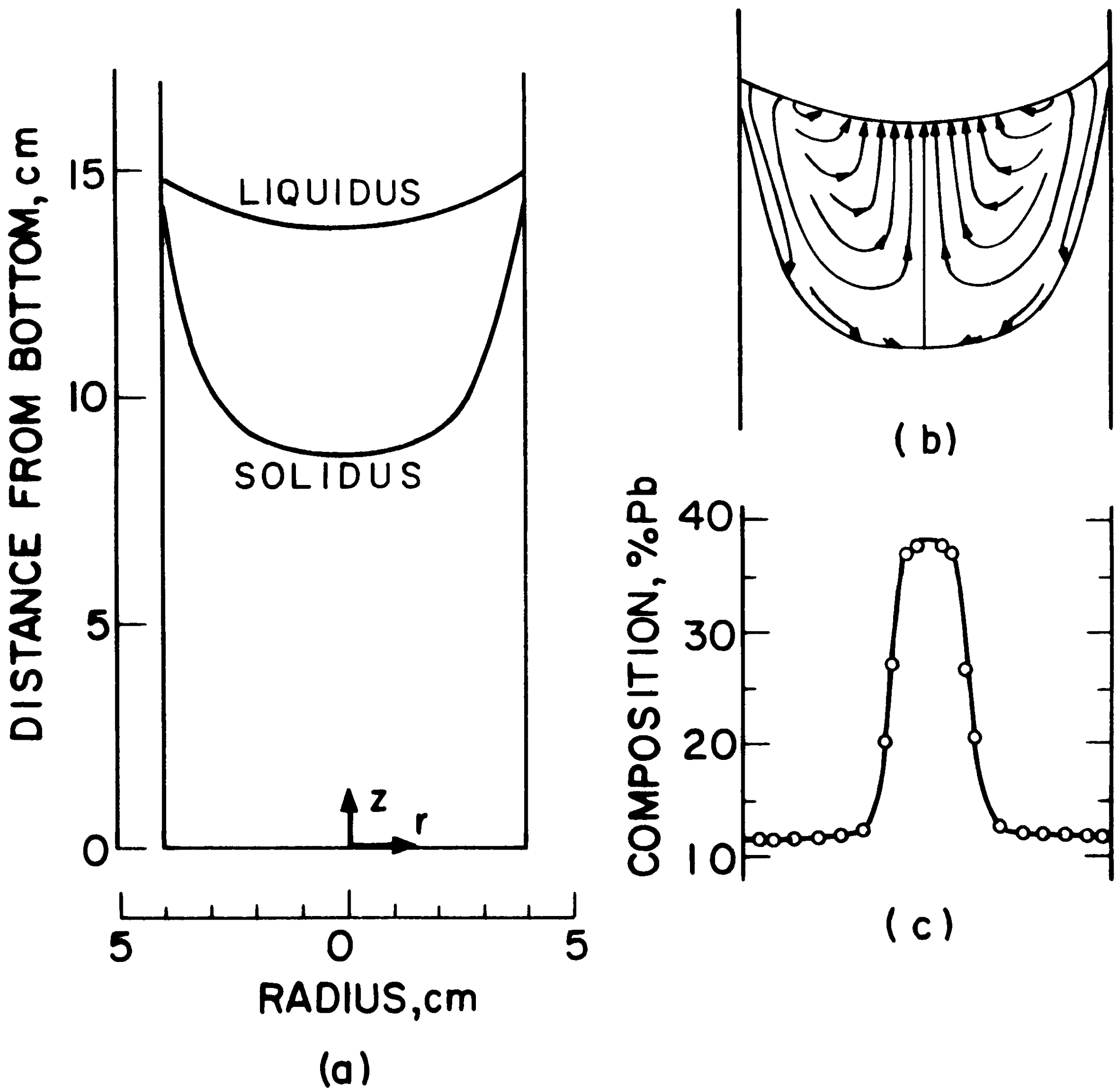

Figure 29: Results obtained for Ingot 6 (Sn-15% Pb).
(a) Liquidus and solidus isotherms after 21 minutes;
(b) flow lines of interdendritic liquid calculated with $\gamma_o = 8 \times 10^{-7}$ cm^2;
(c) macrosegregation as measured.

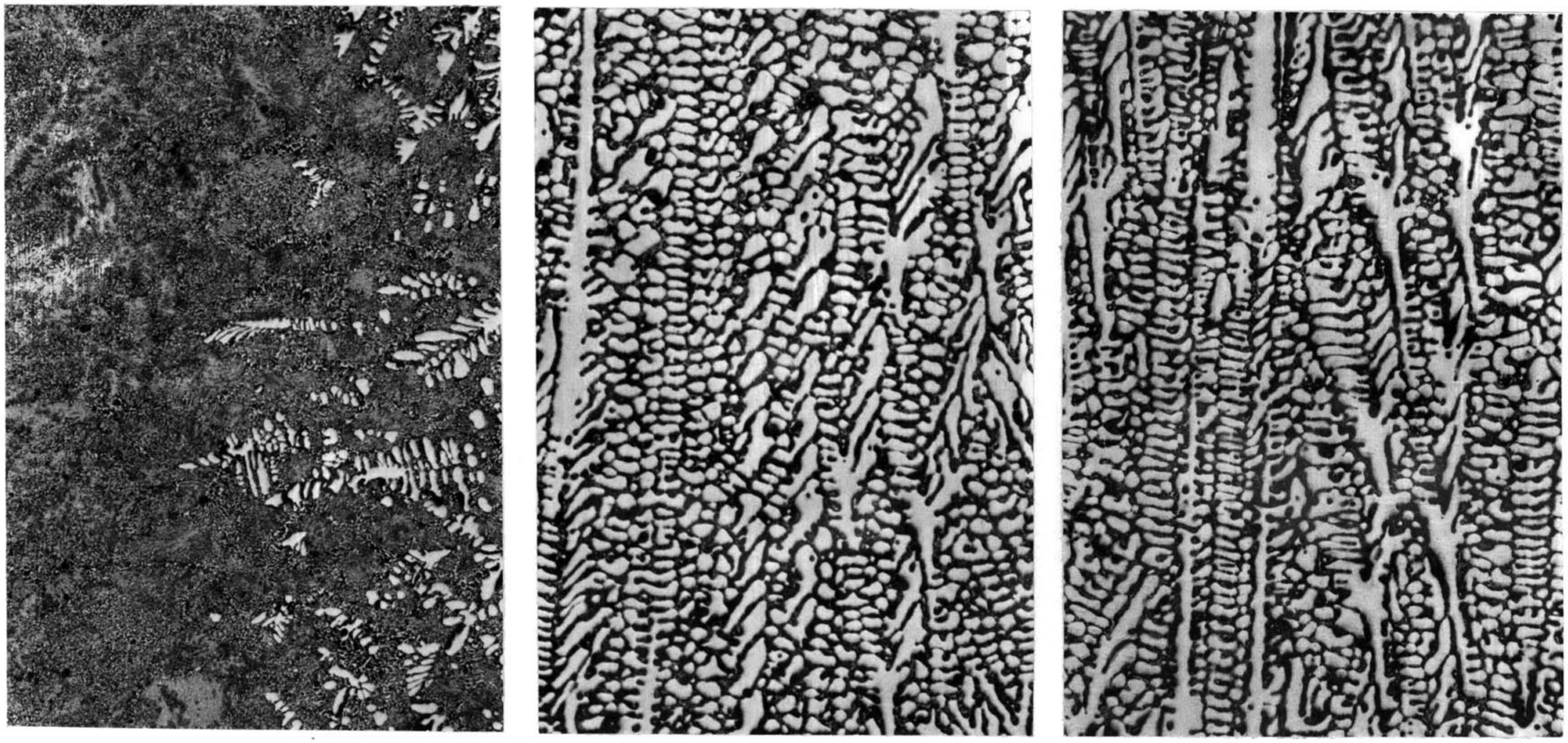

a b c

Figure 30: Longitudinal microsections of Ingot 6 (Sn-15% Pb). (a) center; (b) mid-radius; (c) near surface. Mag. 25.6X.

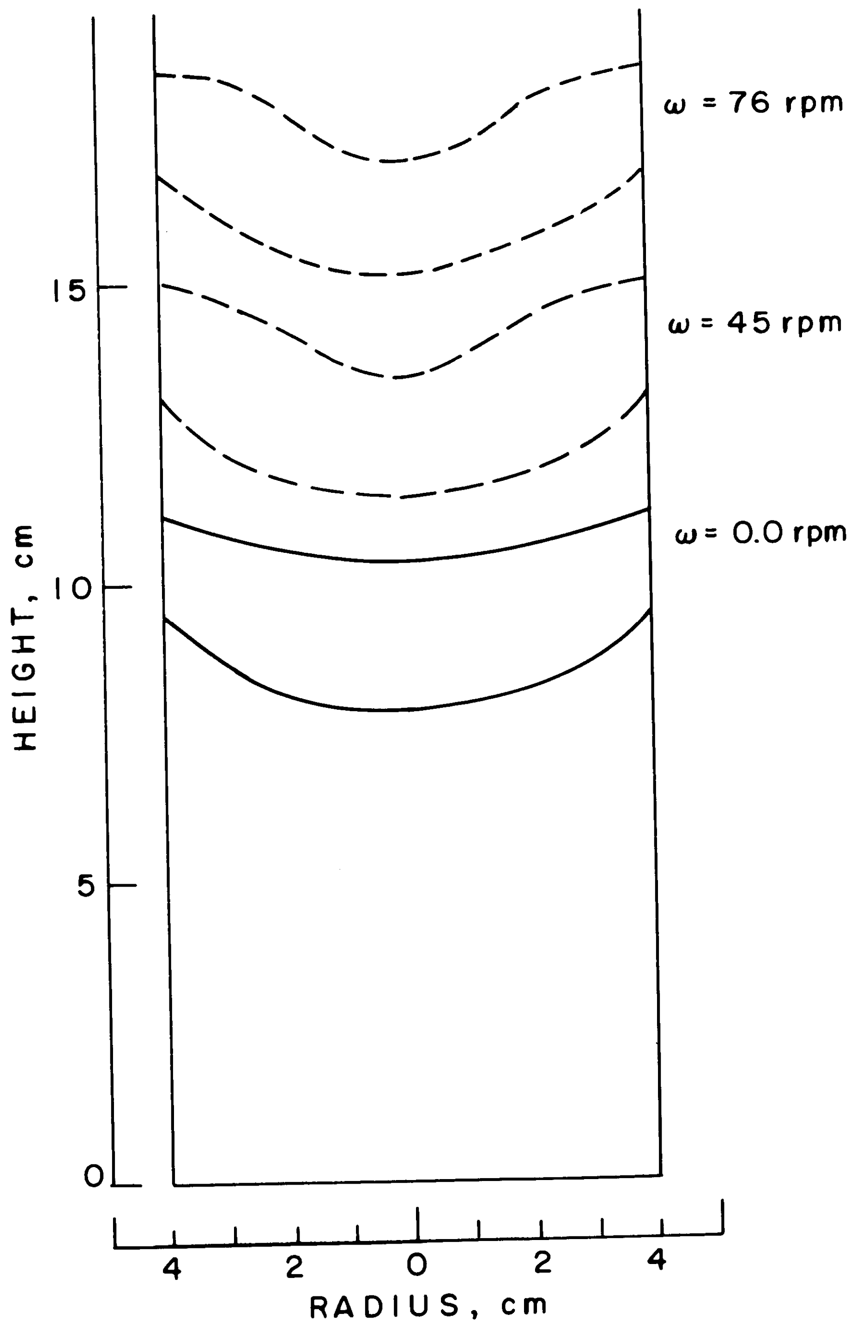

Figure 31: The shapes of the mushy zone in Ingot 7 (Sn-12% Pb).

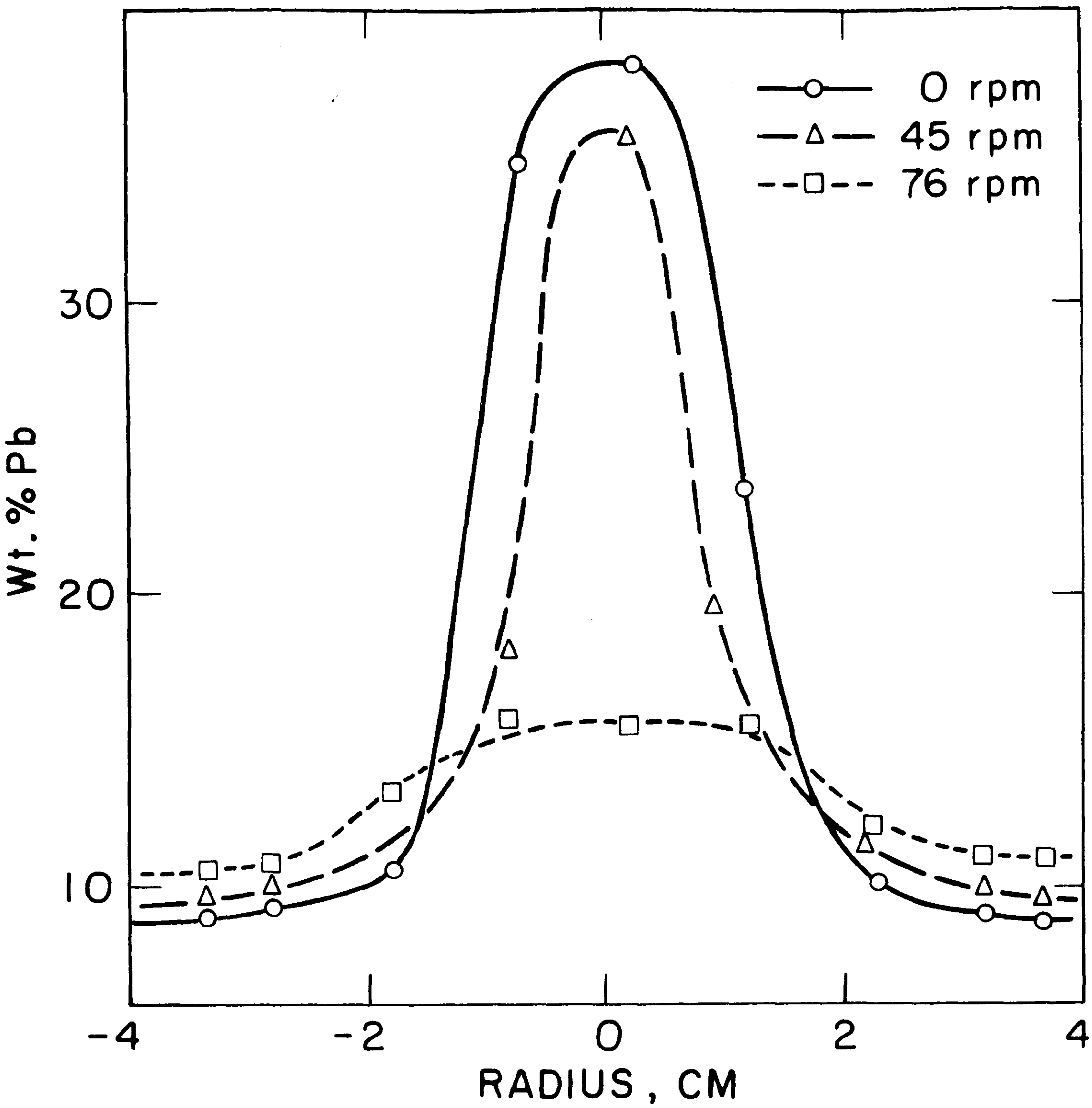

Figure 32: Macrosegregation in Ingot 7 (Sn-12% Pb).

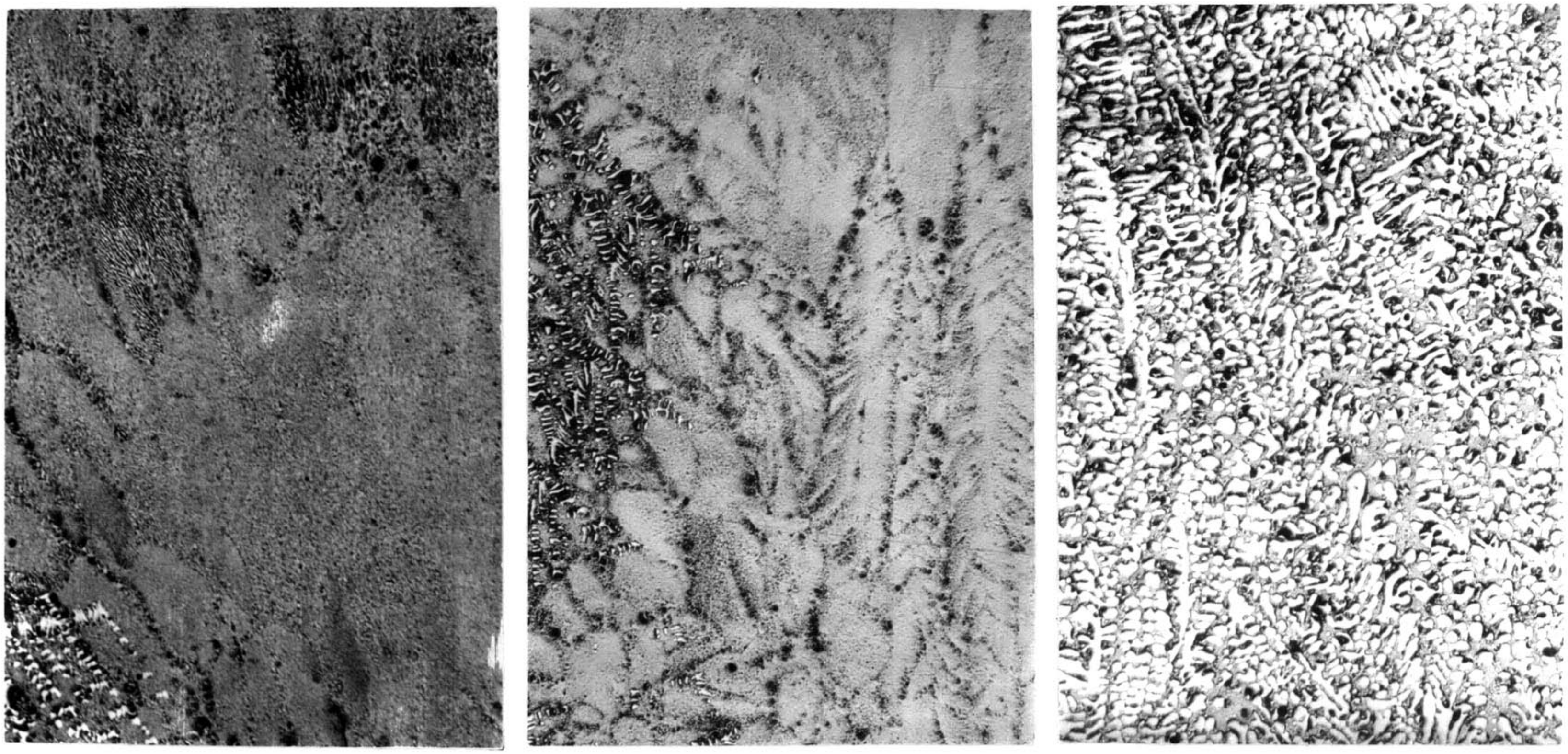

a b c

Figure 33: Longitudinal microsections at the center of Ingot 7 (Sn-12%Pb)
(a) 0 rpm; (b) 45 rpm; (c) 76 rpm. Mag. 25.6X.

Table 3. Results of Sn-Pb Ingots with Rotation

Ingot #	8	9	10	11	12
Solid'n Rate	5.6×10^{-3} cm/sec	6.6×10^{-3} cm/sec	5.3×10^{-3} cm/sec	8.3×10^{-3} cm/sec	1.36×10^{-2} cm/sec
Rotation Speed	83 rpm	97 rpm	119 rpm	66 rpm	54 rpm
Shape of Mushy Zone	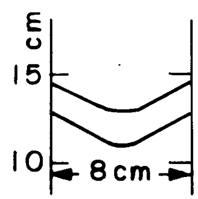	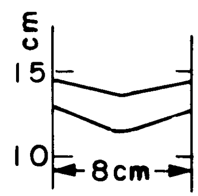	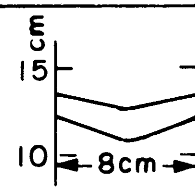	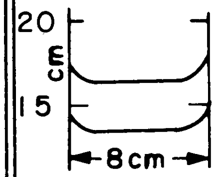	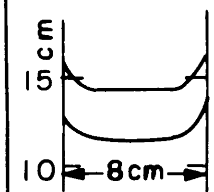
Macrosegre-gation	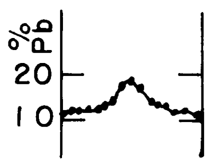	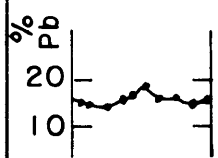	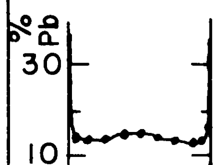	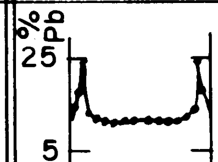	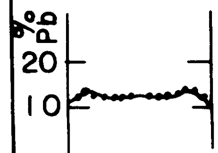
Freckle (Transverse Cross Section)	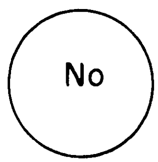	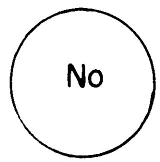	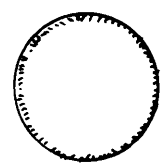	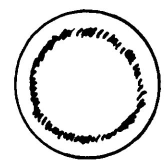	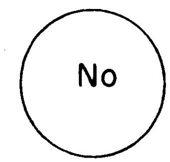
Comment	Increasing $\left(\frac{\text{Spinning Effect}}{\text{Gravity Effect}}\right)$ → Decreasing $\left(\frac{C_{center} - C_{edge}}{C_{origional}}\right)$			Abrupt change in Isotherm Slopes Near Edge	Fast Solid'n Rate and Little Segre-gation

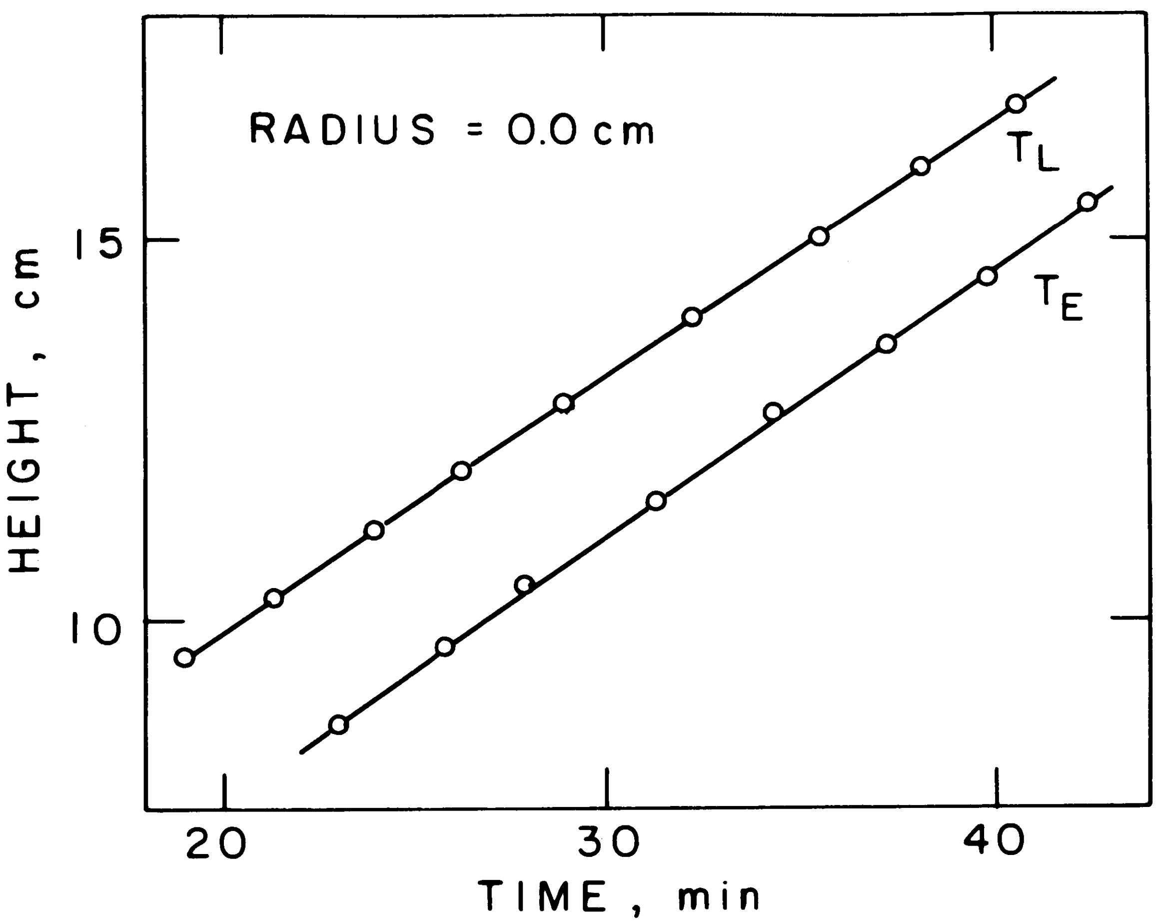

Figure 34: Position of the liquidus and solidus isotherms along the centerline of Ingot 8.

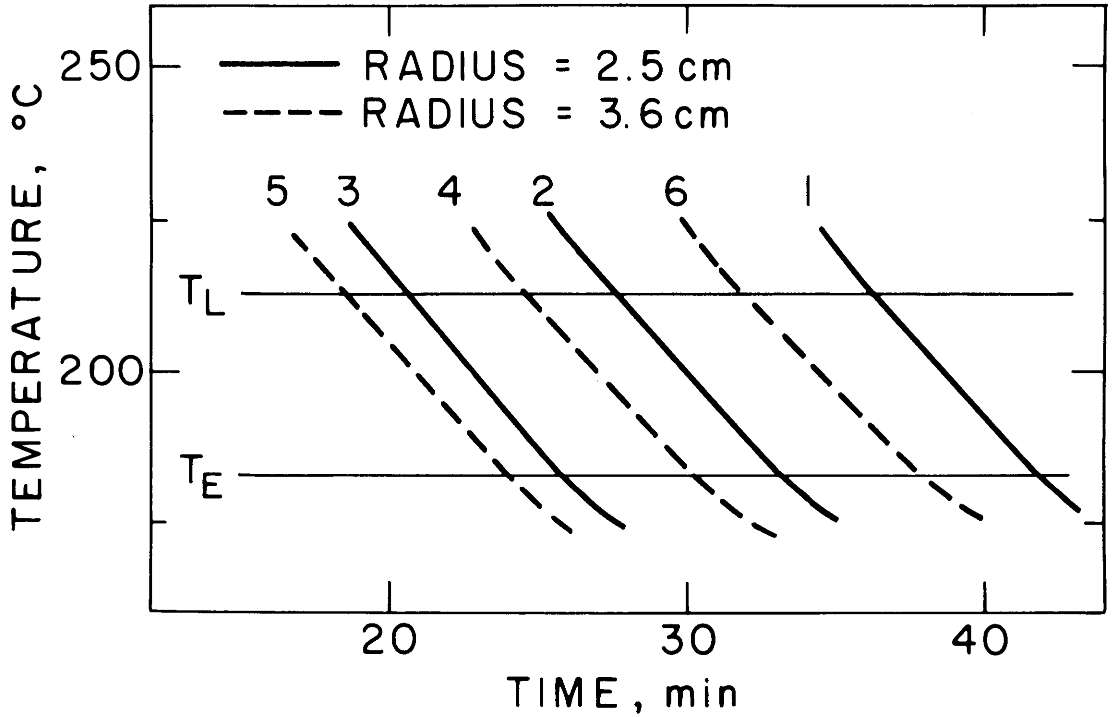

Figure 35: Cooling curves for Ingot 8.

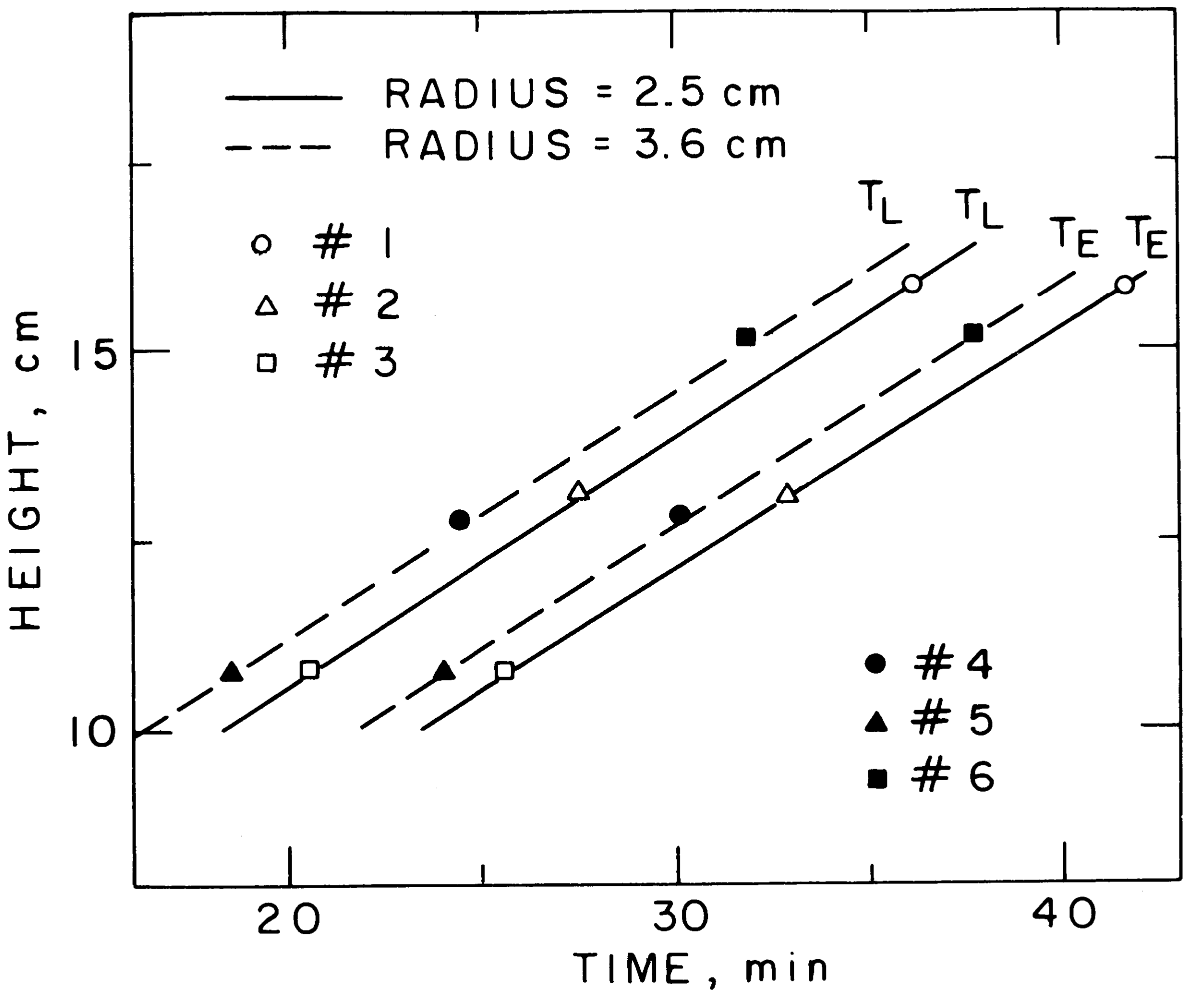

Figure 36: Position of the liquidus and solidus isotherms in Ingot 8.

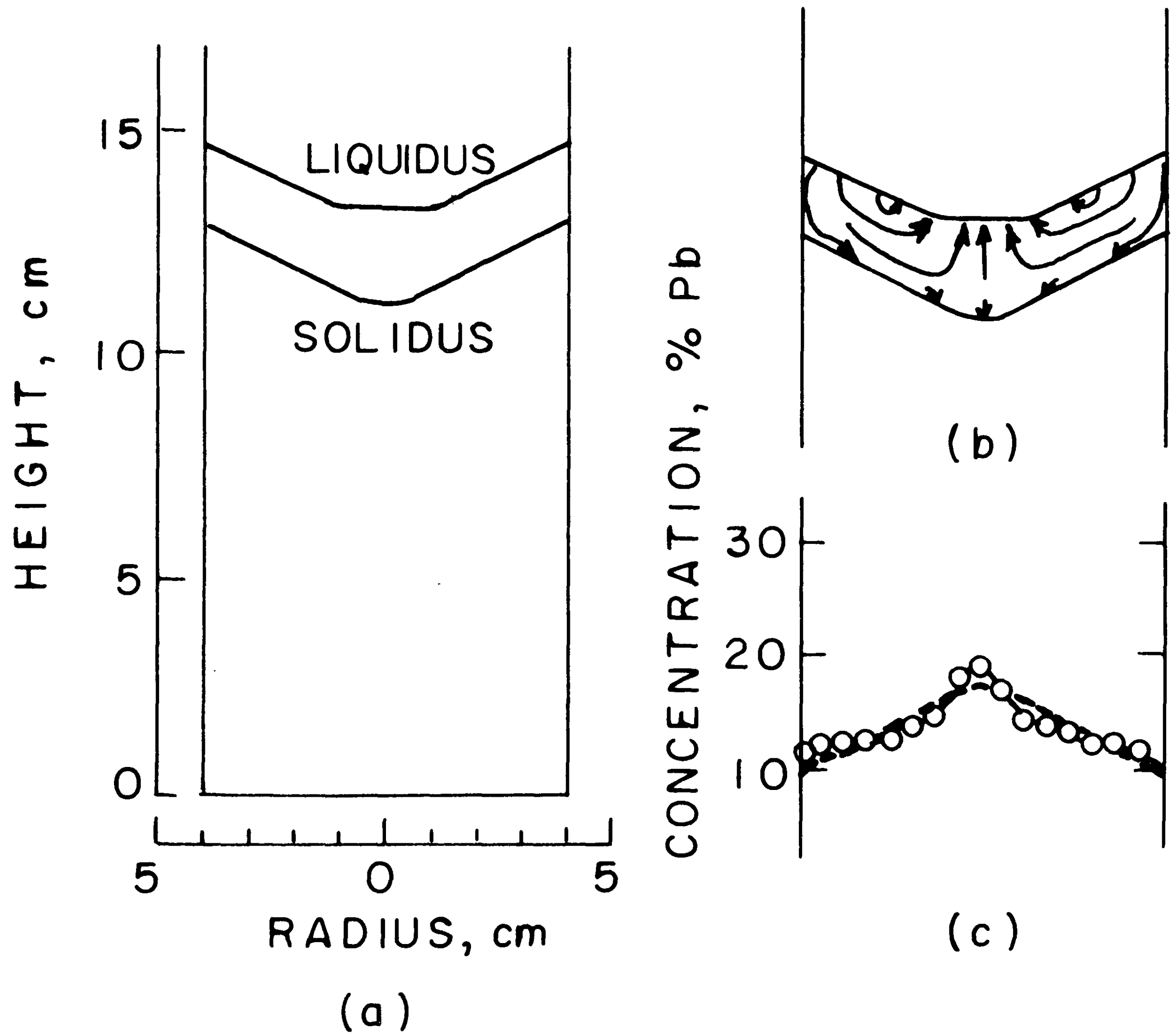

Figure 37: Results obtained for Ingot 8 (Sn-12.2% Pb).
(a) Liquidus and solidus isotherms after 30 minutes;
(b) flow lines of interdendritic liquid;
(c) macrosegregation as measured (solid curve) and calculated with $\gamma_o = 1.2 \times 10^{-6}$ cm^2 (broken curve).

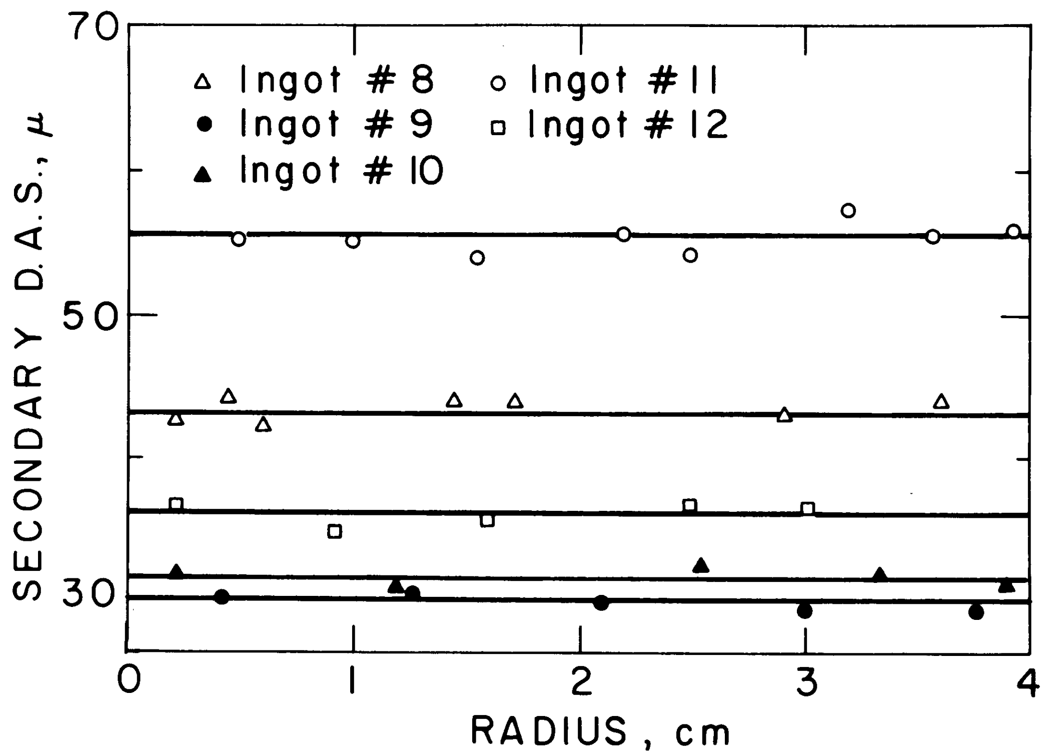

Figure 38: Secondary dendrite arm spacings in Ingots 8-12.

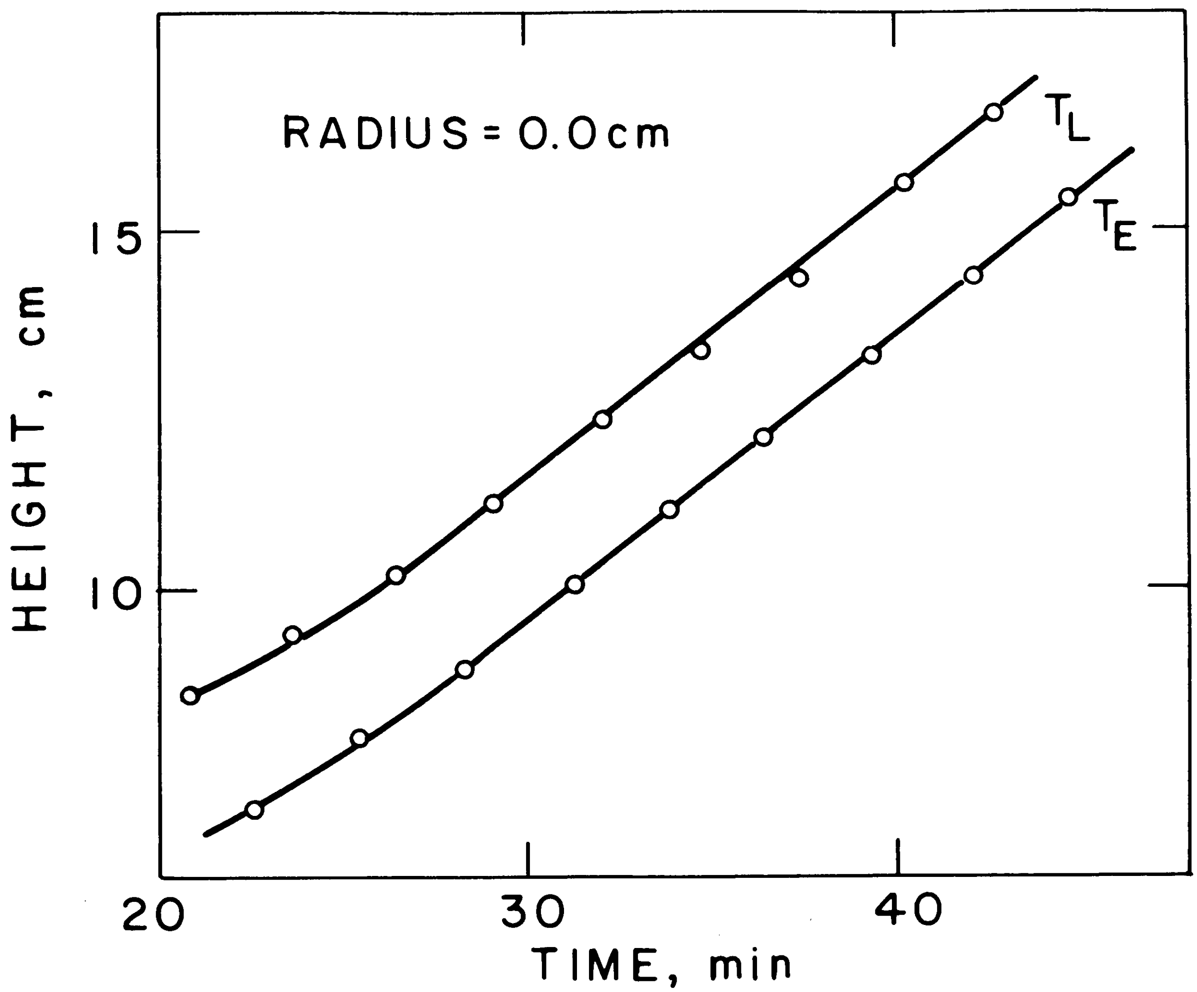

Figure 39: Position of the liquidus and solidus isotherms along the centerline of Ingot 9.

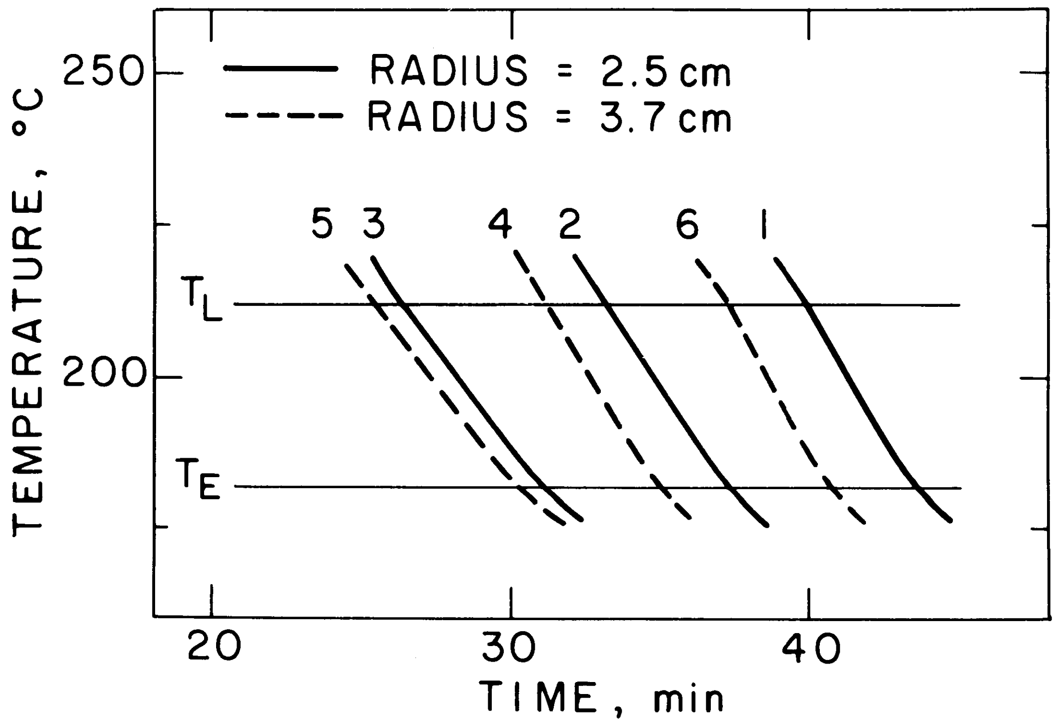

Figure 40: Cooling curves for Ingot 9.

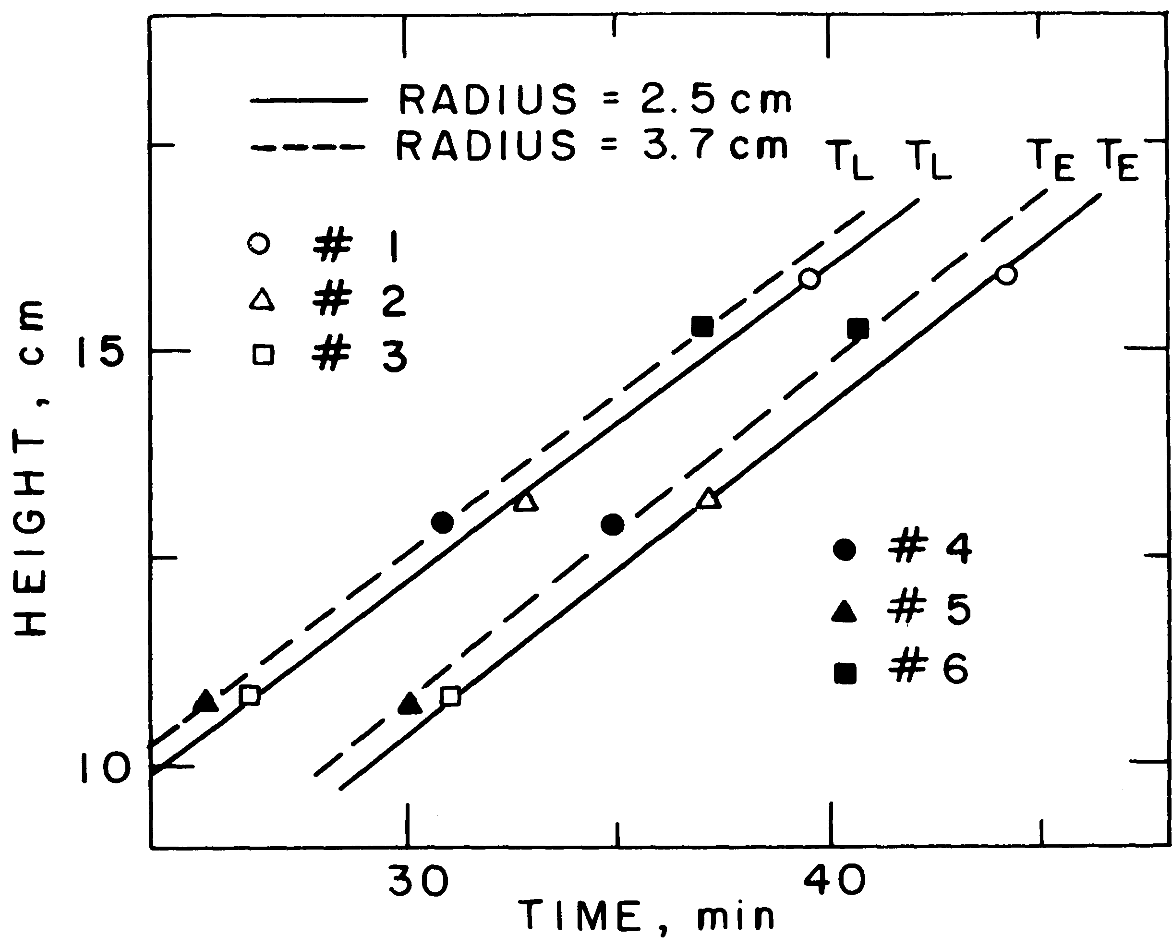

Figure 41: Position of the liquidus and solidus isotherms in Ingot 9.

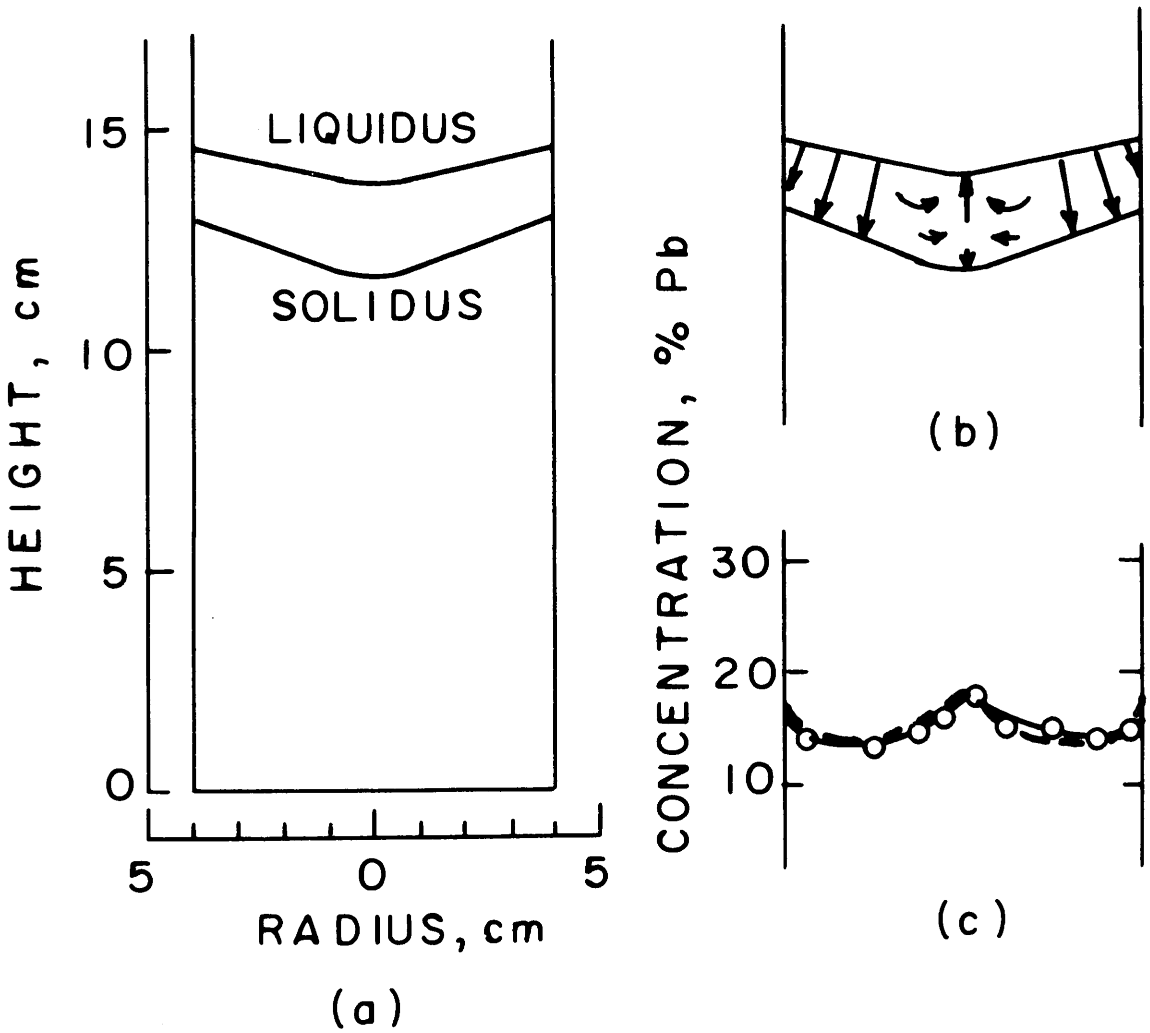

Figure 42: Results obtained for Ingot 9 (Sn-14.0% Pb).
(a) Liquidus and solidus isotherms after 28 minutes;
(b) flow lines of interdendritic liquid;
(c) macrosegregation as measured (solid curve) and calculated with $\gamma_o = 0.98 \times 10^{-6}$ cm^2 (broken curve)

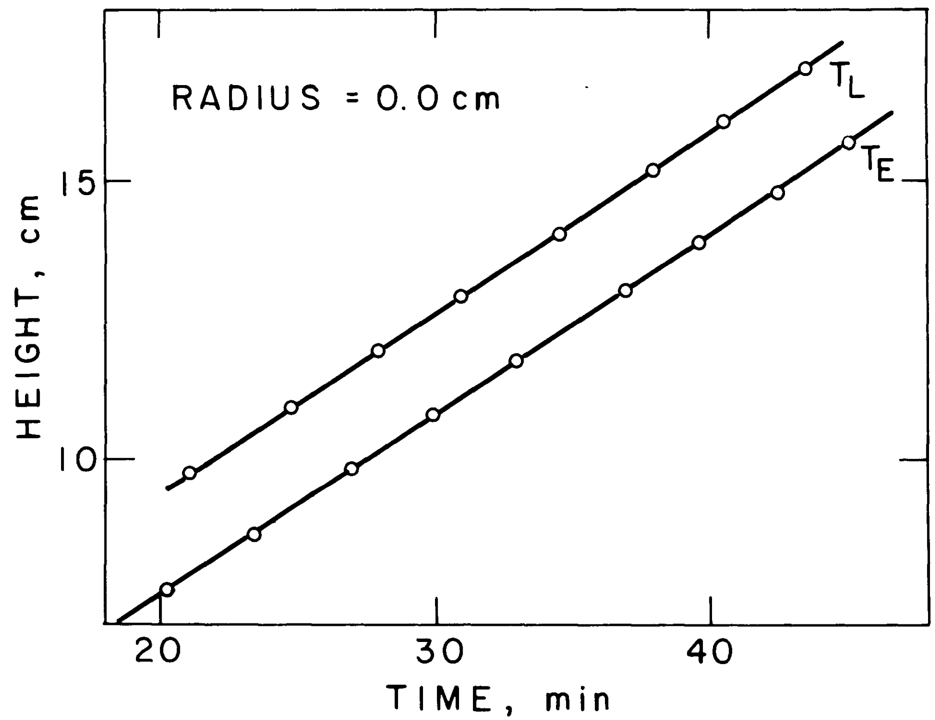

Figure 43: Position of the liquidus and solidus isotherms along the centerline of Ingot 10.

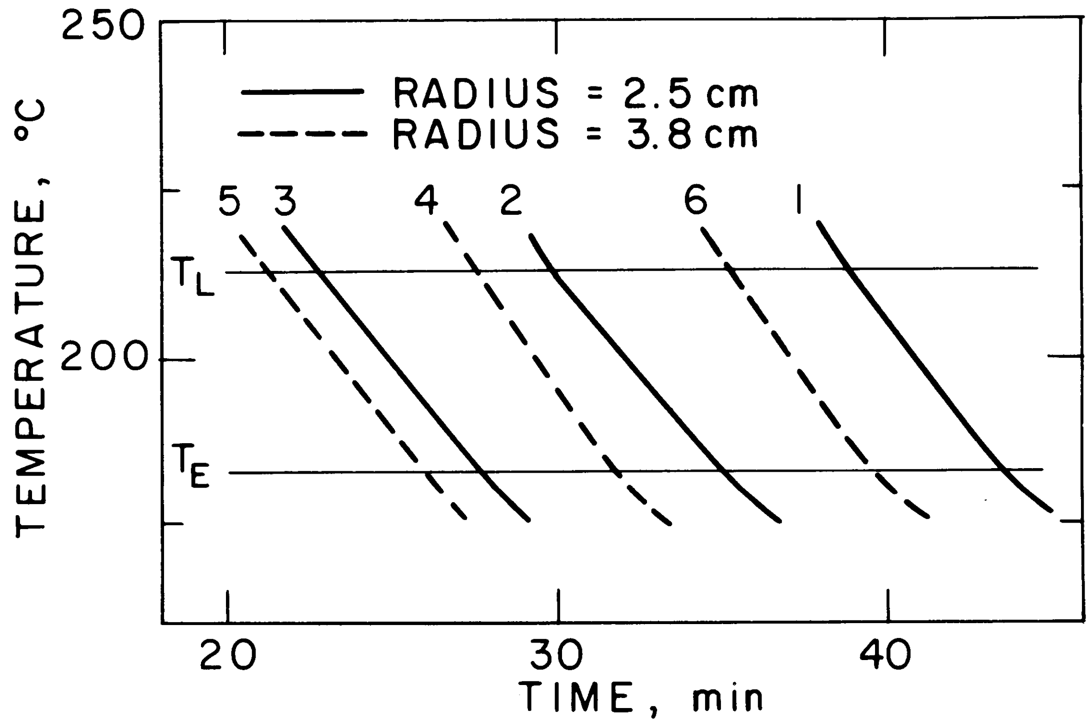

Figure 44: Cooling curves for Ingot 10.

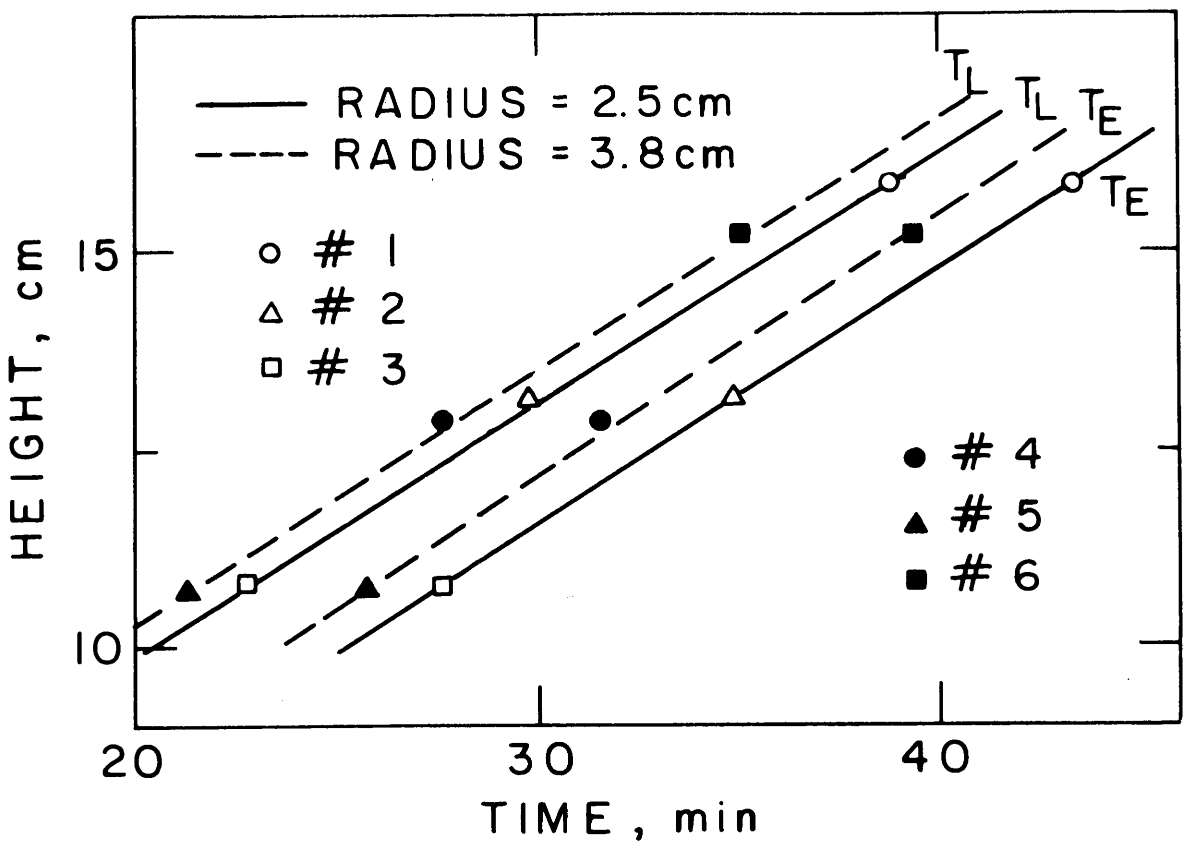

Figure 45: Position of the liquidus and solidus in Ingot 10.

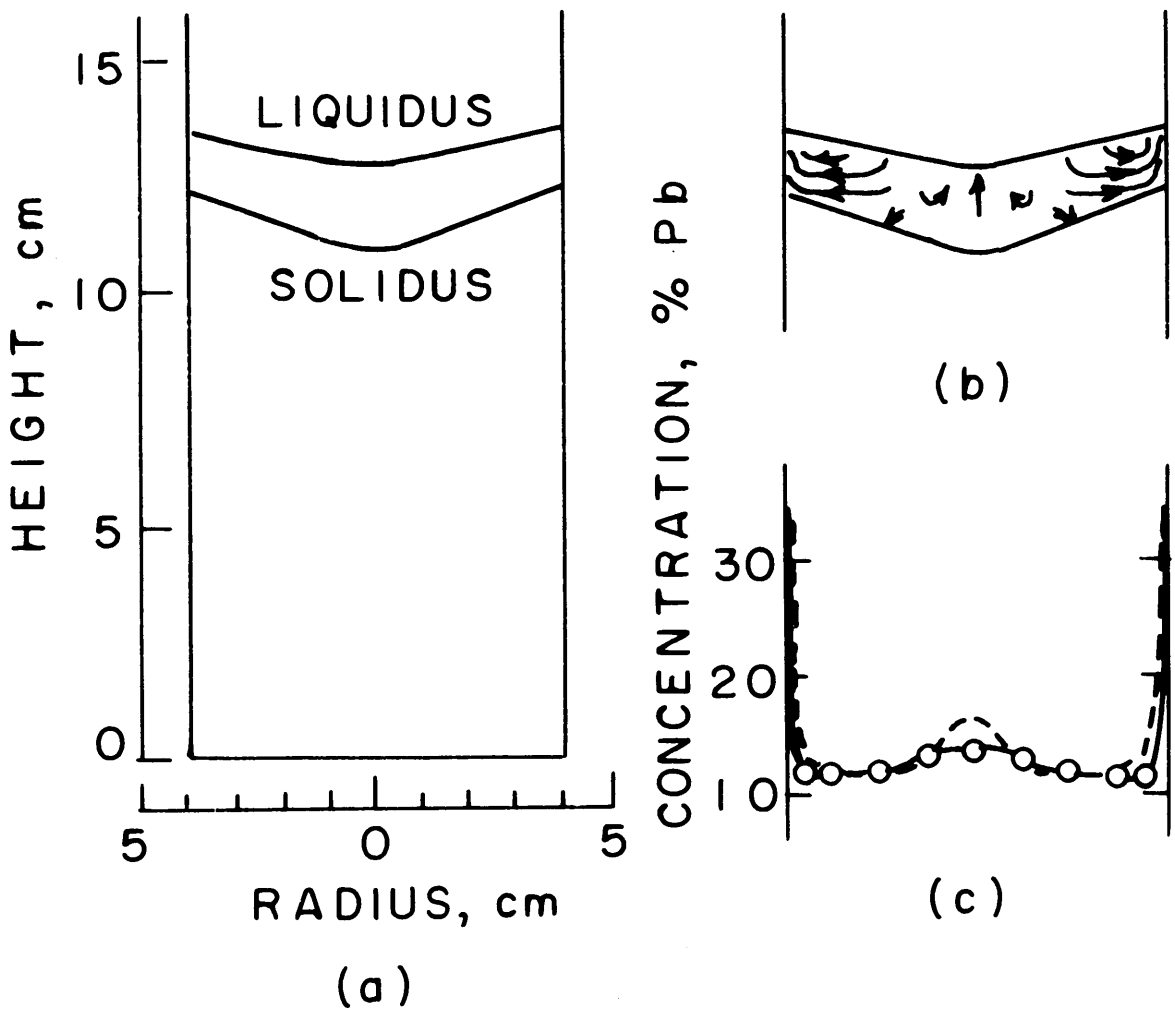

Figure 46: Results obtained for Ingot 10 (Sn-12.8% Pb).
(a) Liquidus and solidus isotherms after 30 minutes;
(b) flow lines of interdendritic liquid;
(c) macrosegregation as measured (solid curve) and calculated with $\gamma_o = 1.3 \times 10^{-6}$ cm^2 (broken curve)

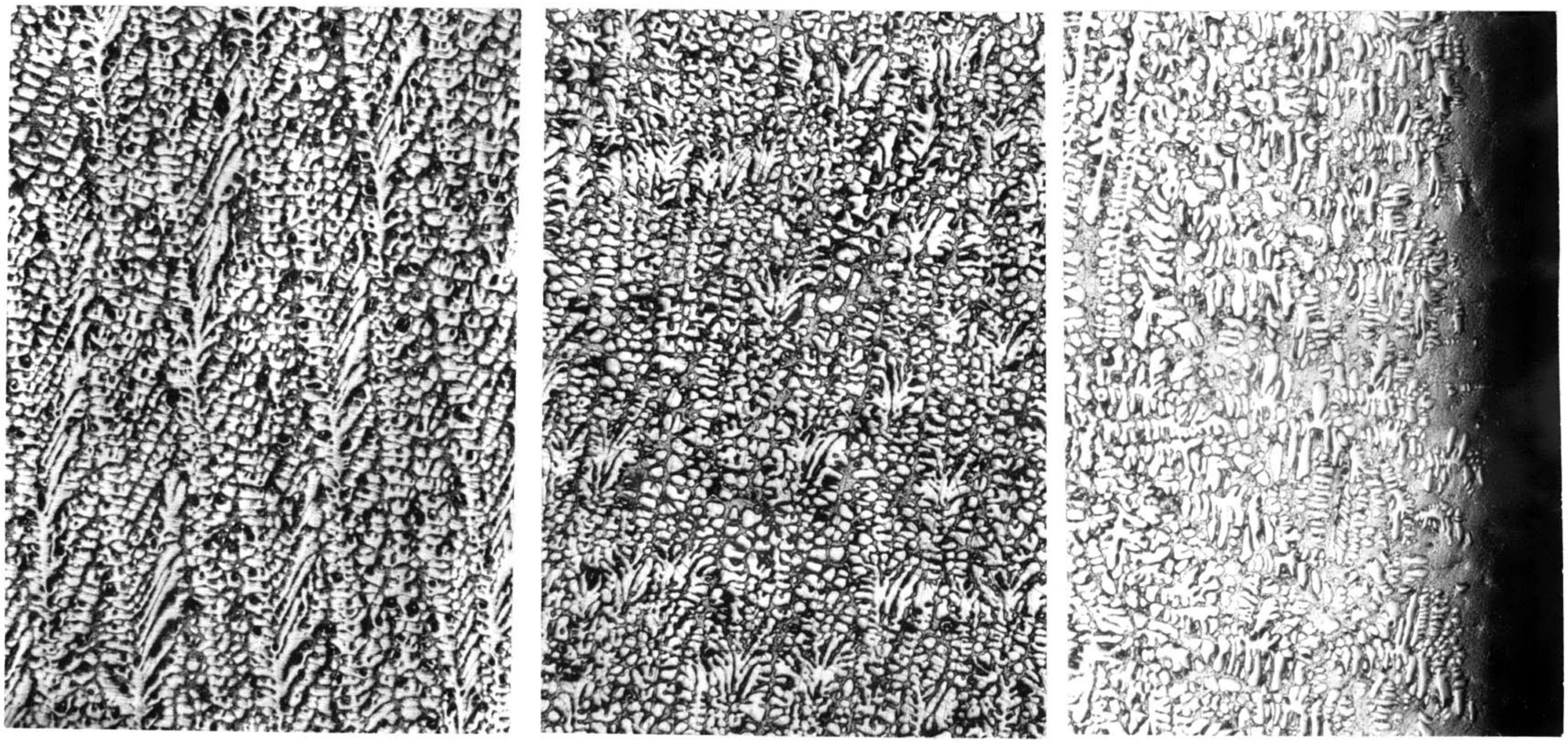

a b c

Figure 47: Longitudinal microsections of Ingot 10 (Sn-12.8% Pb).
(a) center; (b) mid-radius; (c) near surface. Mag. 25.6X.

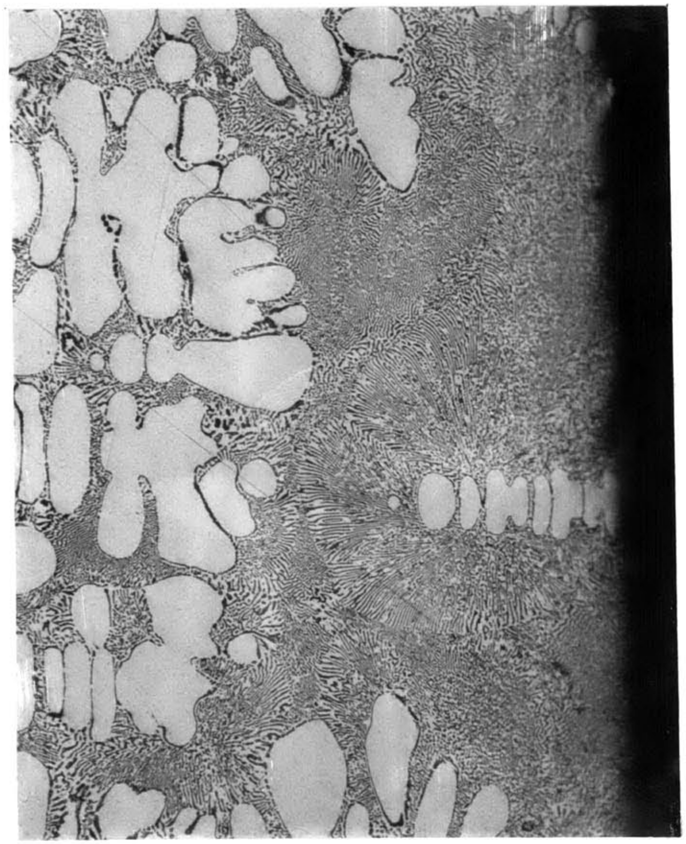

Figure 48: Longitudinal microsection at the edge of Ingot 10 (Sn-12.8% Pb). Mag. 128X.

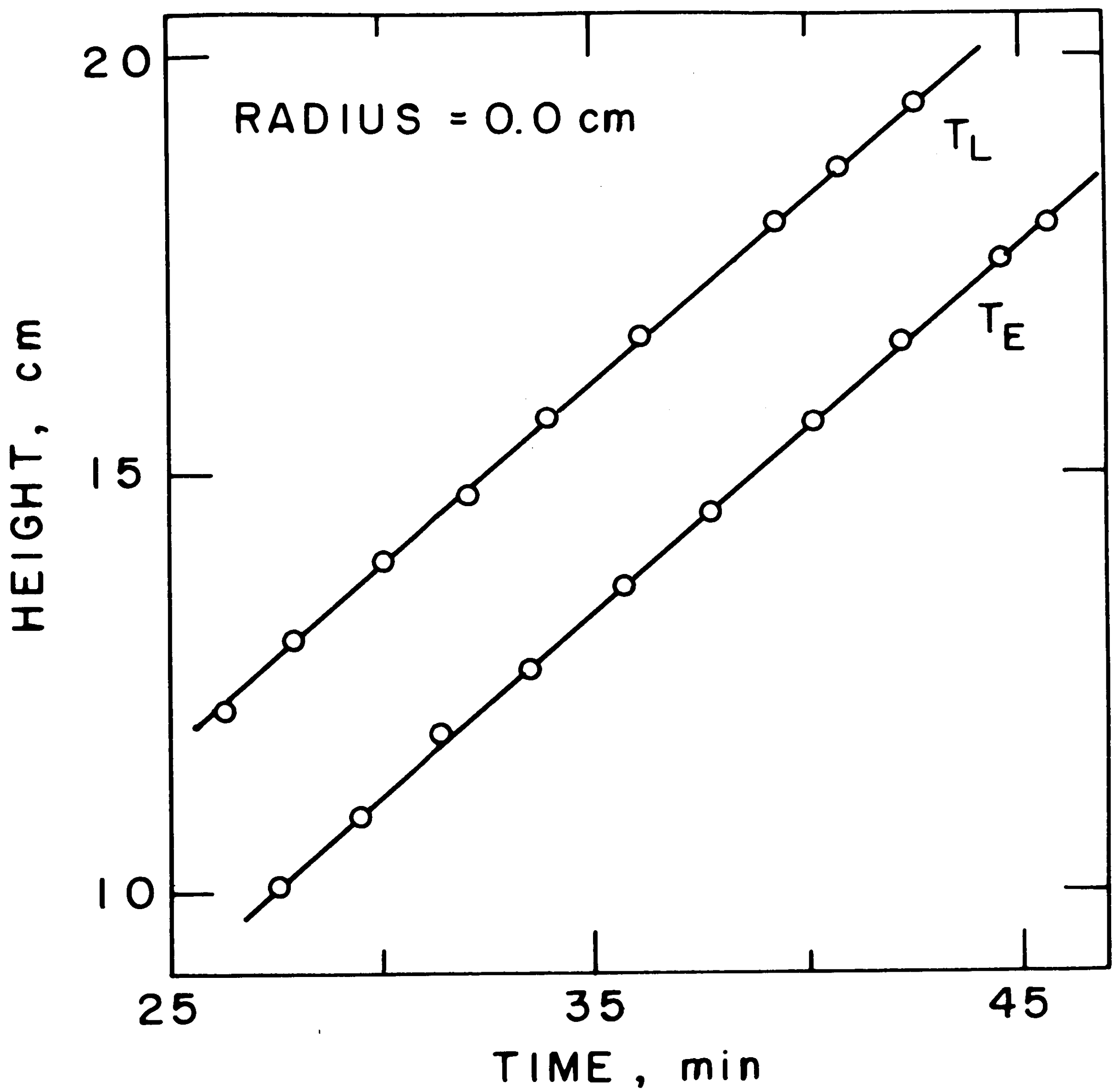

Figure 49: Position of the liquidus and solidus along the centerline of Ingot 11.

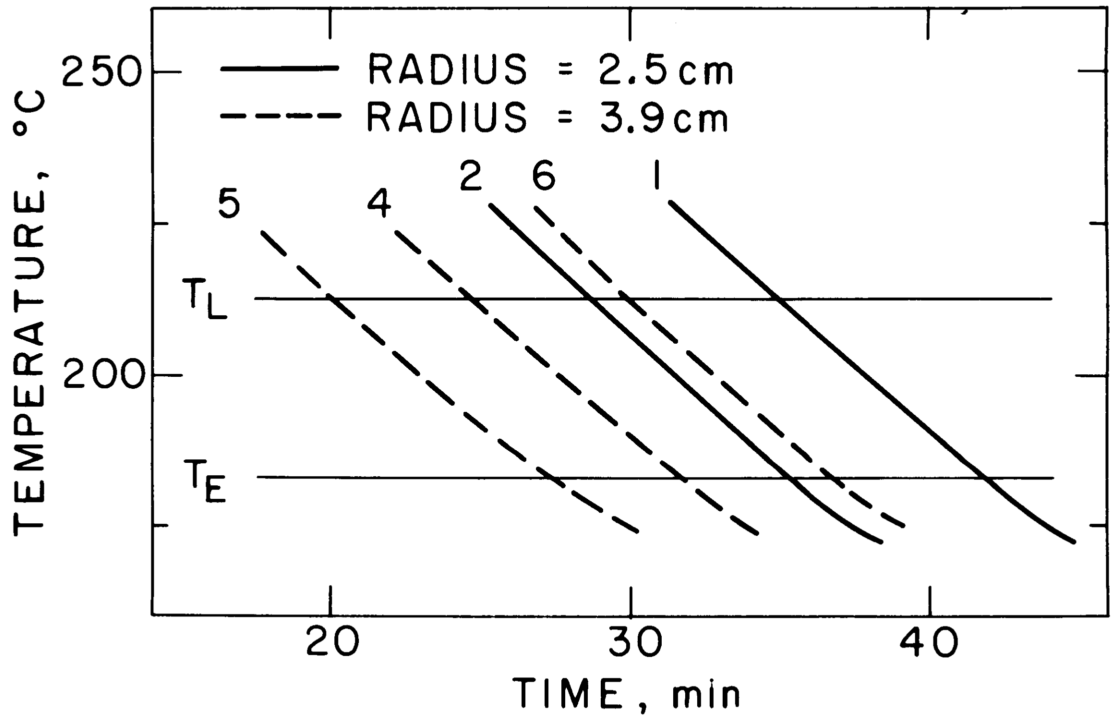

Figure 50: Cooling curves for Ingot 11.

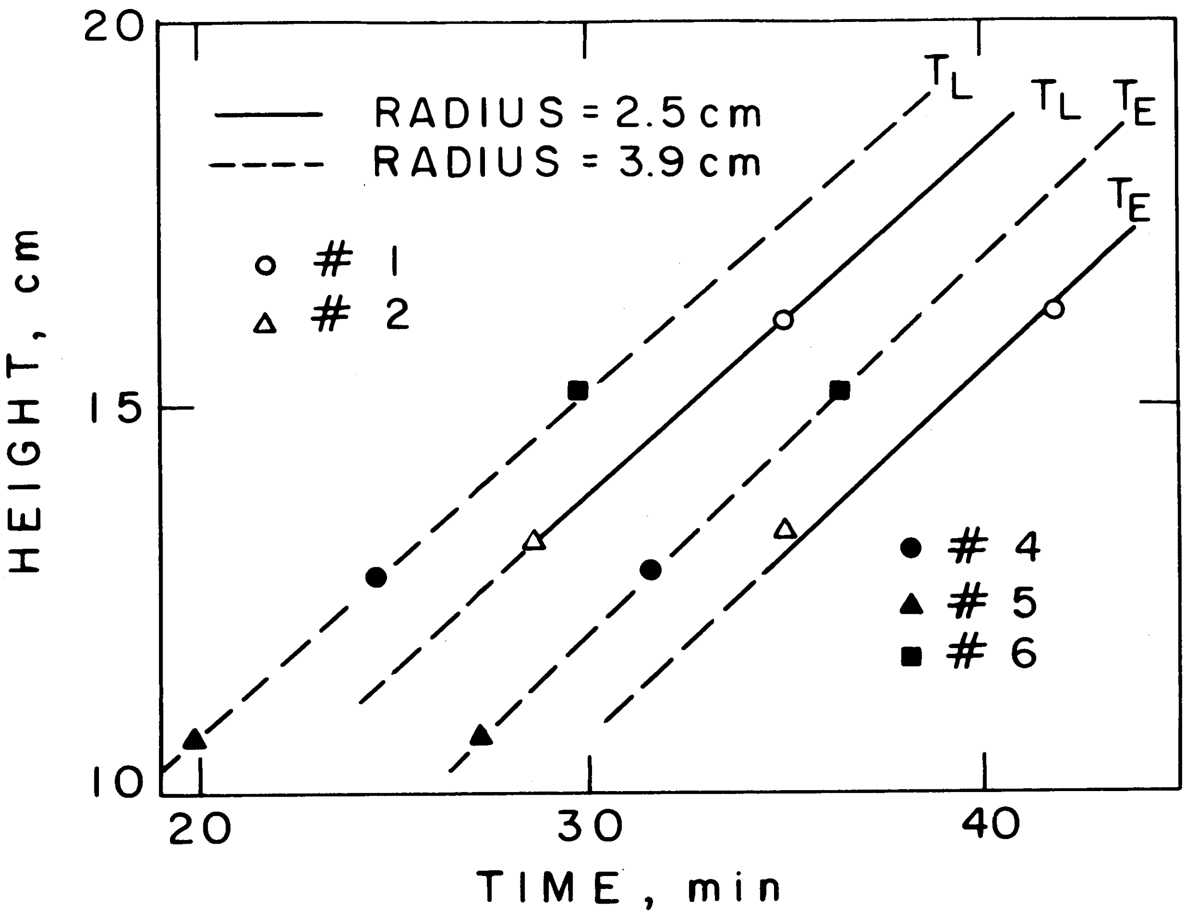

Figure 51: Position of the liquidus and solidus isotherms in Ingot 11.

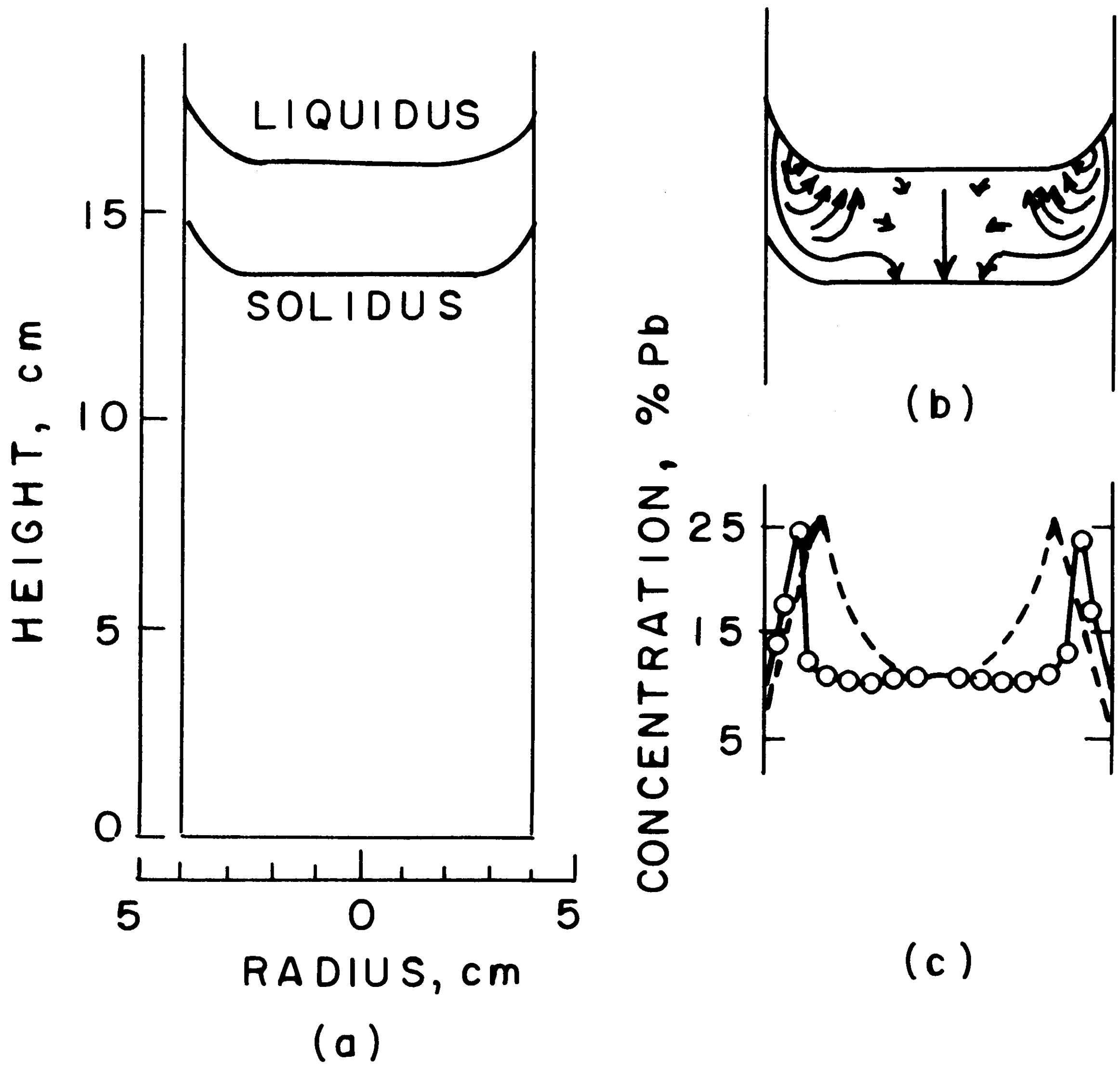

Figure 52: Results obtained for Ingot 11 (Sn-12.4% Pb).
(a) Liquidus and solidus isotherms after 35 minutes;
(b) flow lines of interdendritic liquid;
(c) macrosegregation as measured (solid curve) and calculated with $\gamma_o = 3.3 \times 10^{-6}$ cm^2 (broken curve)

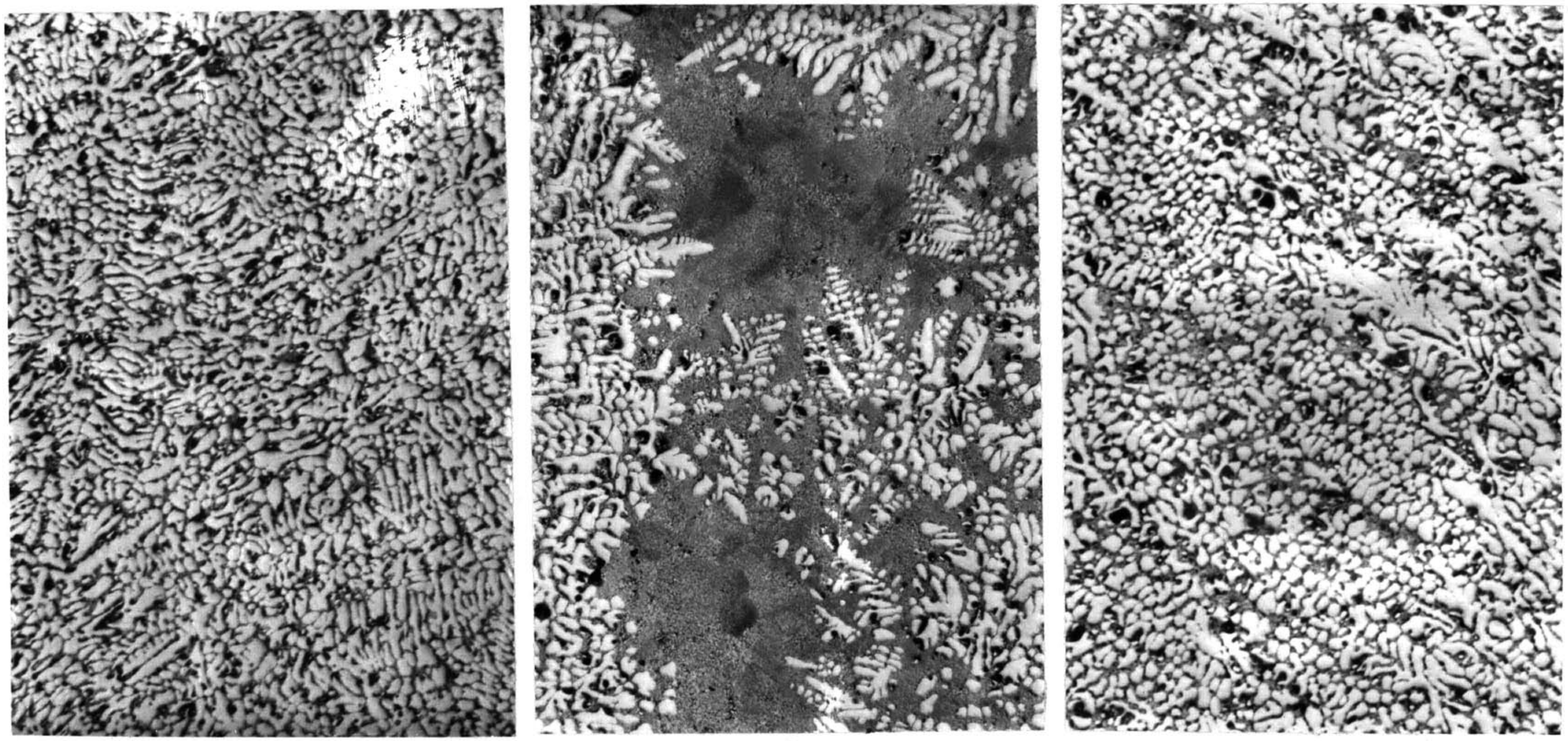

a b c

Figure 53: Transverse microsections of Ingot 11 (Sn-12.4% Pb). (a) center; (b) mid-radius; (c) near surface. Mag. 25.6X.

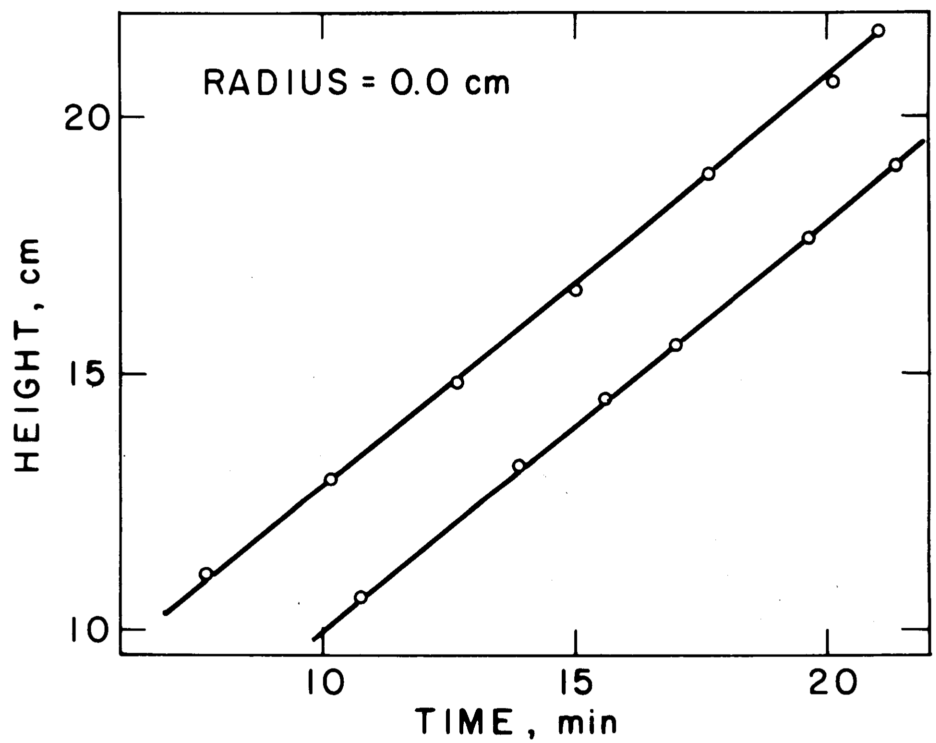

Figure 54: Position of the liquidus and solidus isotherms along the centerline of Ingot 12.

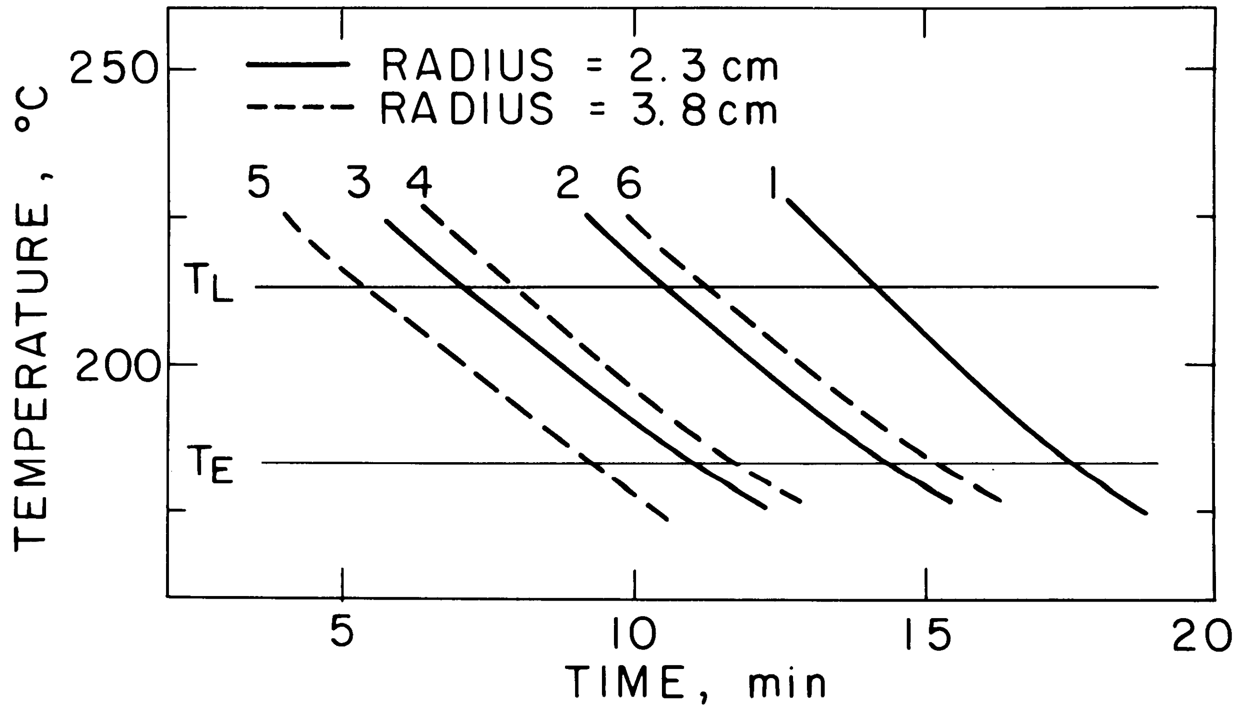

Figure 55: Cooling curves for Ingot 12.

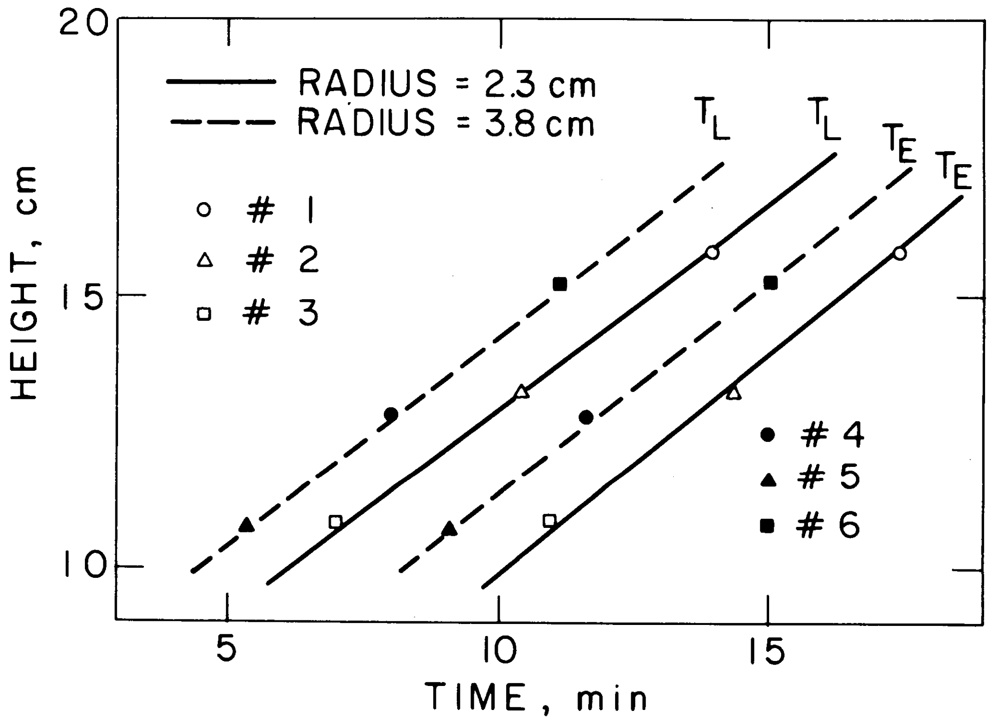

Figure 56: Position of the liquidus and solidus in Ingot 12.

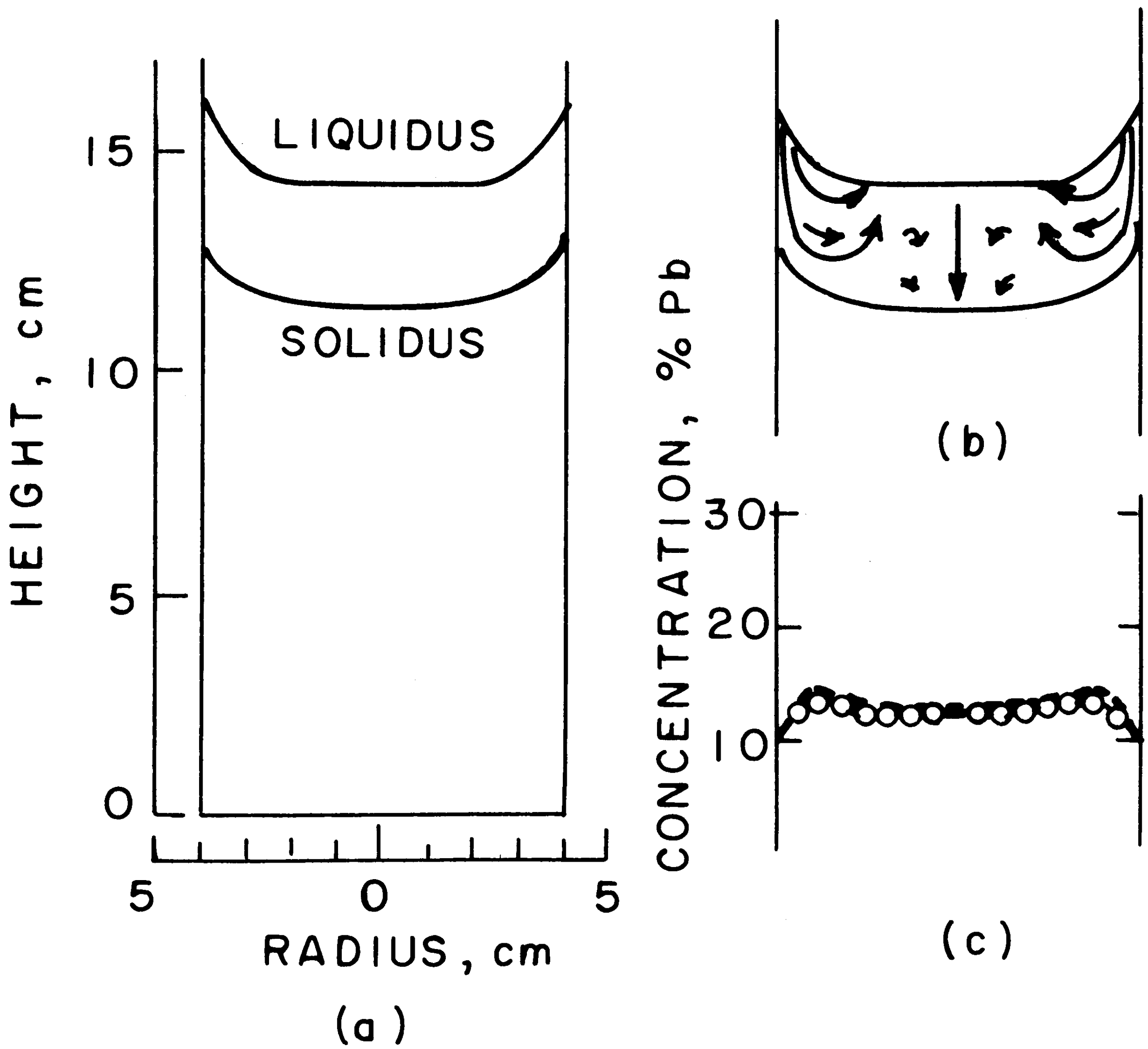

Figure 57: Results obtained for Ingot 12 (Sn-12.0% Pb).
(a) Liquidus and solidus isotherms after 12 minutes;
(b) flow lines of interdendritic liquid;
(c) macrosegregation as measured (solid curve) and calculated with $\gamma_o = 1.0 \times 10^{-6}$ cm^2 (broken curve)

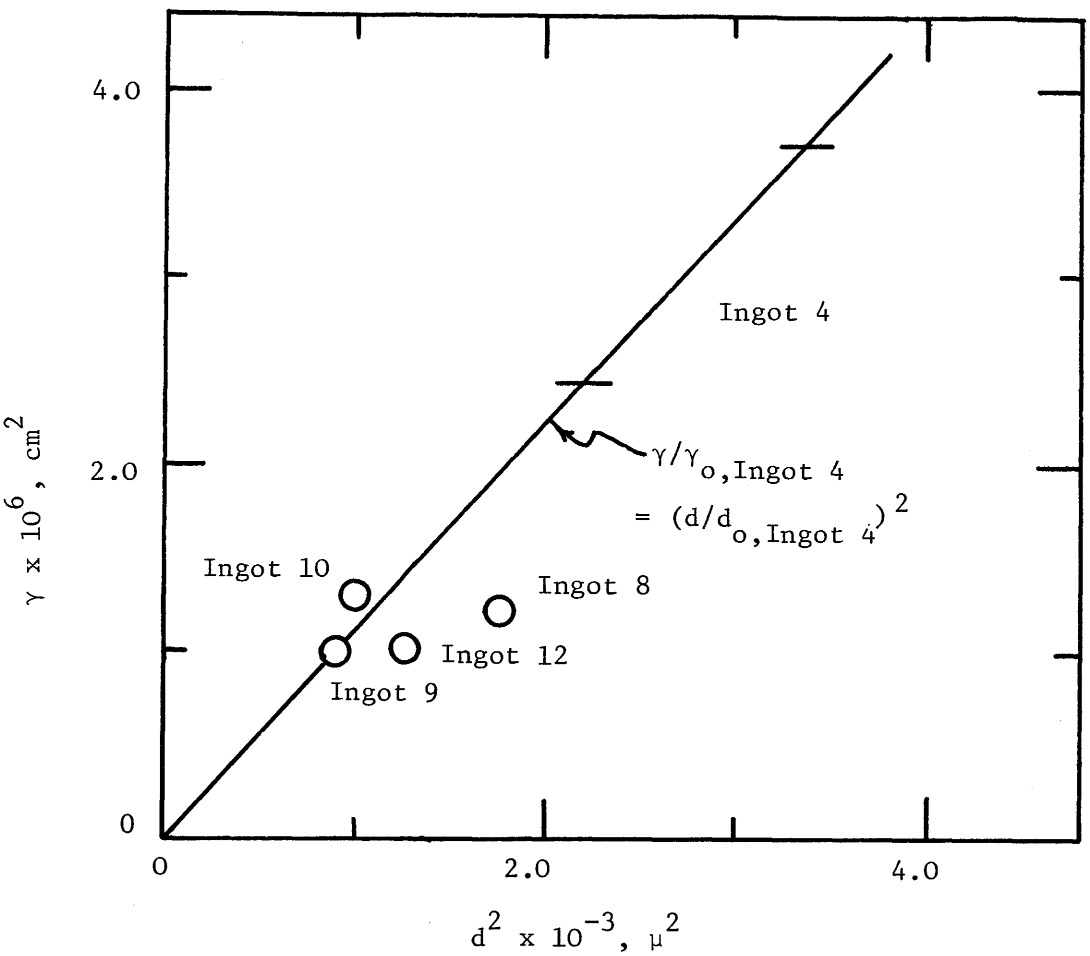

Figure 58: Permeabilities used in Calculation

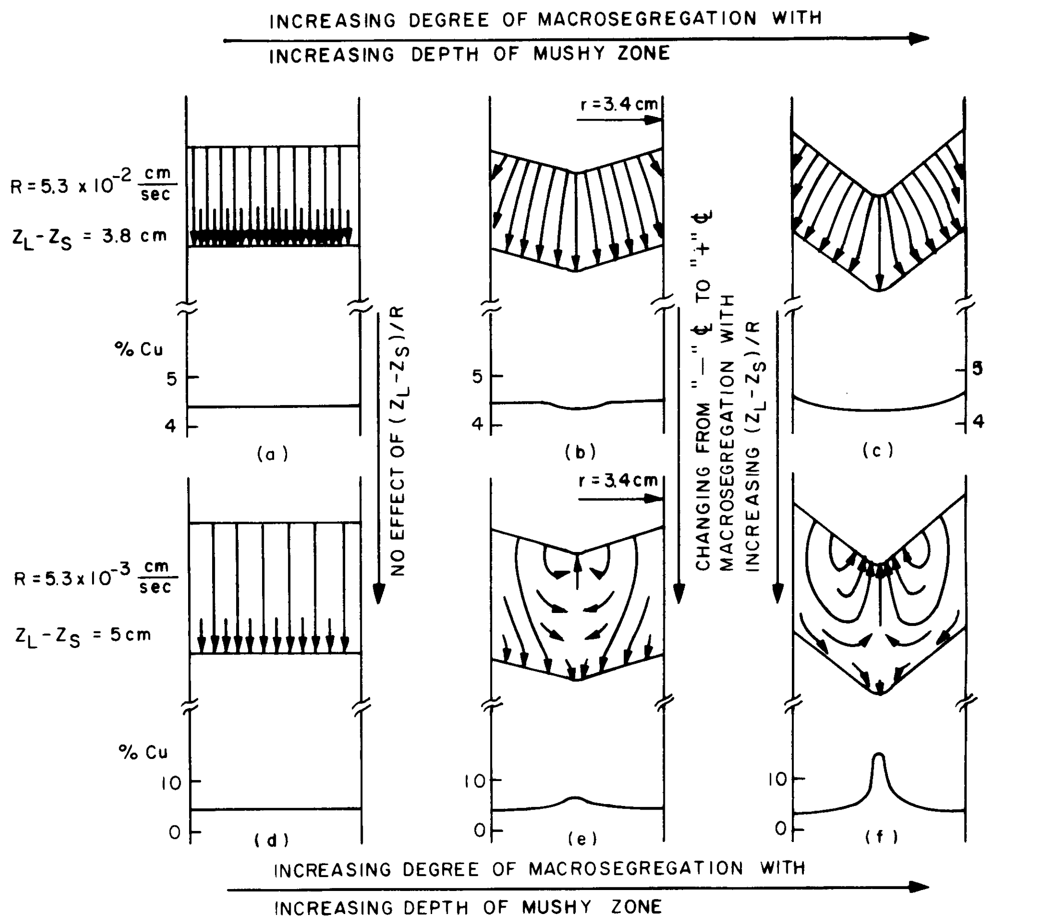

Figure 59: Effects of mushy zone shape and solidification rate on macrosegregation in Al-4.4%Cu. $\gamma_o = 5 \times 10^{-7}$ cm^2

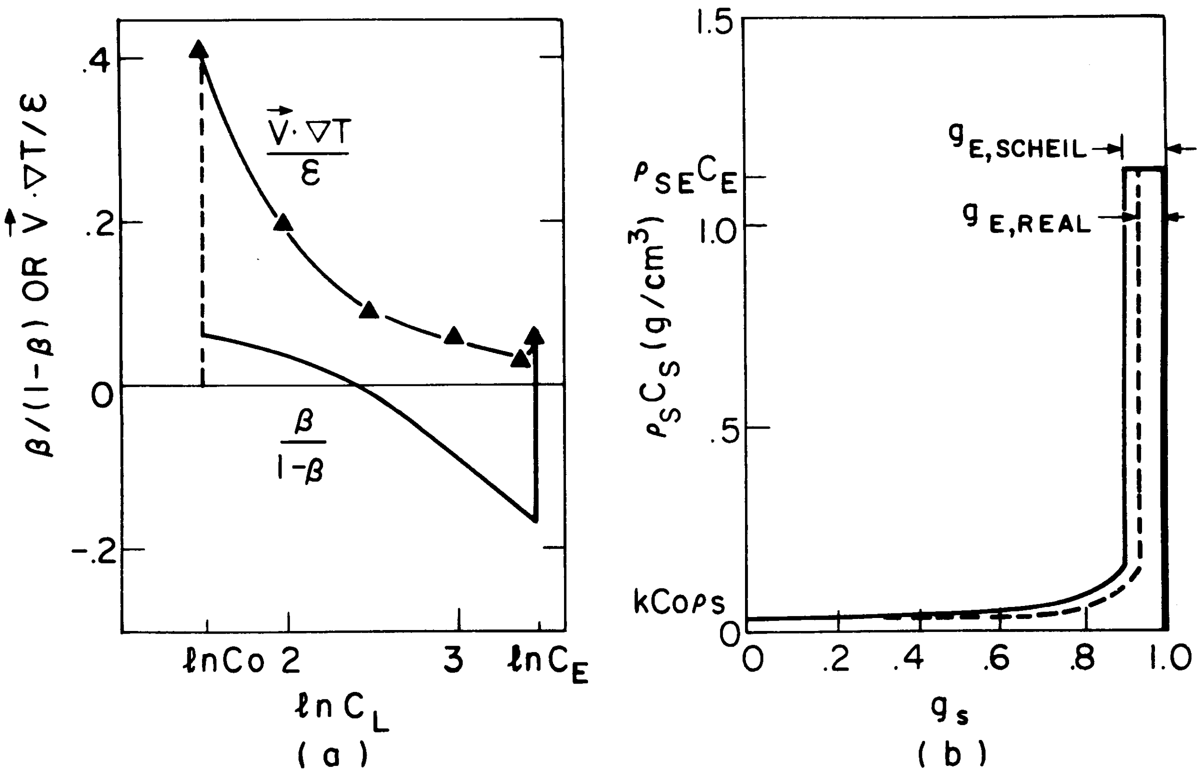

Figure 60: Parameters leading to negative segregation at the center of Ingot 1 (Al-4.4%Cu). (a) Values of the dimensionless group in the local solute redistribution equation; (b) solute accumulation with interdendritic liquid flow and neglecting flow (Scheil equation).

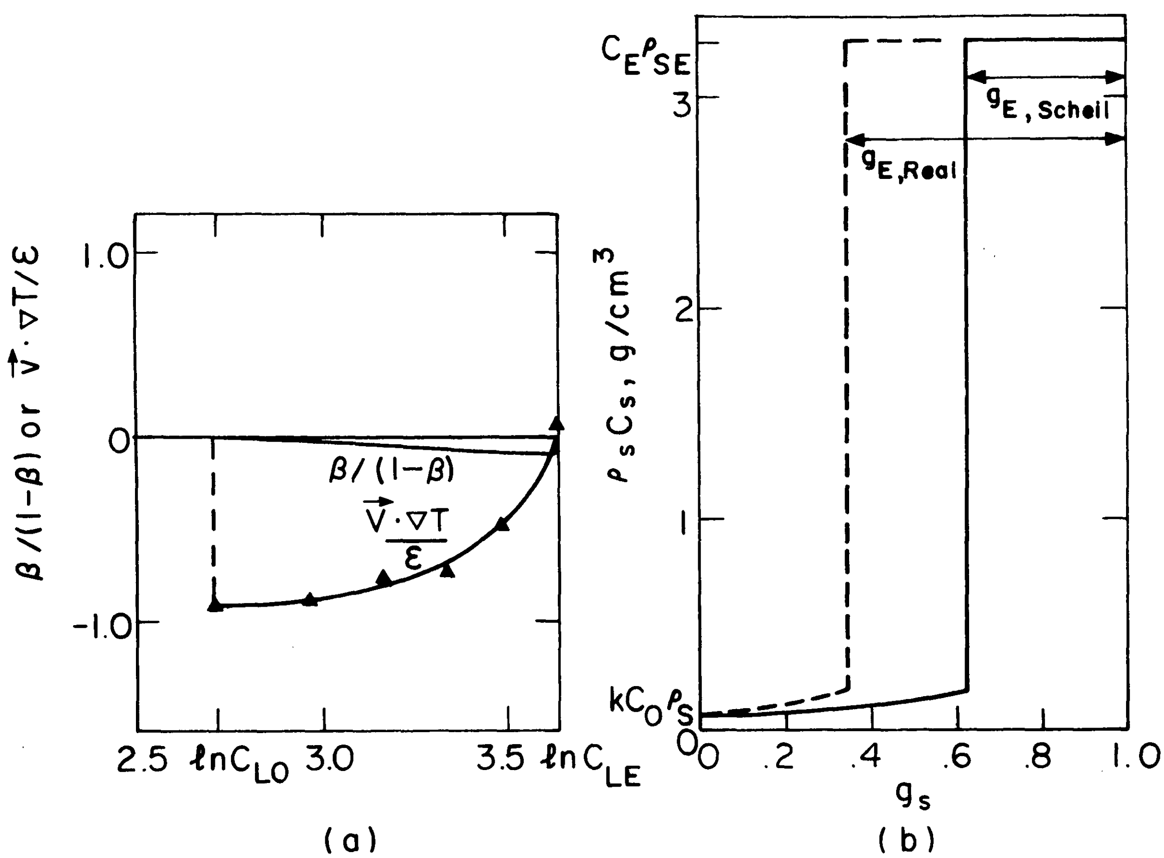

Figure 61: Parameters leading to positive segregation at the center of Ingot 4 (Sn-15% Pb). (a) Values of the dimensionless group in the local solute redistribution equation; (b) solute accumulation with interdendritic liquid flow and neglecting flow (Scheil equation).

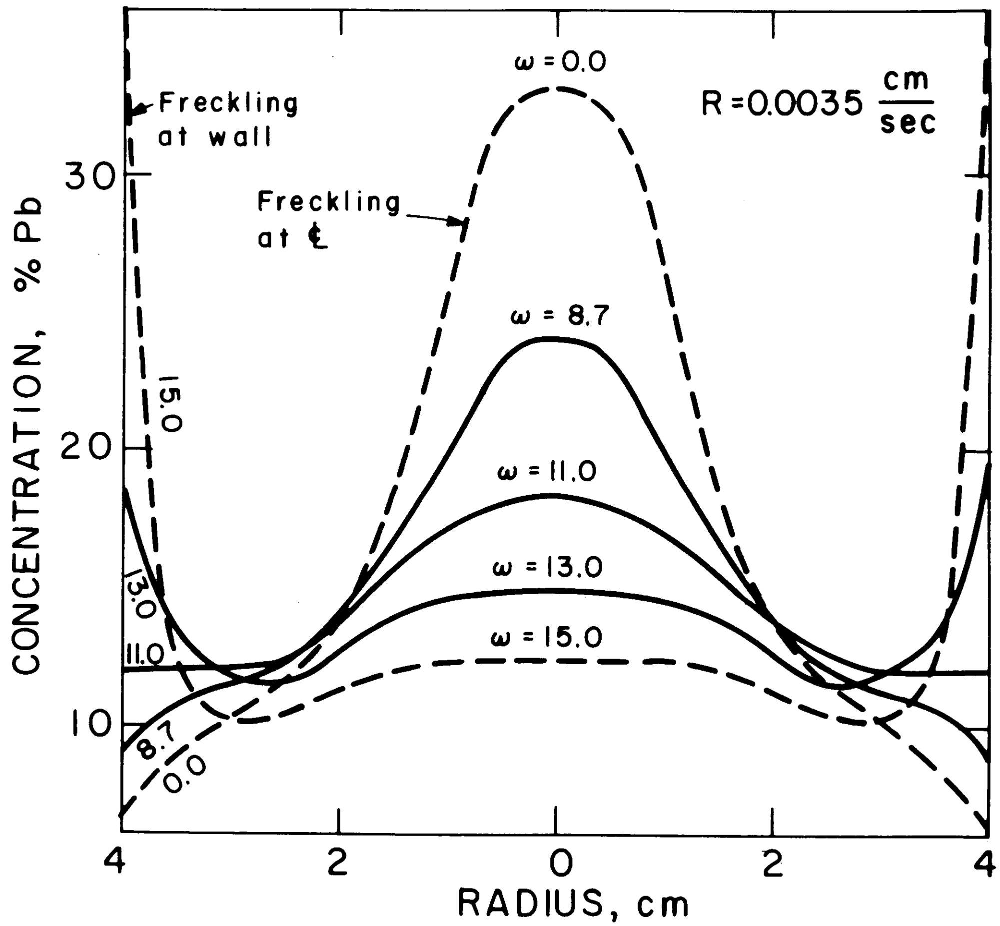

Figure 62: Effect of centrifugal force on macrosegregation across Ingot 8 when solidification rate is 0.0035 cm/sec.

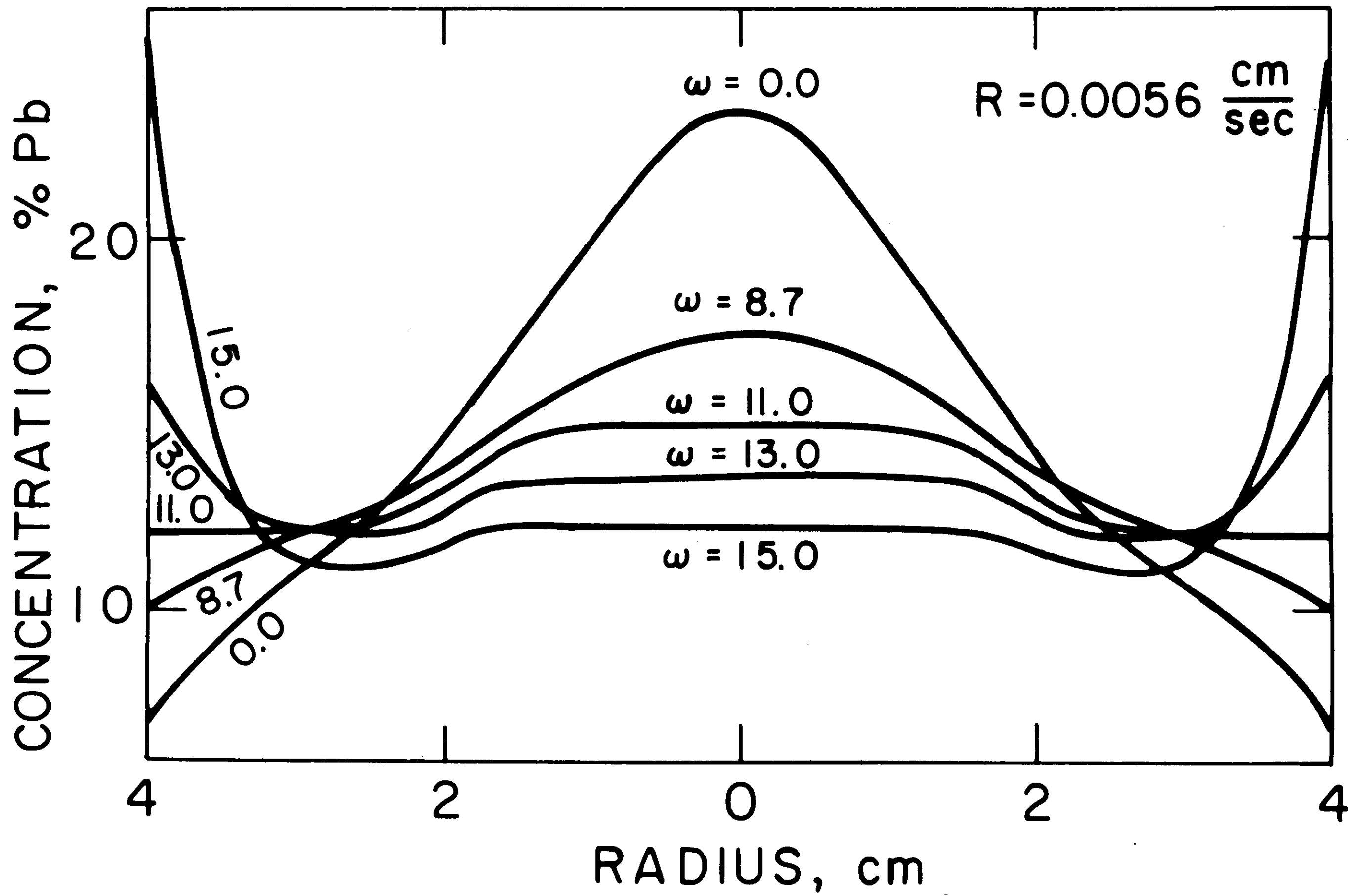

Figure 63: Effect of centrifugal force on macrosegregation across Ingot 8 when solidification rate is 0.0056 cm/sec.

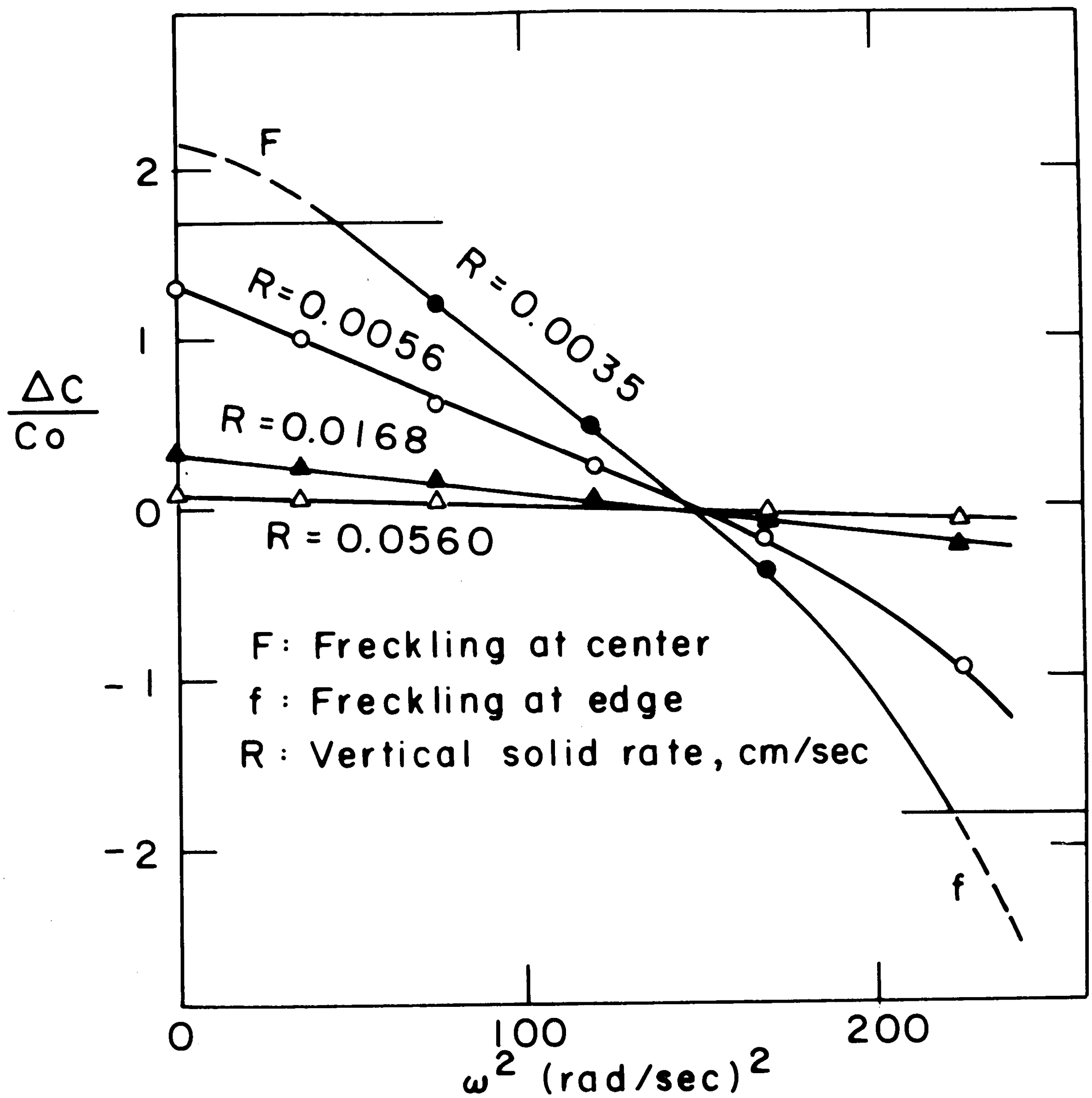

Figure 64: Influence of solidification rates on the spinning effect in Ingot 8.

TABLE 4

LIST OF COMPUTER NOTATIONS

Computer Notation	Algebraic Notation	Explanation of Symbols
A1,A2,A3		Components of AX
A1L(I)		Dimensionized slope of liquids isotherm
A1S(I)		Dimensionized slope of solidus isotherm
ALFA	α	$\beta/[(1-k)/C_L]$
AX	A	A1+A2+A3
B	B	B1+B2
B1,B2		Components of B
C	C	C3-C4-C5-C6
C1, ..., C6		Components of C
CE	C_E	Eutectic composition
CL(I,J)	C_L	Composition of liquid at (I,J)
CO	C_o	Composition of bulk liquid
CONTR		$\rho_{SE}/\rho_{LE}-1$
CONTRL		$\rho_S/\rho_{LO}-1$
CRAT		C_o-C_E
CSE	C_{SE}	Composition of solid in equilibrium with liquid at eutectic temperature
CSINGT		Average ingot composition
CS(J)	C_S	Composition of solid
DECLR	$\partial C_L/\partial r$	Radial gradient of C_L

Computer Notation	Algebraic Notation	Explanation of Symbols
DECLZ	$\partial C_L / \partial z$	Vertical gradient of C_L
DEGLR	$\partial g_L / \partial r$	Radial gradient of g_L
DEGLZ	$\partial g_L / \partial z$	Vertical gradient of g_L
DELRAD	HC or HC/2	Horizontal spacing
DEPMZ		Depth of mushy zone
DERHOR	$\partial \rho_L / \partial r$	Radial gradient of ρ_L
DERHOZ	$\partial \rho_L / \partial z$	Vertical gradient of ρ_L
DIFTEM		T(I,J)-TE
DRODCL	$d\rho_L/dC_L$	Variation of ρ_L with C_L
EM	m	(TE-TM)/CE
EPPS(I,J)		ε at (I,J)
FOR(I,J)		Coefficient of finite difference equation
GADS	γ_o	Permeability at the centerline of mushy zone
GAMMA	γ	Permeability
GE		Scheil's fraction eutectic
GEE	g_E	Real fraction eutectic
GLE		Fraction eutectic
GLEUT(I)		Dimensionized GEE
GL(I,J)	g_L	Fraction liquid
GRAV	g	Gravitational acceleration
GR(I,J)	$\partial T/\partial r$	Radial temperature gradient at (I,J)
GS(I,J)	g_s	Fraction solid
GZ(I,J)	$\partial T/\partial z$	Vertical temperature gradient at (I,J)

Computer Notation	Algebraic Notation	Explanation of Symbols
HA	h_a	Right horizontal grid spacing
HB	h_b	Left horizontal grid spacing
HC	Δr	Radial spacing increment
HEIT(I)		Maximum depth of metal pool at column I
HORAT		$\rho_o - \rho_{LE}$
HTE		Depth of mushy zone at the center
HTMZ		HTT(I) - DEPMZ
HTFRAC		HTMZ/HTT(I)
HTT(I)		ZL(I) - ZS(I)
I		Column designation
IMAX		Column at wall
IMAXN		IMAX-1
ITER		Iteration step
J		Row designation
JJ1(I), ..., JJ5(1)		Column selection for output
JMIN(I)		Minimum value of J at column I
JMN(I)		JMIN(I+1)
JWALL		JMIN(I) at I=IMAX
KAY	k	Partition ratio
KA	k_a	Upper vertical grid spacing
KB	k_b	Lower vertical grid spacing
KC	k_c	Vertical spacing increment
KONST(I,J)		Coefficient of finite difference equation
LOCCOM(I)	$\bar{C}_s$	Local average composition at column I

Computer Notation	Algebraic Notation	Explanation of Symbols
MAXITI		Maximum number of iterations
MLIQ		Slope of liquids isotherm
MO(I,J)		Slope of isotherm at (I,J)
MSOL		Slope of solidus isotherm
MU	μ	Viscosity
NLGL(J)	$\ln g_L$	Natural log of fraction liquid
NMT		NT(I)-1
NNT		NT(I)
NSI(I)		JMIN(I)+1
NT(I)		Top row of column I
NTOP		Maximum number of rows
ONE(I,J)		Coefficient of finite difference equation
PA	P_o	Atmospheric pressure
PERMI(I,J)	K	$\gamma g_L^{\ 2}$
P(I,J)		Pressure at (I,J)
PDR	$\partial P/\partial r$	Radial pressure gradient
PDZ	$\partial P/\partial z$	Vertical pressure gradient
PPP		JMIN(I)
Q1, ... Q8		Coefficients of finite difference equation
RADIUS		Radius of Ingot
RARA		$\vec{V}\cdot\nabla T/\varepsilon$
RATER		$\vec{v}\cdot\nabla T$
RHO(I,J)	ρ_L	Liquid density at (I,J)
R(I,J)	r	Radius at (I,J)

Computer Notation	Algebraic Notation	Explanation of Symbols
RE	ρ_S	Solid density
RFRACS		(RS(J) - R(I,J))/HC
RL(J)		Radius of liquidus isotherm at row J
RLE	ρ_{LE}	Density of liquid eutectic
RO	ρ_{LO}	Density of bulk liquid
ROR(I)		Radius at column I
RR		
RS(J)		Radius of solidus isotherm at row J
RSE	ρ_{SE}	Density of eutectic solid
SOLHZ		$\partial p/\partial r$ at boundary point 1
SOLVE		$\partial p/\partial z$ at boundary point 2
T(I,J)	T	Temperature at (I,J)
TABOT(I,J)		Coefficient of finite difference equation
TAKONS(I,J)		Coefficient of finite difference equation
TALEFT(I,J)		Coefficient of finite difference equation
TART(I,J)		Coefficient of finite difference equation
TATOP(I,J)		Coefficient of finite difference equation
TE	T_E	Eutectic temperature
TL	T_L	Liquidus temperature
TM		Melting point of pure solvent
TRAT		TL-TE
TRE(I,J)		Coefficient of finite difference equation
TTHETA	θ	Angle
TWO(I,J)		Coefficient of finite difference equation

Computer Notation	Algebraic Notation	Explanation of Symbols
TYPE		Different types of pressure calculation
UR	U_r	r-component of $\vec{U}$
UZ(I,J)	U_z	z-component of $\vec{U}$
UZCL		Casting speed
VR	v_r	r-component of $\vec{v}$
VTOT	$\lvert\vec{v}\rvert$	Magnitude of $\vec{v}$
VZ	v_z	z-component of $\vec{v}$
W	ω	Angular velocity
Z(I,J)	z	Height of node (I,J)
ZAT(I)		Ratio of 2nd D.A.S. to 2nd D.A.S. at centerline
ZFRACS		(Z(I,J)-ZS(I))/KC
ZILIQ		Height of liquidus at centerline
ZISOL		Height of solidus at centerline
ZL(I)		Height of liquidus isotherm at column I
ZLHIGH		ZL(I) at wall
ZS(I)		Height of solidus isotherm at column I

APPENDIX A - Composition and Density of Interdendritic Liquid

In the "local solute redistribution equation", it is assumed that equilibrium exists at the interface between the interdendritic liquid and the solid phase (5). Therefore, the temperature of a solidifying alloy is dictated by the liquidus line on the corresponding phase diagram, and the composition of interdendritic liquid is a function of temperature only, i.e., $C_L = C_L(T)$. The temperature, T, is a function of position and time, i.e., $T = T(r,z,t)$. Therefore, from chain rule,

$$\left(\frac{\partial C_L}{\partial t}\right)_{r,z} = \left(\frac{dC_L}{dT}\right) \left(\frac{\partial T}{\partial t}\right)_{r,z} = \frac{\varepsilon}{m} \qquad (13)$$

where m is the slope of the liquidus line of the phase diagram (Figures 2(a), 3(a), and ε is the cooling rate. By substituting Equation (13) into Equation (4), we get Equation (5).

The density of a liquid is a function of both composition and temperature. But, since $C_L = C_L(T)$ we can write for the interdendritic liquid that $\rho_L = \rho_L(C_L)$. Since $C_L = C_L(r,z,t)$, from chain rule, we get

$$\left(\frac{\partial \rho_L}{\partial t}\right)_{r,z} = \left(\frac{d\rho_L}{dC_L}\right) \left(\frac{\partial C_L}{\partial t}\right)_{r,z} = \left(\frac{d\rho_L}{dC_L}\right) \frac{\varepsilon}{m} \qquad (6)$$

where $d\rho_L/dC_L$ is the slope of the ρ_L versus C_L plot for the interdendritic liquid (Figures 2b and 3b).

APPENDIX B - FLOW DIAGRAM

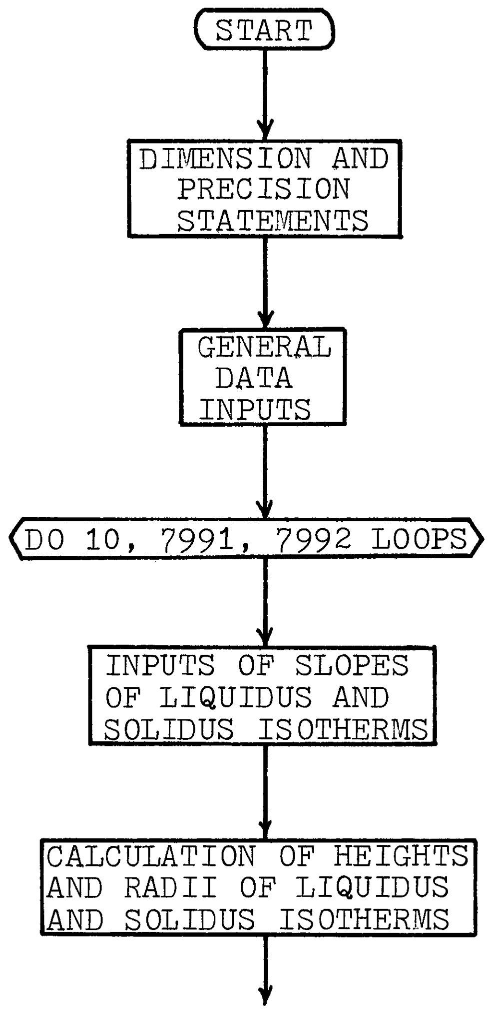

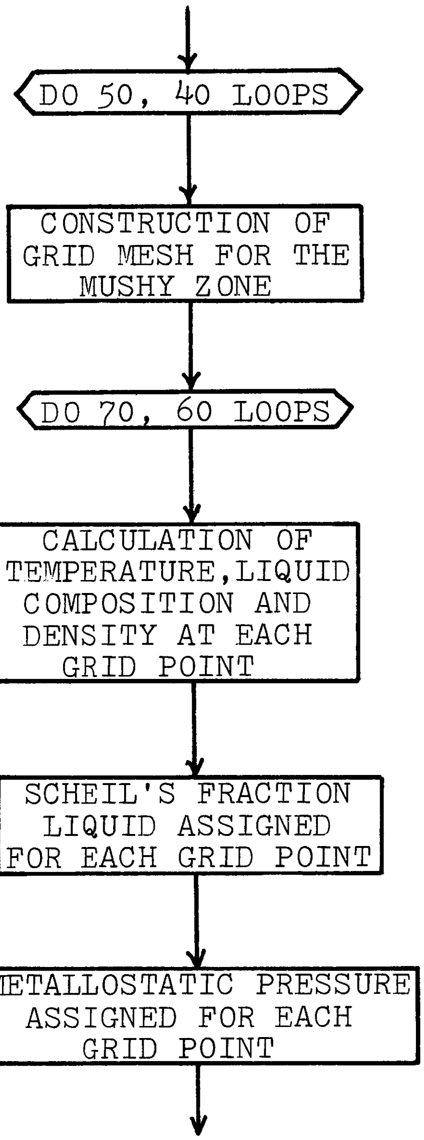
DO 50, 40 LOOPS
CONSTRUCTION OF GRID MESH FOR THE MUSHY ZONE
DO 70, 60 LOOPS
CALCULATION OF TEMPERATURE, LIQUID COMPOSITION AND DENSITY AT EACH GRID POINT
SCHEIL'S FRACTION LIQUID ASSIGNED FOR EACH GRID POINT
METALLOSTATIC PRESSURE ASSIGNED FOR EACH GRID POINT

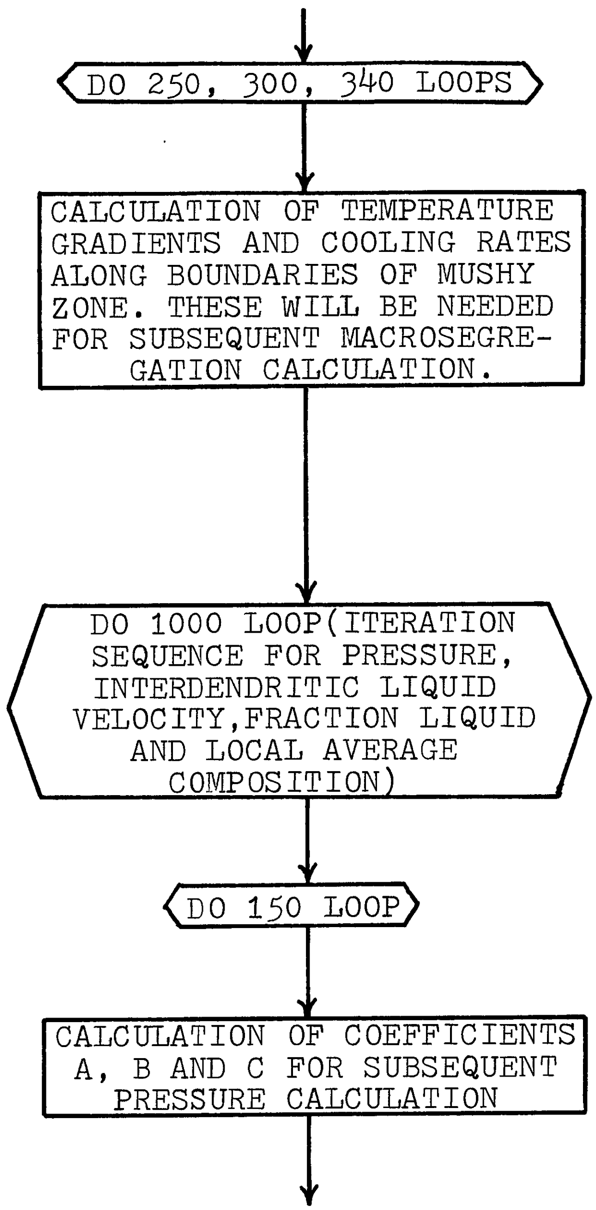
DO 250, 300, 340 LOOPS
CALCULATION OF TEMPERATURE GRADIENTS AND COOLING RATES ALONG BOUNDARIES OF MUSHY ZONE. THESE WILL BE NEEDED FOR SUBSEQUENT MACROSEGREGATION CALCULATION.
DO 1000 LOOP(ITERATION SEQUENCE FOR PRESSURE, INTERDENDRITIC LIQUID VELOCITY,FRACTION LIQUID AND LOCAL AVERAGE COMPOSITION)
DO 150 LOOP
CALCULATION OF COEFFICIENTS A, B AND C FOR SUBSEQUENT PRESSURE CALCULATION

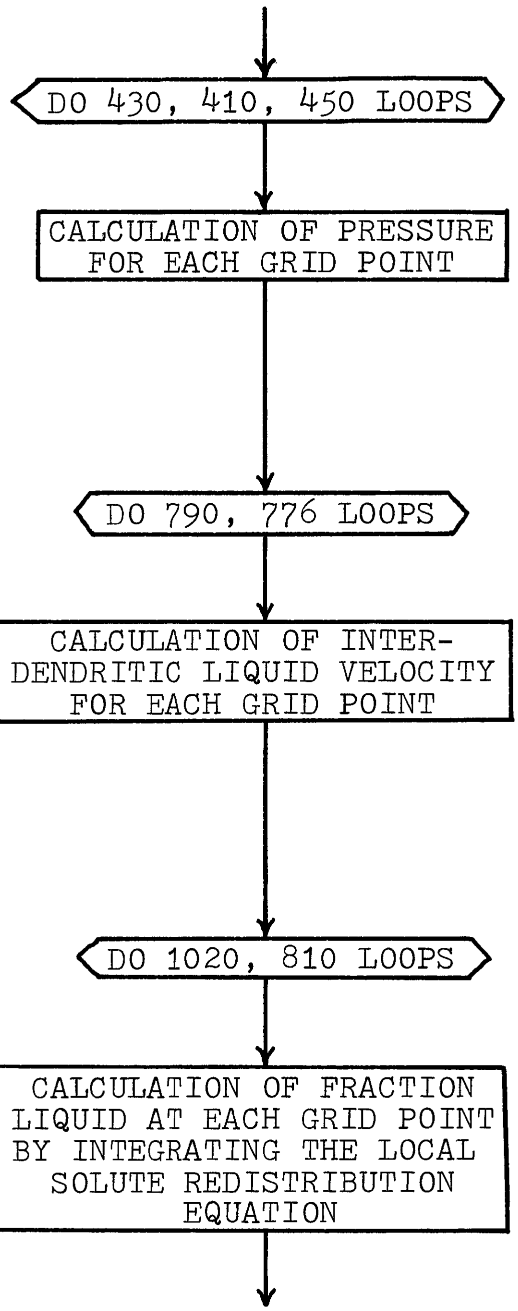
DO 430, 410, 450 LOOPS
CALCULATION OF PRESSURE FOR EACH GRID POINT
DO 790, 776 LOOPS
CALCULATION OF INTER-DENDRITIC LIQUID VELOCITY FOR EACH GRID POINT
DO 1020, 810 LOOPS
CALCULATION OF FRACTION LIQUID AT EACH GRID POINT BY INTEGRATING THE LOCAL SOLUTE REDISTRIBUTION EQUATION

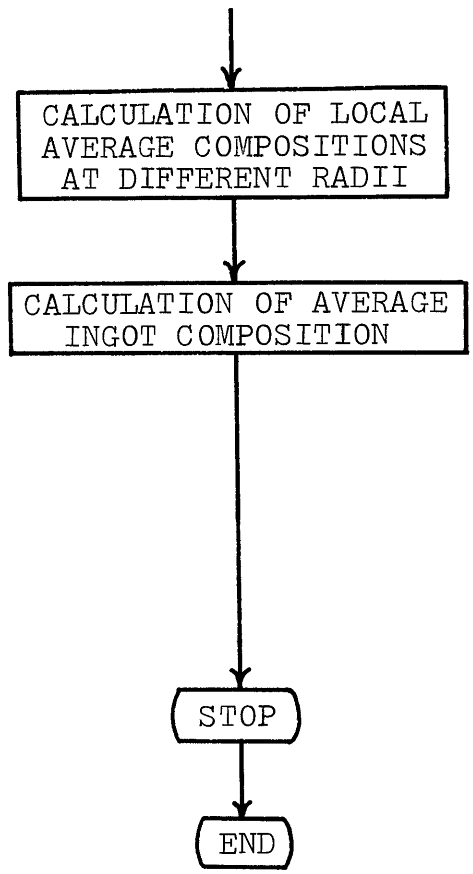
CALCULATION OF LOCAL AVERAGE COMPOSITIONS AT DIFFERENT RADII
CALCULATION OF AVERAGE INGOT COMPOSITION
STOP
END

APPENDIX C

FINITE DIFFERENCE FORMS OF PRESSURE DISTRIBUTION EQUATION

1. Interior Grid Points

$$\left.\frac{\partial P}{\partial r}\right|_{I,J} = (P(I+1,J) - P(I-1,J))/(2h_b)$$

$$\left.\frac{\partial P}{\partial z}\right|_{I,J} = (P(I,J+1) - P(I,J-1))/(2k_a)$$

$$\left.\frac{\partial^2 P}{\partial r^2}\right|_{I,J} = (P(I+1,J) + P(I-1,J) - 2P(I,J))/(h_b^{\,2})$$

$$\left.\frac{\partial^2 P}{\partial z^2}\right|_{I,J} = (P(I,J+1) + P(I,J-1)- 2P(I,J)/(k_a^{\,2})$$

Substituting these equations into the pressure distribution equation, Eqn (8), we get

$$\begin{aligned} P(I,J) = {} & ONE(I,J)\ P(I+1,J) \\ & + TWO(I,J)\ P(I,J+1) \\ & + TRE(I,J)\ P(I-1,J) \\ & + FOR(I,J)\ P(I,J-1) \\ & + KONST(I,J) \end{aligned}$$

where

$$ONE(I,J) = (h_b^{-2} + A(I,J)\ (2h_b)^{-1}) \cdot (2h_b^{-2} + 2k_a^{-2})^{-1}$$

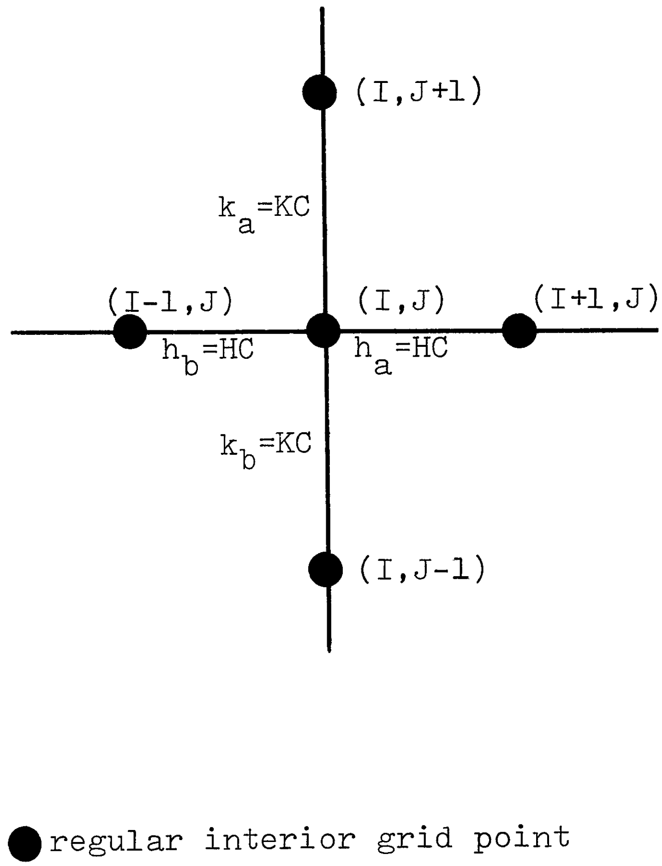
(I,J+1)
k_a=KC
(I-1,J)
(I,J)
(I+1,J)
h_b=HC
h_a=HC
k_b=KC
(I,J-1)
regular interior grid point

$$TWO(I,J) = (k_a^{-2} + B(I,J)(2k_a)^{-1}) \cdot (2h_b^{-2} + 2k_a^{-2})$$

$$TRE(I,J) = (h_b^{-2} - A(I,J)(2h_b)^{-1}) \cdot (2h_b^{-2} + 2k_a^{-2})$$

$$FOR(I,J) = (k_a^{-2} - B(I,J)(2k_a)^{-1}) \cdot (2h_b^{-2} + 2k_a^{-2})$$

$$KONST(I,J) = C \cdot (2h_b^{-2} + 2k_a^{-2})$$

2. Solidus Interior Grid Points

Solidus interior grid points are those grid points inside the mushy zone and just next to the solidus isotherm. They can be classified into three types. Each type has its own finite difference form of the pressure distribution equation.

Type A: $ZFRACS \leq 1.0$ and $RFRACS \leq 1.0$

Type B: $ZFRACS \leq 1.0$ and $RFRACS > 1.0$

Type C: $ZFRACS > 1.0$ and $RFRACS \leq 1.0$

where

$$ZFRACS = (Z(I,J) - ZS(I))/KC$$

and

$$RFRACS = (RS(I) - R(I,J))/HC$$

Type A:

From Darcy's law and the solidus boundary condition, we get the following relation for point 1:

$$\text{SOLHZ} = \left.\frac{\partial P}{\partial r}\right|_1 = \frac{\mu}{\gamma g_{LE}} \left(\frac{\rho_{SE}}{\rho_{LE}} - 1\right) U_{rE} + \rho_{LE}\omega^2 r$$

Similarly, at point 2, we have:

$$\text{SOLVE} = \left.\frac{\partial P}{\partial z}\right|_2 = \frac{\mu}{\gamma g_{LE}} \left(\frac{\rho_{SE}}{\rho_{LE}} - 1\right) U_{zE} - \rho_{LE}\, g$$

Using the "Level Rule" for unequal grid spacings around (I,J), we have:

$$\left.\frac{\partial P}{\partial r}\right|_{I,J} = \text{SOLHZ}\cdot h_b/(h_a + h_b) + (P(I,J)-P(I-2,J))\cdot(h_a/2h_b)/(h_a+h_b)$$

$$\left.\frac{\partial P}{\partial z}\right|_{I,J} = \text{SOLVE}\cdot k_a/(k_a+k_b) + (P(I,J+2)-P(I,J))\cdot(k_b/2k_a)/(k_a+k_b)$$

$$\left.\frac{\partial^2 P}{\partial r^2}\right|_{I,J} = (\text{SOLHZ} - (P(I,J) - P(I-2,J))/(2h_b))/(h_a+h_b)$$

$$\left.\frac{\partial^2 P}{\partial z^2}\right|_{I,J} = ((P(I,J+2) - P(I,J))/(2k_a) - \text{SOLVE})/(k_a+k_b)$$

Substituting these equations into the pressure distribution equation, Eqn (8), we get

$$P(I,J) = \text{TATOP}(I,J)\ P(I,J+2) + \text{TALEFT}(I,J)\ P(I-2,J) + \text{TAKONS}(I,J)$$

Type A:

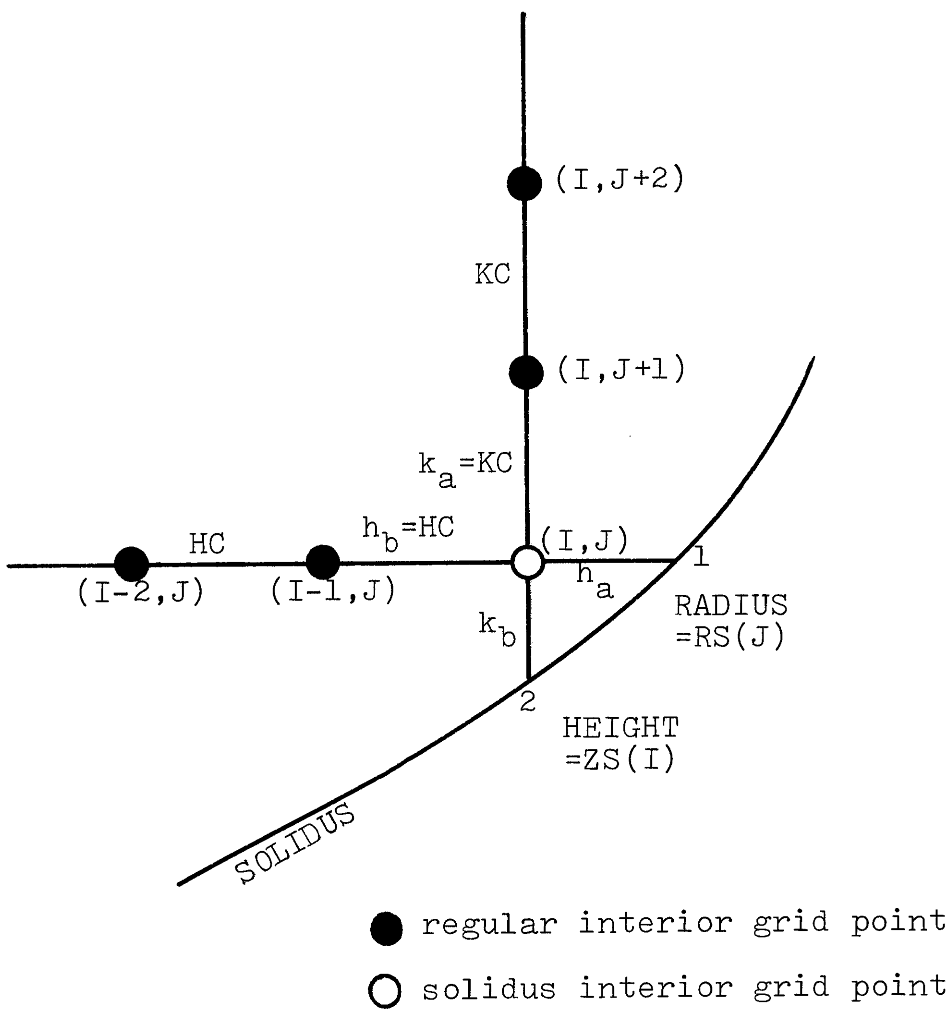

(I,J+2)
KC
(I,J+1)
k_a=KC
h_b=HC
HC
(I,J)
1
h_a
(I-2,J)
(I-1,J)
RADIUS
=RS(J)
k_b
2
HEIGHT
=ZS(I)
SOLIDUS
regular interior grid point
solidus interior grid point

where

$$TATOP(I,J) = (Q2+Q4)/Q6$$

$$TALEFT(I,J) = (Q1-Q3)/Q6$$

$$TAKONS(I,J) = Q5/Q6$$

$$Q1 = (2h_b(h_a+h_b))^{-1}$$

$$Q2 = (2k_a(k_a+k_b))^{-1}$$

$$Q3 = h_a A(I,J)Q1$$

$$Q4 = k_b B(I,J)Q2$$

$$Q5 = SOLHZ\cdot(h_a+h_b)^{-1}\ (1 + h_b A(I,J))$$

$$- SOLVE\cdot(k_a+k_b)^{-1}\ (1-k_a B(I,J)) + C(I,J)$$

$$Q6 = Q1 + Q2 - Q3 + Q4$$

<u>Type B</u>:

$\left.\frac{\partial P}{\partial r}\right|_{I,J}$ and $\left.\frac{\partial^2 P}{\partial r^2}\right|_{I,J}$ are the same as in the case of interior grid points. While $\left.\frac{\partial P}{\partial z}\right|_{I,J}$, $\left.\frac{\partial^2 P}{\partial z^2}\right|_{I,J}$ and SOLVE are the same as in Type A. Substituting these into the pressure distribution equation, Eqn. (8), we get:

$$P(I,J) = TART(I,J)\ P(I+1,J) + TATOP(I,J)\ P(I,J+2)$$

$$+ TALEFT(I,J)\ P(I-1,J) + TAKONS(I,J)$$

where

$$TART(I,J) = (h_b^{-2} + A(I,J)(2h_b)^{-1})/(Q2+Q4+2h_b^{-2})$$

$$TALEFT(I,J) = (h_b^{-2} - A(I,J)(2h_b)^{-1})/(Q2+Q4+2h_b^{-2})$$

$$TATOP(I,J) = (Q2+Q4)/(Q2+Q4+2h_b^{-2})$$

Type B:

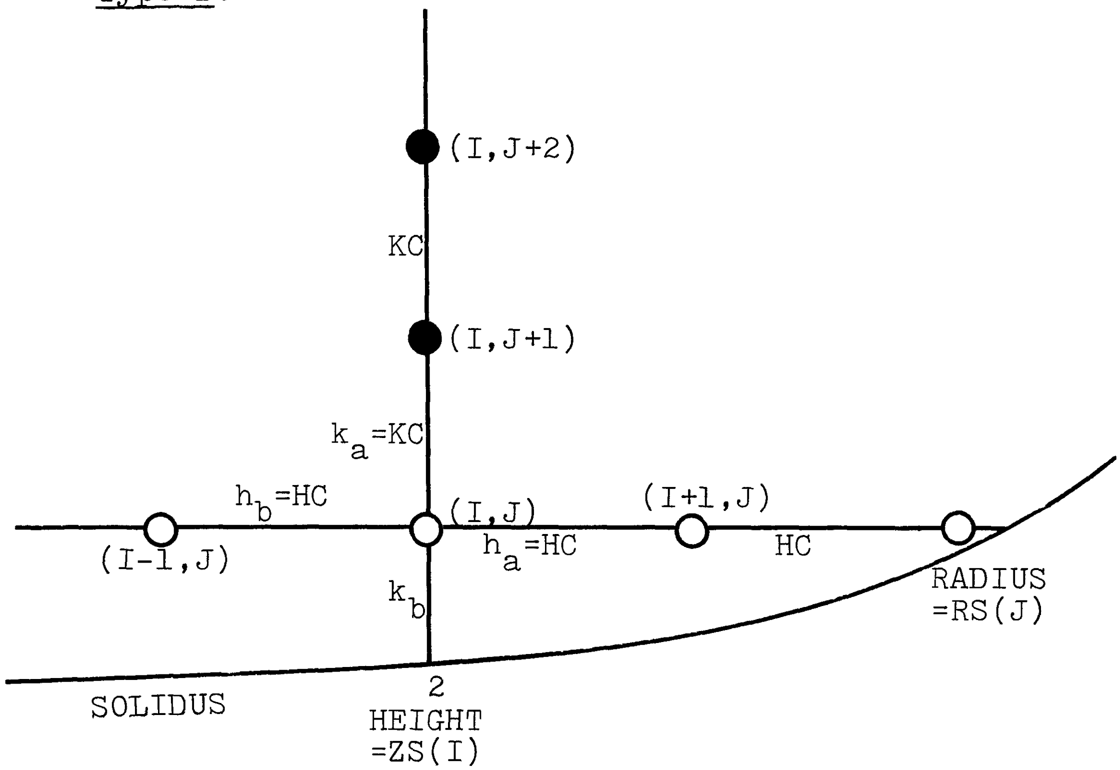

● regular interior grid point

○ solidus interior grid point

$$TAKONS(I,J) = Q7/(Q2+Q4+2h_b^{-2})$$

$$Q7 = -SOLVE\cdot(k_a+k_b)^{-1}\ (1-k_aB(I,J)) + C(I,J)$$

Q2 and Q4 are the same as in Type A.

Type C:

$\left.\frac{\partial P}{\partial z}\right|_{I,J}$ and $\left.\frac{\partial^2 P}{\partial z^2}\right|_{I,J}$ are the same as in the case of interior grid points. While $\left.\frac{\partial P}{\partial r}\right|_{I,J}$, $\left.\frac{\partial^2 P}{\partial r^2}\right|_{I,J}$ and SOLHZ are the same as Type A. Substituting these into the pressure distribution equation, Eqn. (8), we get

$$P(I,J) = TATOP(I,J)\ P(I,J+1) + TALEFT(I,J)\ P(I-2,J) + TABOT(I,J)\ P(I,J-1) + TAKONS(I,J)$$

where

$$TATOP(I,J) = (k_a^{-2} + B(I,J)(2k_a)^{-1})/(Q1-Q3+2k_a^{-2})$$

$$TALEFT(I,J) = (Q1-Q3)/(Q1-Q3+2k_a^{-2})$$

$$TABOT(I,J) = (k_a^{-2} - B(I,J)(2k_a)^{-1})/(Q1-Q3+2k_a^{-2})$$

$$TAKONS(I,J) = Q8/(Q1-Q3+2k_a^{-2})$$

$$Q8 = SOLHZ\cdot(h_a+h_b)^{-1}\ (1+h_bA(I,J)) + C(I,J)$$

Q1 and Q3 are the same as in Type A.

Type C:

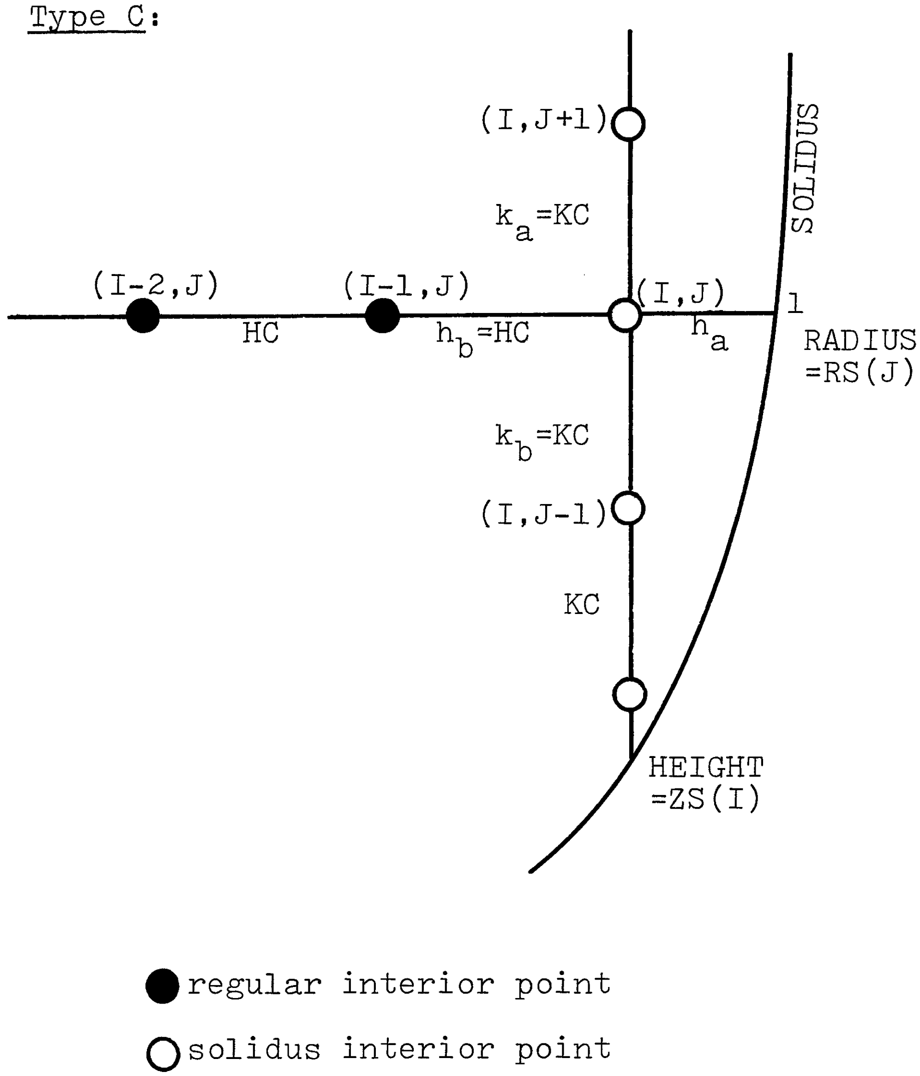
(I,J+1)
SOLIDUS
k_a=KC
(I-2,J)
(I-1,J)
(I,J)
1
HC
h_b=HC
h_a
RADIUS
=RS(J)
k_b=KC
(I,J-1)
KC
HEIGHT
=ZS(I)
regular interior point
solidus interior point

3. Centerline Grid Points

$$\left.\frac{\partial P}{\partial r}\right|_{I,J}, \left.\frac{\partial^2 P}{\partial r^2}\right|_{I,J}, \left.\frac{\partial P}{\partial z}\right|_{I,J} \text{ and } \left.\frac{\partial^2 P}{\partial z^2}\right|_{I,J}$$ are the same as in the case of interior grid point. But since all properties are symmetrical with respect to the centerline, P(I-I,J) equals to P(I+1,J) and $A \frac{\partial P}{\partial r}$ of the pressure distribution equation now equals to $\frac{\partial^2 P}{\partial r^2}$. Substituting these into the pressure distribution equation, Eq. (8), we get

$$
\begin{aligned}
P(I,J) = {} & ONE(I,J)\ P(I+1,J) \\
& + TWO\ (I,J)\ P(I,\ J+1) \\
& + FOR\ (I,J)\ P(I,J-1) \\
& + KONST\ (I,J)
\end{aligned}
$$

where

$$ONE(I,J) = (4\ h_b^{-2})\cdot(4h_b^{-2} + 2k_a^{-2})^{-1}$$

$$TWO(I,J) = (k_a^{-2} + B(I,J)(2k_a)^{-1})\cdot(4h_b^{-2} + 2k_a^{-2})^{-1}$$

$$FOR(I,J) = (k_a^{-2} - B(I,J)(2k_a)^{-1})\cdot(4h_b^{-2} + 2k_a^{-2})^{-1}$$

$$KONST(I,J) = C(I,J)\cdot(4h_b^{-2} + 2k_a^{-2})^{-1}$$

4. Wall Grid Points

$$\left.\frac{\partial P}{\partial r}\right|_{I,J}, \left.\frac{\partial^2 P}{\partial r^2}\right|_{I,J}, \left.\frac{\partial P}{\partial z}\right|_{I,J} \text{ and } \left.\frac{\partial^2 P}{\partial z^2}\right|_{I,J}$$

are the same as in the case of interior grid points. But now because of the wall boundary condition, $P(I+1,J) = P(I-1,J) + (2h_b)\,\rho_L(I,J)\,\omega^2 R$, where R is the radius of the mold. Substituting these into the pressure distribution equation, we get

$$P(I,J) = TWO(I,J)\ P(I,J+1)$$
$$+\ TRE(I,J)\ P(I-1,J)$$
$$+\ FOR(I,J)\ P(I,J-1)$$
$$+\ KONST(I,J)$$

where

$$TWO(I,J) = (k_a^{-2} + B(I,J)(2k_a)^{-1})\cdot(2h_b^{-2} + 2k_a^{-2})^{-1}$$
$$TRE(I,J) = (2h_b^{-2})\cdot(2h_b^{-2} + 2k_a^{-2})^{-1}$$
$$FOR(I,J) = (k_a^{-2} - B(I,J)(2k_a)^{-1})\cdot(2h_b^{-2} + 2k_a^{-2})^{-1}$$
$$KONST)I,J) = (\rho_L\omega^2 R(2h_b^{-1} + A(I,J)) + C(I,J))\cdot$$
$$\cdot(2h_b^{-2} + 2k_a^{-2})^{-1}$$

APPENDIX D

```
C ************************************************************************
C ************************************************************************
C     THIS IS INGOT 1
C ************************************************************************
C ************************************************************************
C
C
C
C******************************************************
C   DIMENSION AND PRECISION STATEMENTS****BEGIN
C******************************************************
C
      INTEGER PT1
      INTEGER NPARAM
      INTEGER*4 N
      INTEGER PPPMAX
      INTEGER PPP
      INTEGER NSI(25),NSIMAX(25),JMIN(25),NT(25),JMN(25)
      REAL*8 THEDA7,THEDA8,THEDA9
      REAL*4 ROO(25),COO(25)
      INTEGER JJ1(25),JJ2(25),JJ3(25),JJ4(25)
      INTEGER JJ5(25),JJ6(25),JJ7(25),JJ8(25)
      REAL*8 D(22,82),E(22,82),F(22,82)
      REAL*8 KAB,KAC,KBB
      REAL*4 NLGE
      REAL*8 ANG
      REAL*8 GADS
      REAL*8 ZZZ,ZZZZ
      REAL*8 VR(22,82),VZ(22,82)
      REAL*4 NLGL(82),FN(82)
      REAL*4 GS(82)
      REAL*4 LOCCOM(22),CS(82)
      REAL*8 MSOL,MLIQ
      REAL*8 KSOL,KLIQ,K,KB,KM,KT
```

```
REAL*8 THEDA1,THEDA2,THEDA3,THEDA4,THEDA5,THEDA6
REAL*8 EPPSE
REAL*8 Q1,Q2,Q3,Q4,Q5,Q6,Q7,Q8
REAL*8 LEFT,KC,KAY,KA
REAL*8 KON1,KON2,KON3,KON4
REAL*8 GAMO1,GAMO2,CONSTT
REAL*4 SLOLIQ,SLOSOL
REAL*4 LTSEG
REAL*8 RSS(82),RL(82)
REAL*8 ZOZ(82)
REAL*8 VZE(25),VRE(25)
REAL*8 RS(82)
REAL*4 ROR(25)
REAL*8 HTT(25),HEIT(25),GRAV,EM,DTT
REAL*8 HTE,TL,TE,HORAT,CRAT,TRAT,RADIUS
REAL*8 RO,RLE,RSE,RE,GE,MU,CO,CE
REAL*8 H,HA,HB,HC,HM,HT
REAL*8 DABS
REAL*8 UR,UZ(22,82),ZL(25),ZS(25)
REAL*8 PA
REAL*8 SOLVE,SOLHZ
REAL*4 A1S(25),A1L(25),DELA1(25)
REAL*8 TABOT(22,82),TAKONS(22,82)
REAL*8 TART(22,82),TATOP(22,82),TALEFT(22,82)
REAL*8 GOPS
REAL*8 T(22,82),RHO(22,82),MO(22,82)
REAL*8 CL(22,82),GL(22,82),Z(22,82),R(22,82)
REAL*8 UZURRO,UZURCL,DERHOR,DERHOZ,DECLR,DECLZ,DEGLR,DEGLZ
REAL*8 DENOM1,DENOM2,THETA
REAL*8 ONE(22,82),TWO(22,82),TRE(22,82),FOR(22,82)
REAL*8 PERMI(22,82),GAMMA(22,82)
REAL*8 GR(22,82),GZ(22,82),EPPS(22,82)
REAL*8 A1,A2,A3,B1,B2,C1,C2,C3,C4
REAL*8 AX,B,C
REAL*8 P(22,82),KONST(22,82)
REAL*8 ZAT(22)
```

```
      REAL*8 A(82),X1,X2
      REAL*8 PDR,PDZ
      REAL*8 GLEUT(25)
C
C    DIMENSION AND PRECISION STATEMENTS****END
C
C
C*******************************************
C    GENERAL DATA INPUTS*************BEGIN
C*******************************************
C
      NTOP=70
      ZILIQ=3.8
      UZCL=0.053
      CO=4.40
      GADS=5.0D-7
      W=0.0
      MAXIT1=110
      MU=.013
      PA=1.0D6
      TRIG=1
      HC=0.25
      KC=0.14
      RADIUS=3.4
      ZISOL=0.0
      DTT=0.
      GRAV=980.
      RO=2.45
      PI=3.14156
      RSE=3.38
      RLE=3.2
      RE=2.62
      TE=548.
      TM=660.
      CSE=5.65
      CE=33.
```

```
C
C    INPUT OF (2'NDARY D.A.S./2'NDARY D.A.S. AT CENTER LINE)
C
      ZAT(1)=1.0
      ZAT(2)=1.0
      ZAT(3)=1.0
      ZAT(4)=1.0
      ZAT(5)=1.0
      ZAT(6)=1.0
      ZAT(7)=1.0
      ZAT(8)=1.0
      ZAT(9)=1.0
      ZAT(10)=1.0
      ZAT(11)=1.0
      ZAT(12)=1.0
      ZAT(13)=1.0
      ZAT(14)=1.0
      ZAT(15)=1.0
      ZAT(16)=1.0
      ZAT(17)=1.0
C
C    GENERAL DATA INPUTS*************END
C
      IMAX=RADIUS/HC+.0001
      IMAX=IMAX+1
      J1MAX=ZILIQ/KC+0.0001
      J1MAX=J1MAX+1
      DRODCL=(RO-RLE)/(CO-CE)
      KAY=CSE/CE
      KON1=(1.0D0/CO)**(1./(KAY-1.))
      KON2=1.0D0/(KAY-1.0D0)
      KON3=KON2-1.0D0
      KON4=-KON2
      KAY=CSE/CE
      GE=(CE/CO)**(1./(KAY-1.))
      EM=(TE-TM)/CE
```

```
      TL=EM*(CO-CE)+TE
      CONTR=RSE/RLE-1.
      CONTRL=(RE/RO-1.)
      HORAT=RO-RLE
      TRAT=TL-TE
      CRAT=CO-CE
      IMAXN=IMAX-1
      IMAXP=IMAX+1
      WRITE(6,5650) IMAX,J1MAX
 5650 FORMAT(1X,2I16)
      DO 8 I=1,IMAX
      GLEUT(I)=GE
    8 CONTINUE
      WRITE(6,6925)
 6925 FORMAT(12X,'**********',10X,'***********',8X,'***')
      WRITE(6,9000)
 9000 FORMAT(12X,'Z-SOLIDUS',10X,'Z-LIQUIDUS',9X,'I')
      WRITE(6,6926)
 6926 FORMAT(12X,'**********',10X,'***********',8X,'***'/)
C
C**********************************************************************
C   CALCULATION OF HFIGHTS OF LIQUIDUS POINTS, AND HEIGHTS & RADIUS OF
C   SOLIDUS POINT****BEGIN
C**********************************************************************
C
      DO 10 I=1,IMAX
      H=HC
C
C   INPUT OF SLOPES OF SOLIDUS AND LIQUIDUS ISOTHERMS****BEGIN
C
      IF(I.EQ.1) MSOL=0.0
      IF(I.EQ.1) MLIQ=0.0
      IF(I.GT.1) MLIQ=0.80
      IF(I.GT.1) MSOL=0.80
      IF(I.EQ.1) A1S(I)=0.0
      IF(I.EQ.1) A1L(I)=0.0
```

```
C
C   INPUT OF SLOPES OF SOLIDUS AND LIQUIDUS ISOTHERMS****END
C
      A1S(I)=MSOL
      A1L(I)=MLIQ
      IF(I.EQ.1) GO TO 22
      GO TO 23
   22 CONTINUE
      ROR(1)=0.0
      ZS(I)=ZISOL
      ZL(I)=ZILIQ
      GO TO 19
   23 CONTINUE
      ROR(I)=ROR(I-1)+HC
      ZL(I)=ZL(I-1)+A1L(I)*HC
      ZS(I)=ZS(I-1)+A1S(I)*HC
   19 CONTINUE
      WRITE(6,6000) ZS(I),ZL(I),I
 6000 FORMAT(1X,2E20.4,I10/)
   10 CONTINUE
      ZLHIGH=ZL(IMAX)
      DO 11 J=1,NTOP
      IF(J.EQ.1) GO TO 4
      GO TO 5
    4 CONTINUE
      ZOZ(1)=0.0
      GO TO 6
    5 CONTINUE
      ZOZ(J)=ZOZ(J-1)+KC
    6 CONTINUE
   11 CONTINUE
      WRITE(6,6927)
 6927 FORMAT(12X,'*********',12X,'***')
      WRITE(6,6917)
 6917 FORMAT(14X,'RS(J)',15X,'J')
      WRITE(6,6928)
```

```
 6928 FORMAT(12X,'*********',12X,'***'/)
      DO 7991 I=2,IMAX
      SUM=KC
      DO 7992 J=2,NTOP
      IF((ZS(I).GE.SUM).AND.(ZS(I-1).LT.SUM)) GO TO 7993
      GO TO 7994
 7993 RS(J)=(I-1)*HC-HC*((ZS(I)-SUM)/(ZS(I)-ZS(I-1)))
      WRITE(6,7995) RS(J),J
 7995 FORMAT(5X,1E15.4,1I15/)
 7994 SUM=SUM+KC
      IF(ZS(I).LT.SUM) GO TO 7991
 7992 CONTINUE
 7991 CONTINUE
C
C   CALCULATION OF HEIGHTS OF LIQUIDUS POINTS, AND HEIGHTS & RADIUS OF
C   SOLIDUS POINT****END
C
C
C***********************************************************
C                 CONSTRUCTION OF THE GRID MESH****BEGIN
C***********************************************************
C
C          THIS PARTICULAR SECTION DEALS WITH THE SETTING UP OF THE GRID
C          MESH FOR THE MUSHY ZONE
C
      DO 50 I=1,IMAX
      HTT(I)=ZL(I)-ZS(I)
      Z(I,1)=ZISOL
      R(I,1)=ROR(I)
      DO 40 J=2,NTOP
      Z(I,J)=ZOZ(J)
      R(I,J)=ROR(I)
   40 CONTINUE
   50 CONTINUE
      DO 51 I=1,IMAX
      HEIT(I)=ZLHIGH-ZL(I)
```

```
   51 CONTINUE
      DO 53 I=1,IMAX
      DO 41 J=1,NTOP
      IF(Z(I,J).GT.ZS(I)) GO TO 33
      IF(Z(I,J).EQ.ZS(I)) GO TO 35
      GO TO 41
   33 ZFRACS=(Z(I,J)-ZS(I))/KC
      IF(ZFRACS.LT.1.0) GO TO 34
      GO TO 41
   34 JMIN(I)=J
      GO TO 41
   35 JMIN(I)=J+1
      GO TO 41
   41 CONTINUE
   53 CONTINUE
      I=IMAX
      JWALL=JMIN(I)
      JWAL=JWALL-1
      DO 5583 I=1,IMAX
      DO 5584 J=J1MAX,NTOP
      ZZZ=Z(I,J)-ZL(I)
      ZZZZ=DABS(ZZZ)
      IF(ZZZZ.LE.0.001) GO TO 5586
      IF(ZZZ.GT.0.001) GO TO 5585
      GO TO 5584
 5585 ZFRACL=(Z(I,J)-ZL(I))/KC
      IF(ZFRACL.LT.1.0) GO TO 5588
      GO TO 5583
 5588 NT(I)=J-1
      GO TO 5583
 5586 NT(I)=J-1
      GO TO 5583
 5584 CONTINUE
 5583 CONTINUE
C
C   CONSTANTS NEEDED FOR SUBSEQUENT HEIGHT SELECTION IN THE PRINTOUTS
```

```
C
      DO 52 I=1,IMAX
      NUMPTS=NT(I)-JMIN(I)
      N8TH=NUMPTS/5.
      JJ1(I)=JMIN(I)+N8TH
      JJ2(I)=JMIN(I)+2.*N8TH
      JJ3(I)=JMIN(I)+3.*N8TH
      JJ4(I)=JMIN(I)+4.*N8TH
      JJ5(I)=JMIN(I)+5.*N8TH
   52 CONTINUE
      WRITE(6,6929)
 6929 FORMAT(10X,'*************',4X,'***********',7X,'***')
      WRITE(6,9010)
 9010 FORMAT(10X,'VALUE OF JMIN',4X,'VALUE OF NT',8X,'I')
      WRITE(6,6930)
 6930 FORMAT(10X,'*************',4X,'***********',7X,'***'/)
      DO 88 I=1,IMAXN
      NSI(I)=JMIN(I)+1
      JMN(I)=JMIN(I+1)
      IF(JMIN(I).EQ.JMIN(I+1)) JMN(I)=NSI(I)
      WRITE(6,8010) JMIN(I),NT(I),I
 8010 FORMAT(1X,2I16,1I14/)
   88 CONTINUE
C
C   CONSTRUCTION OF THE GRID MESH****END
C
C
C*****************************************************************
C   TEMP AND TEMP RELATED ITEMS FOR EACH NODE****BEGIN
C
C
C   SCHEIL 'GL' AND HYDROSTATIC 'P' ARE ASSIGNED!
C*****************************************************************
C
      I=IMAX
      PPP=JMIN(I)
```

```
      NMT=NT(I)-1
      DO 70 I=1,IMAX
      MNT=JMIN(I)
      NNT=NT(I)
      DO 60 J=MNT,NNT
      DEPMZ=ZL(I)-Z(I,J)
      HTMZ=HTT(I)-DEPMZ
      HTFRAC=HTMZ/HTT(I)
      T(I,J)=TRAT*HTFRAC+TE
      DIFTEM=T(I,J)-TE
      RHO(I,J)=(HORAT/TRAT)*DIFTEM+RLE
      CL(I,J)=(CRAT/TRAT)*DIFTEM+CE
      GL(I,J)=KON1*(CL(I,J)**KON2)
      GAMMA(I,J)=GADS*(ZAT(I))**2
      P(I,J)=.5D0*(RHO(I,J)+RO)*GRAV*DEPMZ+GRAV*RO*HEIT(I)
      P(I,J)=P(I,J)+0.5*RO*(W**2)*(R(I,J)**2)
      P(I,J)=P(I,J)+PA
   60 CONTINUE
   70 CONTINUE
      GL(1,1)=KON1*(CE**KON2)
      GL(IMAX,JWAL)=KON1*(CE**KON2)
      DO 5590 I=1,IMAX
      NNT=NT(I)
      J=NNT+1
      T(I,J)=TL
      RHO(I,J)=RO
      CL(I,J)=CO
      GL(I,J)=1.0
      GAMMA(I,J)=GADS*(ZAT(I))**2
      P(I,J)=RO*GRAV*HEIT(I)+PA+0.5*RO*(W**2)*(R(I,J)**2)
 5590 CONTINUE
C
C
C    TEMP AND TEMP RELATED ITEMS FOR EACH NODE****END
C
C
```

```
C*********************************************************************
C   CALCULATION OF VARIABLES AT BOUNDARIES(NEEDED FOR SUBSEQUENT
C   MACROSEGREGATION CALCULATION)****BEGIN
C*********************************************************************
C
C
C   VARIABLES AT WALL
C
      I=IMAX
      PPP=JMIN(I)
      NMT=NT(I)
      DO 250 J=PPP,NMT
      IF(J.GT.NT(I-1)) GO TO 200
      GO TO 201
  200 GR(I,J)=(TL-T(I,J))/(((ZL(I)-Z(I,J))/(ZL(I)-ZL(I-1)))*HC)
      GO TO 202
  201 GR(I,J)=(T(I,J)-T(I-1,J))/HC
  202 GZ(I,J)=(TL-TE)/(ZL(I)-ZS(I))
      EPPS(I,J)=-GZ(I,J)*UZCL
  250 CONTINUE
      I=IMAX
      J=NT(I)+1
      GZ(I,J)=(TL-TE)/(ZL(I)-ZS(I))
      GR(I,J)=-A1L(I)*GZ(I,J)
      EPPS(I,J)=-GZ(I,J)*UZCL
C
C   VARIABLES AT LIQUIDUS
C
      DO 300 I=2,IMAXN
      NNT=NT(I)
      J=NNT+1
      GZ(I,J)=(TL-TE)/(ZL(I)-ZS(I))
      GR(I,J)=-GZ(I,J)*A1L(I)
      EPPS(I,J)=-GZ(I,J)*UZCL
  300 CONTINUE
C
```

```
C    VARIABLES AT CENTER LINE
C
      I=1
      NNT=NT(I)+1
      DO 340 J=2,NNT
      GR(I,J)=0.0
      GZ(I,J)=TRAT/HTT(I)
      EPPS(I,J)=-GZ(I,J)*UZCL
      IF(J.EQ.NNT) GO TO 339
      IF(J.EQ.I) GO TO 338
      GO TO 340
  338 CONTINUE
      VR(I,J)=0.0
      VZ(I,J)=-UZCL*CONTR
      GO TO 340
  339 CONTINUE
  340 CONTINUE
      I=1
      J=1
      GR(I,J)=0.0
      GZ(I,J)=(TL-TE)/(ZL(I)-ZS(I))
      EPPS(I,J)=-GZ(I,J)*UZCL
   73 CONTINUE
C
C    CALCULATION OF VARIABLES AT BOUNDARIES(NEEDED FOR SUBSEQUENT
C    MACROSEGREGATION CALCULATION)****END
C
C
C*********************************************************************
C*********************************************************************
C    ITERATION SEQUENCE FOR 'P',VELOCITY, 'GL' AND COPM****BEGIN
C*********************************************************************
C*********************************************************************
C
      DO 1000 ITER=1,MAXIT1
C
```

```
C*******************************************
C   CALCULATION OF COEFFICIENTS****BEGIN
C*******************************************
C
C          THIS SECTION DEALS WITH THE DETERMINATION OF THE PARAMETERS
C          DEALING WITH THE COEFFICIENTS OF THE SECOND ORDER PARTIAL
C          DIFFERENTIAL EQUATION USED TO FIND THE VALUES OF PRESSURE
C          AT ANY GIVEN NODE WITHIN THE MUSHY ZONE.
C
      DO 150 I=2,IMAXN
      PPP=JMIN(I)
      NMT=NT(I)
      DO 145 J=PPP,NMT
      IF(J.GE.JWALL) GO TO 8004
      ZFRACS=(Z(I,J)-ZS(I))/KC
      RFRACS=(RS(J)-R(I,J))/HC
      IF((ZFRACS.LE.1.0).AND.(RFRACS.LE.1.0)) GO TO 17
      IF((ZFRACS.LE.1.0).AND.(RFRACS.GT.1.0)) GO TO 71
      IF((ZFRACS.GT.1.0).AND.(RFRACS.LE.1.0)) GO TO 171
 8004 CONTINUE
      IF((J.LE.NMT).AND.(J.GT.NT(I-1)))GO TO 111
      GO TO 737
   17 GL(I,J-1)=GLEUT(I)
      GL(I+1,J)=(GLEUT(I+1)-GLEUT(I))*RFRACS+GLEUT(I)
      CL(I,J-1)=CE
      CL(I+1,J)=CE
      RHO(I,J-1)=RLE
      RHO(I+1,J)=RLE
      T(I,J-1)=TE
      T(I+1,J)=TE
      KB=Z(I,J)-ZS(I)
      KA=KC
      HB=HC
      HA=RS(J)-R(I,J)
      TYPE=1.0
      GO TO 7997
```

```
 71 GL(I,J-1)=GLEUT(I)
    CL(I,J-1)=CE
    RHO(I,J-1)=RLE
    T(I,J-1)=TE
    KB=Z(I,J)-ZS(I)
    KA=KC
    HB=HC
    HA=HC
    TYPE=2.0
    GO TO 7997
171 GL(I+1,J)=(GLEUT(I+1)-GLEUT(I))*RFRACS+GLEUT(I)
    CL(I+1,J)=CE
    RHO(I+1,J)=RLE
    T(I+1,J)=TE
    KB=KC
    KA=KC
    HB=HC
    HA=RS(J)-R(I,J)
    TYPE=3.0
    GO TO 7997
111 HB=((ZL(I)-Z(I,J))/(ZL(I)-ZL(I-1)))*HC
    GL(I-1,J)=1.0
    CL(I-1,J)=CO
    RHO(I-1,J)=RO
    T(I-1,J)=TL
    HA=HC
    KA=KC
    ZZK=ZL(I)-Z(I,J)
    IF(J.EQ.NMT) KA=ZZK
    KB=KC
    TYPE=4.0
    GO TO 7997
737 CONTINUE
    HA=HC
    HB=HC
    KA=KC
```

```
      ZZK=ZL(I)-Z(I,J)
      IF(J.EQ.NMT) KA=ZZK
      KB=KC
      TYPE=5.0
      GO TO 7997
 7997 CONTINUE
      FACT1=1.0
      FACT2=GL(I,J)**2
      PERMI(I,J)=GAMMA(I,J)*(GL(I,J)**2)
      GZ(I,J)=(T(I,J+1)-T(I,J-1))/(KA+KB)
      GR(I,J)=(T(I+1,J)-T(I-1,J))/(HA+HB)
      EPPS(I,J)=-GZ(I,J)*UZCL
      DERHOR=(RHO(I+1,J)-RHO(I-1,J))/(HA+HB)
      DERHOZ=(RHO(I,J+1)-RHO(I,J-1))/(KA+KB)
      DECLR=(CL(I+1,J)-CL(I-1,J))/(HA+HB)
      DECLZ=(CL(I,J+1)-CL(I,J-1))/(KA+KB)
      DEGLR=(GL(I+1,J)-GL(I-1,J))/(HA+HB)
      DEGLZ=(GL(I,J+1)-GL(I,J-1))/(KA+KB)
      ALFA=(RHO(I,J)/RE-1.)*KON2/CL(I,J)
      A1=1.0D0/R(I,J)
      A2=2.*DEGLR/GL(I,J)+DERHOR/RHO(I,J)
      A3=ALFA*DECLR
      B1=2.*DEGLZ/GL(I,J)+DERHOZ/RHO(I,J)
      B2=ALFA*DECLZ
      C1=2.*DEGLZ/GL(I,J)+2.*DERHOZ/RHO(I,J)
      C2=ALFA*(DECLZ-(W**2)*DECLR*R(I,J)/GRAV)
      C3=GRAV*RHO(I,J)*(C1+C2)
      C4=DRODCL/RHO(I,J)+ALFA
      C5=EPPS(I,J)*MU/(EM*GAMMA(I,J)*GL(I,J))
      C6=(W**2)*(2.*RHO(I,J)+2.*RHO(I,J)*R(I,J)*DEGLR/GL(I,J)+2.*R(I,J)*
     1DERHOR)
      AX=A1+A2+A3
      B=B1+B2
      C=C3-C4*C5-C6
      IF(TYPE.EQ.1.0) GO TO 7998
      IF(TYPE.EQ.2.0) GO TO 7999
```

```
      IF(TYPE.EQ.3.0) GC TO 8000
      IF(TYPE.EQ.4.0) GO TO 8001
      IF(TYPE.EQ.5.0) GO TO 8001
 7998 CONTINUE
      GLE=RFRACS*(GLEUT(I+1)-GLEUT(I))+GLEUT(I)
      MO(I,J)=A1S(I+1)
      SOLVE=MU*CONTR*UZCL/(GAMMA(I,J)*GLEUT(I)*(1.+A1S(I)**2))-RLE*GRAV
      SOLHZ=-MU*CONTR*UZCL*MO(I,J)/(GAMMA(I,J)*GLE*(1.+MO(I,J)**2))
     $+RLE*RS(J)*(W**2)
      Q1=1./(2.*HB*(HA+HB))
      Q2=1./(2.*KA*(KA+KB))
      Q3=(HA*AX)/(2.*HB*(HA+HB))
      Q4=KB*B/(2.*KA*(KA+KB))
      Q5=SOLHZ/(HA+HB)-SOLVE/(KA+KB)+SOLHZ*AX*HB/(HA+HB)
     $+SOLVE*B*KA/(KA+KB)+C
      IF(I.EQ.2) GO TO 6711
      GO TO 6712
 6711 Q1=0.0
      Q3=0.0
 6712 CONTINUE
      Q6=Q1+Q2-Q3+Q4
      TATOP(I,J)=(Q2+Q4)/Q6
      TALEFT(I,J)=(Q1-Q3)/Q6
      TAKONS(I,J)=Q5/Q6
      TART(I,J)=0.0
      TABOT(I,J)=0.0
      GO TO 113
 7999 CONTINUE
      GLE=RFRACS*(GLEUT(I+1)-GLEUT(I))+GLEUT(I)
      MO(I,J)=A1S(I+1)
      SOLVE=MU*CONTR*UZCL/(GAMMA(I,J)*GLEUT(I)*(1.+A1S(I)**2))-RLE*GRAV
      Q2=1./(2.*KA*(KA+KB))
      Q4=KB*B/(2.*KA*(KA+KB))
      Q7=-SOLVE/(KA+KB)+KA*SOLVE*B/(KA+KB)+C
      TART(I,J)=(1./HA**2+AX*1.0/(2.*HB))/(Q2+Q4+2./(HB**2))
      TATOP(I,J)=(Q2+Q4)/(Q2+Q4+2./(HB**2))
```

```
      TALEFT(I,J)=(1./HB**2-AX*1.0/(2.*HB))/(Q2+Q4+2./HB**2)
      TAKONS(I,J)=Q7/(Q2+Q4+2./HB**2)
      TABOT(I,J)=0.0
      GO TO 113
 8000 CONTINUE
      GLE=RFRACS*(GLEUT(I+1)-GLEUT(I))+GLEUT(I)
      MO(I,J)=A1S(I+1)
      SOLVE=MU*CONTR*UZCL/(GAMMA(I,J)*GLEUT(I)*(1.+A1S(I)**2))-RLE*GRAV
      SOLHZ=-MU*CONTR*UZCL*MO(I,J)/(GAMMA(I,J)*GLE*(1.+MO(I,J)**2))
     $+RLE*RS(J)*(W**2)
      Q1=1./(2.*HB*(HA+HB))
      Q3=(HA*AX*1.0)/(2.*HB*(HA+HB))
      Q8=SOLHZ/(HA+HB)+AX*1.0*HB*SOLHZ/(HA+HB)+C
      TATOP(I,J)=(1./(KA**2)+B*1.00/(2.*KA))/(Q1-Q3+2./(KA**2))
      TABOT(I,J)=(1./(KA**2)-B*1.00/(2.*KA))/(Q1-Q3+2./(KA**2))
      TALEFT(I,J)=(Q1-Q3)/(Q1-Q3+2./(KA**2))
      TAKONS(I,J)=Q8/(Q1-Q3+2./(KA**2))
      TART(I,J)=0.0
      GO TO 113
 8001 CONTINUE
      IF(J.EQ.NT(I)) GO TO 5625
      GO TO 5626
 5625 CONTINUE
      XX=KA/KC
      YY=HB/HC
      IF((XX.LE.0.10).AND.(YY.LE.0.10)) GO TO 5620
      THEDA1=KA*KB*(2.+AX*HB-AX*HA)+HA*HB*(2.+B*KB-B*KA)
      THEDA2=(2.+HB*AX)*HB*KA*KB/(HA+HB)
      THEDA3=(2.+KB*B)*HA*HB*KB/(KA+KB)
      THEDA4=(2.-HA*AX)*HA*KA*KB/(HA+HB)
      THEDA5=(2.-KA*B)*HA*HB*KA/(KA+KB)
      THEDA6=KA*KB*HA*HB*C
      ONE(I,J)=THEDA2/THEDA1
      TWO(I,J)=THEDA3/THEDA1
      TRE(I,J)=THEDA4/THEDA1
      FOR(I,J)=THEDA5/THEDA1
```

```
      KONST(I,J)=THEDA6/THEDA1
      GO TO 5628
 5620 CONTINUE
      ONE(I,J)=0.
      TWO(I,J)=1.
      TRE(I,J)=0.
      FOR(I,J)=0.
      KONST(I,J)=0.
 5628 CONTINUE
      GO TO 5627
 5626 CONTINUE
      THEDA1=4.*(HB/HA+1.0)*(KA**2)
      THEDA2=4.*(HA/HB+1.0)*(KA**2)
      THEDA3=2.*AX*1.0*HB*(KA**2)*(1.0+HB/HA)
      THEDA4=2.*AX*1.0*HA*(KA**2)*(1.+HA/HB)
      THEDA5=((HA+HB)**2)
      THEDA6=4.*THEDA5+THEDA1+THEDA2+THEDA3-THEDA4
      ONE(I,J)=(THEDA1+THEDA3)/THEDA6
      TWO(I,J)=(2.+KA*B*1.00)*(THEDA5/THEDA6)
      TRE(I,J)=(THEDA2-THEDA4)/(THEDA6)
      FOR(I,J)=(2.-KA*B*1.00)*(THEDA5/THEDA6)
      KONST(I,J)=2.*(KA**2)*(THEDA5/THEDA6)*C
      GO TO 5627
 5627 CONTINUE
  113 CONTINUE
  145 CONTINUE
  150 CONTINUE
C
C    CALCULATION OF COEFFICIENTS******END
C
C
C****************************************
C    CALCULATION OF PRESSURES****BEGIN
C****************************************
C
C
```

```
C    CALCULATION OF PRESSURES ALONG CENTER-LINE
C
      NNT=NT(1)
      NMT=NNT
      I=1
      DO 5563 J=2,NMT
      DEGLZ=(GL(I,J+1)-GL(I,J-1))/(2.*KC)
      PERMI(I,J)=GAMMA(I,J)*(GL(I,J)**2)
      ALFA=(RHO(I,J)/RE-1.)*KON2/CL(I,J)
      GZ(I,J)=(TL-TE)/ZILIQ
      EPPS(I,J)=-GZ(I,J)*UZCL
      DERHOZ=(RO-RLE)/ZILIQ
      DECLZ=(CO-CE)/ZILIQ
      GR(I,J)=0.
      DERHOR=0.0
      DECLR=0.
      DEGLR=0.
      B1=2.*DEGLZ/GL(I,J)+DERHOZ/RHO(I,J)
      B2=ALFA*DECLZ
      C1=2.*DEGLZ/GL(I,J)+2.*DERHOZ/RHO(I,J)
      C2=ALFA*(DECLZ-(W**2)*DECLR*R(I,J)/GRAV)
      C3=GRAV*RHO(I,J)*(C1+C2)
      C4=DRODCL/RHO(I,J)+ALFA
      C5=EPPS(I,J)*MU/(EM*GAMMA(I,J)*GL(I,J))
      C6=(W**2)*(2.*RHO(I,J)+2.*RHO(I,J)*R(I,J)*DEGLR/GL(I,J)+2.*R(I,J)*
     1DERHOR)
      B=B1+B2
      C=C3-C4*C5-C6
      D(I,J)=AX
      E(I,J)=B
      F(I,J)=C
 5563 CONTINUE
      NNT=NT(1)
      NMT=NNT-1
      I=1
      DO 430 J=2,NMT
```

```
      IF(J.EQ.2) GO TO 5555
      Q50=4./(HC**2)+2./(KC**2)
      Q51=1./(KC**2)+E(I,J)/(2.*KC)
      Q52=4./(HC**2)
      Q53=1./(KC**2)-E(I,J)/(2.*KC)
      P(I,J)=Q51*P(I,J+1)/Q50+Q52*P(I+1,J)/Q50+Q53*P(I,J-1)/Q50+F(I,J)/
     $Q50
      GO TO 5556
 5555 CONTINUE
      Q54=4./(HC**2)+1./(4.*KC**2)+E(I,J)/(4.*KC)
      Q55=4./(HC**2)
      Q56=1./(4.*KC**2)+E(I,J)/(4.*KC)
      SOLVE=MU*CONTR*UZCL/(GAMMA(I,J)*GLEUT(I)*(1.+A1S(I)**2))-RLE*GRAV
      Q57=E(I,J)*SOLVE/2.+F(I,J)-SOLVE/(2.*KC)
      P(I,J)=Q55*P(I+1,J)/Q54+Q56*P(I,J+2)/Q54+Q57/Q54
 5556 CONTINUE
  430 CONTINUE
C
C    CALCULATION OF PRESSURES ALONG SOLIDUS-INTERIOR
C
      DO 410 I=2,IMAXN
      PPP=JMIN(I)
      NMT=NT(I)
      DO 408 J=PPP,NMT
      IF(J.GE.JWALL) GO TO 8005
      RFRACS=(RS(J)-R(I,J))/HC
      ZFRACS=(Z(I,J)-ZS(I))/KC
      IF((ZFRACS.LE.1.).AND.(RFRACS.LE.1.)) GO TO 888
      IF((ZFRACS.LE.1.).AND.(RFRACS.GT.1.)) GO TO 889
      IF((ZFRACS.GT.1.).AND.(RFRACS.LE.1.)) GO TO 891
 8005 CONTINUE
      IF((J.LE.NMT).AND.(J.GT.NT(I-1))) GO TO 405
      GO TO 406
  888 CONTINUE
      IF(I.EQ.2) GO TO 6713
      P(I,J) =TATOP(I,J)*P(I,J+2) + TALEFT(I,J)*P(I-2,J) + TAKONS(I,J)
```

```
      GO TO 6714
 6713 P(I,J)=TATOP(I,J)*P(I,J+2)+TAKONS(I,J)
 6714 CONTINUE
      GO TO 408
  889 CONTINUE
      P(I,J)=TART(I,J)*P(I+1,J)  + TATOP(I,J)*P(I,J+2)  + TALEFT(I,J)*
     $P(I-1,J)  + TAKONS(I,J)
      GO TO 408
  891 CONTINUE
      P(I,J)=TATOP(I,J)*P(I,J+1)+TALEFT(I,J)*P(I-2,J)+TABOT(I,J)*
     $P(I,J-1)+TAKONS(I,J)
      GO TO 408
C
C    CALCULATION OF PRESSURES FOR INTERIOR GRID POINTS
C
  405 CONTINUE
      RR=R(I,J)-HC*(ZL(I)-Z(I,J))/(ZL(I)-ZL(I-1))
      PP        =(ZLHIGH-Z(I,J))*RO*GRAV+PA+0.5*RO*(W**2)*(RR**2)
      P(I,J)=ONE(I,J)*P(I+1,J)+TWO(I,J)*P(I,J+1)+TRE(I,J)*PP+FOR(I,J)*
     $P(I,J-1)+KONST(I,J)
      GO TO 408
  406 CONTINUE
      RIGHT=ONE(I,J)*P(I+1,J)
      TOP=TWO(I,J)*P(I,J+1)
      LEFT=TRE(I,J)*P(I-1,J)
      BOTTOM=FOR(I,J)*P(I,J-1)
      P(I,J)=RIGHT+TOP+LEFT+BOTTOM+KONST(I,J)
  408 CONTINUE
  410 CONTINUE
C
C    CALCULATION OF PRESSURES ALONG THR WALL
C
      I=IMAX
      NMT=NT(I)
      MNT=JMIN(I)
      DO 5567 J=MNT,NMT
```

```
      IF((J.LE.NMT).AND.(J.GT.NT(I-1))) GO TO 5569
      GO TO 5570
 5569 CONTINUE
      HB=HC*(ZLHIGH-Z(I,J))/(ZLHIGH-ZL(I-1))
      T(I-1,J)=TL
      CL(I-1,J)=CO
      RHO(I-1,J)=RO
      GL(I-1,J)=1.0
      GO TO 5571
 5570 CONTINUE
      HB=HC
      GO TO 5571
 5571 CONTINUE
      GR(I,J)=(T(I,J)-T(I-1,J))/HB
      DERHOR=(RHO(I,J)-RHO(I-1,J))/HB
      DECLR=(CL(I,J)-CL(I-1,J))/HB
      DEGLR=(GL(I,J)-GL(I-1,J))/HB
      GZ(I,J)=(TL-TE)/(ZLHIGH-ZS(I))
      DERHOZ=(RO-RLE)/(ZLHIGH-ZS(I))
      DECLZ=(CO-CE)/(ZLHIGH-ZS(I))
      KB=KC
      KA=KC
      KBB=Z(I,J)-ZS(I)
      IF(J.EQ.MNT) KB=KBB
      ZZK=ZL(I)-Z(I,J)
      IF(J.EQ.NMT) KA=ZZK
      DEGLZ=(GL(I,J+1)-GL(I,J-1))/(KA+KB)
      PERMI(I,J)=GAMMA(I,J)*(GL(I,J)**2)
      ALFA=(RHO(I,J)/RE-1.)*KON2/CL(I,J)
      FPPS(I,J)=-GZ(I,J)*UZCL
      A1=1.0D0/R(I,J)
      A2=2.*DEGLR/GL(I,J)+DERHOR/RHO(I,J)
      A3=ALFA*DECLR
      B1=2.*DEGLZ/GL(I,J)+DERHOZ/RHO(I,J)
      B2=ALFA*DECLZ
      C1=2.*DEGLZ/GL(I,J)+2.*DERHOZ/RHO(I,J)
```

```
      C2=ALFA*(DECLZ-(W**2)*DECLR*R(I,J)/GRAV)
      C3=GRAV*RHO(I,J)*(C1+C2)
      C4=DRODCL/RHO(I,J)+ALFA
      C5=EPPS(I,J)*MU/(EM*GAMMA(I,J)*GL(I,J))
      C6=(W**2)*(2.*RHO(I,J)+2.*RHO(I,J)*R(I,J)*DEGLR/GL(I,J)+2.*R(I,J)*
     1DERHOR)
      AX=A1+A2+A3
      B=B1+B2
      C=C3-C4*C5-C6
      D(I,J)=AX
      E(I,J)=B
      F(I,J)=C
 5567 CONTINUE
      I=IMAX
      NMT=NT(I)
      MNT=JMIN(I)
      DO 450 J=MNT,NMT
      IF(J.EQ.MNT) GO TO 5560
      IF((J.LE.NMT).AND.(J.GT.NT(I-1))) GO TO 1021
      GO TO 1022
 5560 CONTINUE
      KA=KC
      KB=Z(I,J)-ZS(I)
      Q70=2./(HC**2)+1./ (2.*KA*(KA+KB))+KB*E(I,J)/(2.*KA*(KA+KB))
      Q71=2./(HC**2)
      Q72=(1.+KB*E(I,J))/(2.*KA*(KA+KB))
      SOLVE=MU*CONTR*UZCL/(GAMMA(I,J)*GLEUT(I)*(1.+A1S(I)**2))-RLE*GRAV
      Q73=RHO(I,J)*(W**2)*R(I,J)*(2./HC+D(I,J))+SOLVE*(KA*E(I,J)-1.)/
     $(KA+KB)+F(I,J)
      P(I,J)=Q71*P(I-1,J)/Q70+Q72*P(I,J+2)/Q70+Q73/Q70
      GO TO 5561
 1021 RR=RADIUS-HC*(ZLHIGH-Z(I,J))/(ZLHIGH-ZL(I-1))
      HB=HC*(ZLHIGH-Z(I,J))/(ZLHIGH-ZL(I-1))
      PP      =PA+RO*GRAV*(ZLHIGH-Z(I,J))+0.5*RO*(W**2)*(RR**2)
      KB=KC
      HA=HC
```

```
      KA=KC
      ZZK=ZL(I)-Z(I,J)
      IF(J.EQ.NMT) KA=ZZK
 5559 CONTINUE
      XX=KA/KC
      YY=HB/HC
      IF((XX.LE.0.10).AND.(YY.LE.0.10)) GO TO 5623
      Q60=2.*KA*KB+HB**2*(2.+KB*E(I,J)-KA*E(I,J))
      Q61=KB*(HB**2)*(2.+KB*E(I,J))/(KA+KB)
      Q62=2.*KA*KB
      Q63=KA*(HB**2)*(2.-KA*E(I,J))/(KA+KB)
      Q64=RHO(I,J)*(W**2)*RADIUS*(2.*HB*KA*KB+D(I,J)*(HB**2)*KA*KB)
     $+F(I,J)*(HB**2)*KA*KB
      GO TO 5624
 5623 CONTINUE
      Q60=1.
      Q61=1.
      Q62=.0
      Q63=.0
      Q64=.0
 5624 CONTINUE
      P(I,J)=Q61*P(I,J+1)/Q60+Q62*PP       /Q60+Q63*P(I,J-1)/Q60+Q64/Q60
      GO TO 5561
 1022 CONTINUE
      HB=HC
      HA=HC
      KB=KC
      KA=KC
      ZZK=ZL(I)-Z(I,J)
      IF(J.EQ.NMT) KA=ZZK
      Q60=2.*KA*KB+HB**2*(2.+KB*E(I,J)-KA*E(I,J))
      Q61=KB*(HB**2)*(2.+KB*E(I,J))/(KA+KB)
      Q62=2.*KA*KB
      Q63=KA*(HB**2)*(2.-KA*E(I,J))/(KA+KB)
      Q64=RHO(I,J)*(W**2)*RADIUS*(2.*HB*KA*KB+D(I,J)*(HB**2)*KA*KB)
     $+F(I,J)*(HB**2)*KA*KB
```

```
      P(I,J)=Q61*P(I,J+1)/Q60+Q62*P(I-1,J)/Q60+Q63*P(I,J-1)/Q60+Q64/Q60
 5561 CONTINUE
  450 CONTINUE
C
C    CALCULATION OF PRESSURES****END
C
C
C**********************************************************
C   CALCULATION OF INTERDENDRITIC FLUID VELOCITY****BEGIN
C**********************************************************
C
      IF(ITER.EQ.50) GO TO 6920
      IF(ITER.EQ.70) GO TO 6920
      IF(ITER.EQ.90) GO TO 6920
      IF(ITER.EQ.110) GO TO 6920
      GO TO 6921
 6920 WRITE(6,6931)
 6931 FORMAT(7X,'****',10X,'***',10X,'****',8X,'****',7X,'******',
     $5X,'********',4X,'******',5X,'***',2X,'***',2X,'******')
      WRITE(6,6922)
 6922 FORMAT(8X,'GL',12X,'P',12X,'VZ',10X,'VR',9X,'VTOT',7X,'TTHETA',
     $6X,'RARA',7X,'I',4X,'J',4X,'ITER')
      WRITE(6,6932)
 6932 FORMAT(7X,'****',10X,'***',10X,'****',8X,'****',7X,'******',
     $5X,'********',4X,'******',5X,'***',2X,'***',2X,'******'/)
 6921 CONTINUE
      DO 790 I =1,IMAX
      PPP=JMIN(I)
      NNT=NT(I)+1
      DO 776 J=PPP,NNT
      IF(J.GE.JWALL) GO TO 8006
      RFRACS=(RS(J)-R(I,J))/HC
      ZFRACS=(Z(I,J)-ZS(I))/KC
      IF((ZFRACS.LE.1.).AND.(RFRACS.LE.1.)) GO TO 710
      IF((ZFRACS.LE.1.).AND.(RFRACS.GT.1.)) GO TO 709
      IF((ZFRACS.GT.1.).AND.(RFRACS.LE.1.)) GO TO 722
```

```
8006 CONTINUE
     IF(J.EQ.NNT)  GO TO 724
     IF((I.EQ.IMAX).AND.(J.EQ.JMIN(I))) GO TO 709
     GO TO 8002
 710 CONTINUE
     KB=Z(I,J)-ZS(I)
     KA=KC
     HB=HC
     HA=RS(J)-R(I,J)
     SOLVE=MU*CONTR*UZCL/(GAMMA(I,J)*GLEUT(I)*(1.+A1S(I)**2))-RLE*GRAV
     PDZ=(KA/(KA+KB))*SOLVE+((KB/(KA+KB))*((P(I,J+2)-P(I,J))/(2.*KA)))
     PERMI(I,J)=GAMMA(I,J)*(GL(I,J)**2)
     VZ(I,J)=-PERMI(I,J)/(MU*GL(I,J))*(PDZ+GRAV*RHO(I,J))
     IF((I.EQ.1).OR.(I.EQ.IMAX)) GO TO 601
     GLE=RFRACS*(GLEUT(I+1)-GLEUT(I))+GLEUT(I)
     MO(I,J)=A1S(I+1)
     SOLHZ=-MU*CONTR*UZCL*MO(I,J)/(GAMMA(I,J)*GLE*(1.+MO(I,J)**2))
    $+RLE*RS(J)*(W**2)
     IF(I.EQ.2) GO TO 6715
     PDR=SOLHZ*HB/(HA+HB)+(HA/(HA+HB))*((P(I,J)-P(I-2,J))/(2.*HB))
     GO TO 6716
6715 PDR=SOLHZ*HB/(HA+HB)
6716 CONTINUE
     VR(I,J)=-PERMI(I,J)/(MU*GL(I,J))*(PDR-RHO(I,J)*(W**2)*R(I,J))
     GO TO 602
 601 VR(I,J)=0.0
     GO TO 602
 602 CONTINUE
     GO TO 740
 709 CONTINUE
     HA=HC
     HB=HC
     KA=KC
     KB=Z(I,J)-ZS(I)
     SOLVE=MU*CONTR*UZCL/(GAMMA(I,J)*GLEUT(I)*(1.+A1S(I)**2))-RLE*GRAV
     PDZ=(KA/(KA+KB))*SOLVE+((KB/(KA+KB))*((P(I,J+2)-P(I,J))/(2.*KA)))
```

```
      PERMI(I,J)=GAMMA(I,J)*(GL(I,J)**2)
      VZ(I,J)=-PERMI(I,J)/(MU*GL(I,J))*(PDZ+GRAV*RHO(I,J))
      IF((I.EQ.1).OR.(I.EQ.IMAX)) GO TO 603
      PDR=(P(I+1,J)-P(I-1,J))/(2.*HB)
      VR(I,J)=-PERMI(I,J)/(MU*GL(I,J))*(PDR-RHO(I,J)*(W**2)*R(I,J))
      GO TO 604
  603 VR(I,J)=0.0
      GO TO 604
  604 CONTINUE
      GO TO 740
  722 CONTINUE
      HA=RS(J)-R(I,J)
      HB=HC
      KA=KC
      KB=KC
      PDZ=(P(I,J+1)-P(I,J-1))/(2.*KA)
      PERMI(I,J)=GAMMA(I,J)*(GL(I,J)**2)
      VZ(I,J)=-PERMI(I,J)/(MU*GL(I,J))*(PDZ+GRAV*RHO(I,J))
      IF((I.EQ.1).OR.(I.EQ.IMAX)) GO TO 605
      GLE=RFRACS*(GLEUT(I+1)-GLEUT(I))+GLEUT(I)
      MO(I,J)=A1S(I+1)
      SOLHZ=-MU*CONTR*UZCL*MO(I,J)/(GAMMA(I,J)*GLE*(1.+MO(I,J)**2))
     $+RLE*RS(J)*(W**2)
      PDR=SOLHZ*HB/(HA+HB)+(HA/(HA+HB))*((P(I,J)-P(I-2,J))/(2.*HB))
      VR(I,J)=-PERMI(I,J)/(MU*GL(I,J))*(PDR-RHO(I,J)*(W**2)*R(I,J))
      GO TO 606
  605 VR(I,J)=0.0
      GO TO 606
  606 CONTINUE
      GO TO 740
 8002 CONTINUE
      ZZK=ZL(I)-Z(I,J)
      IF(J.EQ.NT(I)) KA=ZZK
      IF(J.LT.NT(I)) KA=KC
      PDZ=(P(I,J+1)-P(I,J-1))/(KA+KC)
      PERMI(I,J)=GAMMA(I,J)*(GL(I,J)**2)
```

```
      VZ(I,J)=-PERMI(I,J)/(MU*GL(I,J))*(PDZ+GRAV*RHO(I,J))
      IF((I.EQ.1).OR.(I.EQ.IMAX)) GO TO 727
      NMT=NT(I)
      IF((J.LE.NMT).AND.(J.GT.NT(I-1))) GO TO 7777
      GO TO 7778
 7777 CONTINUE
      HB=HC*(ZL(I)-Z(I,J))/(ZL(I)-ZL(I-1))
      RR=R(I,J)-HB
      PP=        PA+RO*GRAV*(ZLHIGH-Z(I,J))+0.5*RO*(W**2)*(RR**2)
      PDR=(P(I+1,J)-PP)/(HC+HB)
      VR(I,J)=-PERMI(I,J)/(MU*GL(I,J))*(PDR-RHO(I,J)*(W**2)*R(I,J))
      GO TO 728
 7778 CONTINUE
      HB=HC
      GO TO 5604
 5604 CONTINUE
      PDR=(P(I+1,J)-P(I-1,J))/(HC+HB)
      VR(I,J)=-PERMI(I,J)/(MU*GL(I,J))*(PDR-RHO(I,J)*(W**2)*R(I,J))
      GO TO 728
  727 VR(I,J)=0.0
      GO TO 728
  728 CONTINUE
      GO TO 740
  724 PDZ=(P(I,J)-P(I,J-2))/(ZL(I)-Z(I,J-2))
      PERMI(I,J)=GAMMA(I,J)*(GL(I,J)**2)
      VZ(I,J)=-PERMI(I,J)/(MU*GL(I,J))*(PDZ+GRAV*RHO(I,J))
      IF((I.EQ.1).OR.(I.EQ.IMAX)) GO TO 730
      IF(ZL(I-1).EQ.ZL(I)) GO TO 5598
      IF(ZL(I+1).GE.Z(I+1,J)) GO TO 5596
      IF(ZL(I+1).LT.Z(I+1,J)) GO TO 5597
      GO TO 5600
 5596 PDR=((P(I+1,J-1)+(P(I+1,J)-P(I+1,J-1))*(ZL(I)-Z(I,J-1))/KC)
     $-P(I,J))/HC
      GO TO 5600
 5597 PDR=((P(I+1,J-1)+(P(I+1,J)-P(I+1,J-1))*(ZL(I)-Z(I,J-1))/(ZL(I+1)-
     $Z(I+1,J-1)))-P(I,J))/HC
```

```
      GO TO 5600
 5598 PDR=(P(I+1,J)-P(I-1,J))/(2.*HC)
 5600 CONTINUE
      VR(I,J)=-PERMI(I,J)/(MU*GL(I,J))*(PDR-RHO(I,J)*(W**2)*R(I,J))
      GO TO 731
  730 VR(I,J)=0.0
      GO TO 731
  731 CONTINUE
  740 CONTINUE
      VTOT=(VR(I,J)**2+VZ(I,J)**2)**0.5
      IF(VR(I,J).EQ.0.0) VR(I,J)=1.0D-6
      ANG=VZ(I,J)/VR(I,J)
      TTHETA=(180.0/PI)*DATAN(ANG)
      RARA=(VR(I,J)*GR(I,J)+VZ(I,J)*GZ(I,J))/EPPS(I,J)
      IF(ITER.EQ.50) GO TO 6911
      IF(ITER.EQ.70) GO TO 6911
      IF(ITER.EQ.90) GO TO 6911
      IF(ITER.EQ.110) GO TO 6911
      GO TO 776
 6911 CONTINUE
      WRITE(6,7500) GL(I,J),P(I,J),VZ(I,J),VR(I,J),VTOT,TTHETA,RARA,
     $I,J,ITER
 7500 FORMAT(1X,1E13.4,1E15.6,5E12.3,2I5,1I7/)
  776 CONTINUE
  790 CONTINUE
  805 CONTINUE
C
C   CALCULATION OF INTERDENDRITIC FLUID VELOCITY****END
C
C
C********************************************
C   CALCULATION OF MACROSEGREGATION****BEGIN
C********************************************
C
C          INTEGRATION OF THE LOCAL SOLUTE DISTRIBUTION EQUATION IS
C          FOLLOWED-THROUGH COLUMN-WISE STARTING FROM THE LIQUIDUS.
```

```
C
      IF(ITER.EQ.50) GO TO 6918
      IF(ITER.EQ.70) GO TO 6918
      IF(ITER.EQ.90) GO TO 6918
      IF(ITER.EQ.110) GO TO 6918
      GO TO 6919
 6918 CONTINUE
      WRITE(6,6933)
 6933 FORMAT(5X,'*****************',4X,'*********************',4X,
     $'***************',5X,'*********',5X,'******')
      WRITE(6,9900)
 9900 FORMAT(5X,'LOCAL SOLUTE CCMP',4X,'FRACT LIQUID EUTECTIC',4X,
     $'RADIUS OF INGOT',5X,'COLUMN NO',5X,'ITERAT')
      WRITE(6,6934)
 6934 FORMAT(5X,'*****************',4X,'*********************',4X,
     $'***************',5X,'*********',5X,'******'/)
 6919 CONTINUE
      SUUM1=0.0
      SUUM2=0.0
      DO 1020 I=1,IMAX
      NMT=NT(I)
      SUM=0.
      MNT=JMIN(I)
      DO 810 IT=MNT,NMT
      NN=NMT-IT
      J=NN+MNT
      IF(J.EQ.NMT) NLGL(J+1)=0.0
      COEFT1=-KON4*RHO(I,J)/(CL(I,J)*RE)
      COEFT2=-KON4*RHO(I,J+1)/(CL(I,J+1)*RE)
      RATER1=VR(I,J)*GR(I,J)+VZ(I,J)*GZ(I,J)
      RATER2=VR(I,J+1)*GR(I,J+1)+VZ(I,J+1)*GZ(I,J+1)
      VZE(I)=-CONTR*UZCL/(1.+A1S(I)**2)
      VRE(I)=-A1S(I)*VZE(I)
      RATERE=VZE(I)*(TL-TE)/(ZL(I)-ZS(I))-VRE(I)*(TL-TE)*A1S(I)/
     $(ZL(I)-ZS(I))
      FN(J)=COEFT1*(1.+RATER1/EPPS(I,J))
```

```
      FN(J+1)=COEFT2*(1.+RATER2/EPPS(I,J+1))
      NLGL(J)=.5*(CL(I,J)-CL(I,J+1))*(FN(J)+FN(J+1))+SUM
      IF(NLGL(J).GT.0.0) NLGL(J)=0.0
      SUM=NLGL(J)
      GL(I,J)=EXP(NLGL(J))
      GS(J)=1.0-GL(I,J)
      CS(J)=KAY*CL(I,J)
      GO TO 810
  810 CONTINUE
      J=MNT
      EPPSE=-(TL-TE)*UZCL/(ZL(I)-ZS(I))
      NLGE=NLGL(J)+0.5*(CE-CL(I,J))*((-KON4*RLE/(CE*RSE))*(1.+RATERE/
     $EPPSE)+FN(J))
      GEE=EXP(NLGE)
C
C             LOCAL SOLUTE COMPOSITION FOR DESIGNATED RADII WITHIN
C             THE INGOT IS INITIATED.
C
      J=JMIN(I)
      SUMMS=0.5*(CSE+CS(J))*((1.-GEE)-GS(J))
      NNT=NT(I)+1
      J=NNT
      GS(J)=0.0
      CS(J) =KAY*CO
      PPP=JMIN(I)+1
      DO 850 J=PPP,NNT
      SUMMS=.5*(CS(J)+CS(J-1))*(GS(J-1)-GS(J))+SUMMS
  850 CONTINUE
      GLEUT(I)=GEE
      TNT=RE*SUMMS+RSE*CE*GEE
      DDD=RE*(1.-GEE)+RSE*GEE
      LOCCOM(I)=TNT/DDD
C
C    AVERAGE INGOT COMPOSITION ACROSS THE INGOT IS CALCULATED
C
      IF(I.EQ.1) GO TO 880
```

```
      IF(I.EQ.IMAX) GO TO 885
      DELRAD=HC
      GO TO 890
  880 DELRAD=HC/2.
      ROR(I)=HC/4.
      GO TO 890
  885 DELRAD=HC/2.
  890 CONTINUE
      SUUM1=ROR(I)*TNT*DELRAD+SUUM1
      SUUM2=ROR(I)*DDD*DELRAD+SUUM2
      CSINGT=SUUM1/SUUM2
      ROR(1)=0.0
      IF(ITER.EQ.50) GO TO 6913
      IF(ITER.EQ.70) GO TO 6913
      IF(ITER.EQ.90) GO TO 6913
      IF(ITER.EQ.110) GO TO 6913
      GO TO 1020
 6913 CONTINUE
      WRITE(6,7900) LOCCOM(I),GEE,ROR(I),I,ITER
 7900 FORMAT(1X,1E18.4,1E23.4,E20.3,1I13,1I13/)
      IF(I.EQ.IMAX) GO TO 6914
      GO TO 1020
 6914 WRITE(6,6935)
 6935 FORMAT(5X,'*************************')
      WRITE(6,6915)
 6915 FORMAT(5X,'AVERAGE INGOT COMPOSITION')
      WRITE(6,6936)
 6936 FORMAT(5X,'*************************'/)
      WRITE(6,6916) CSINGT
 6916 FORMAT(1X,1E20.4///)
C
C   CALCULATION OF MACROSEGREGATION****END
C
      WRITE(6,6937)
 6937 FORMAT(2X,'*****************************************************
     $***************************************************'///)
```

```
 1020 CONTINUE
C
C    CALCULATION OF MACROSEGREGATION****END
C
      GL(1,1)=GLEUT(1)
      GL(IMAX,JWAL)=GLEUT(IMAX)
 1000 CONTINUE
C
C    ITERATION SEQUENCE FOR 'P',VELOCITY, 'GL' AND COPM****END
C
      STOP
      END
```

BIOGRAPHICAL NOTE

The author was born on September 5, 1949 in Taiwan, the Republic of China. He completed his Bachelor's degree in Chemical Engineering at National Taiwan University in 1971 and Master's degree in Materials Engineering at the University of Wisconsin, Milwaukee in 1974. He entered MIT Graduate School in 1974.

He has the following publications:

1. S. Lau, Y.A. Chang and S. Kou: "Thermodynamic Properties of the β'-NiZn Intermetallic Phase Exhibiting the Cs-Cl-Structure", Metallurgical Transactions, 1974, vol. 5, pp. 1979.

2. S. Kou and Y.A. Chang: "Thermodynamics of the α-AuZn and β'-AuZn Phases", Metallurgical Transactions, 1975, vol. 6, pp. 39.

3. S. Kou and Y.A. Chang: "Thermodynamics of β_1-NiZn and α-NiZn Phases", Metallurgical Transactions, 1975, vol. 6, pp. 245.

4. S. Kou, and Y.A. Chang: "Thermodynamics of Ordered β_1-PdZn Alloys", Acta Metallurgica, vol. 23, 1975, pp. 1185.

5. S. Kou, D.R. Poirier and M.C. Flemings: "Macrosegregation in Electroslag Remelted Ingots", to be published in Electric Furnace Conference, Iron and Steel Society of AIME, 1977.

6. S. Kou, D.R. Poirier and M.C. Flemings: "Effect of Centrifugal Force on Macrosegregation in Electroslag Remelted Ingots", to be published in Metallurgical Transactions, 1978.